Cross-Linked Polymers of Phenylacetylene and 1,3-Diethynylbenzene: New Polymer Precursors for Nanoporous Carbon Materials for Supercapacitors and Gas Storage

by

Mark Grundy

A thesis submitted in partial fulfillment
of the requirements for the degree of
Master of Applied Science (MASc.)
in Natural Resources Engineering

The Faculty of Graduate Studies
Laurentian University
Sudbury, Ontario, Canada

THESIS DEFENCE COMMITTEE/COMITÉ DE SOUTENANCE DE THÈSE
Laurentian Université/Université Laurentienne
Faculty of Graduate Studies/Faculté des études supérieures

Title of Thesis
Titre de la thèse: Cross-Linked Polymers of Phenylacetylene and 1,3-Diethynylbenzene: New Polymer Precursors for Nanoporous Carbon Materials for Supercapacitors and Gas Storage

Name of Candidate
Nom du candidat: Grundy, Mark

Degree
Diplôme: Master of Applied Science

Department/Program
Département/Programme: Natural Resources Engineering

Date of Defence
Date de la soutenance: October 29, 2014

APPROVED/APPROUVÉ

Thesis Examiners/Examinateurs de thèse:

Dr. Zhibin Ye
(Supervisor/Directeur de thèse)

Dr. Ramesh Subramanian
(Committee member/Membre du comité)

Dr. Eduard Guerra
(Committee member/Membre du comité)

Dr. Hongfa Hu
(External Examiner/Examinateur externe)

Approved for the Faculty of Graduate Studies
Approuvé pour la Faculté des études supérieures
Dr. David Lesbarrères
M. David Lesbarrères
Acting Dean, Faculty of Graduate Studies
Doyen intérimaire, Faculté des études supérieures

ACCESSIBILITY CLAUSE AND PERMISSION TO USE

ABSTRACT

The increasing threats of global warming, rapid depletion of fossil fuels, and increasing energy demands are driving an enormous amount of research into clean renewable sources of energy, flue gas capture technologies, and environmentally friendly energy storage devices, to name a few. Activated carbons present a multipurpose material commonly used in many of these increasingly popular green technologies.

A wide range of cross-linked acetylenic polymers of phenylacetylene and 1,3-diethynylbenzene were synthesized and investigated in this thesis to generate materials for electrochemical double layer capacitors, CO_2 capture, and hydrogen storage. Chemical activation of the copolymers in the presence of KOH was shown to produce highly microporous carbons with various textural properties. The specific cross-linking densities of the polymer precursors prior to carbonization were shown to greatly affect the carbon yield, surface area, pore volumes and pore sizes of the carbons produced. Electrochemical measurements of the activated carbons showed their impressive performances as capacitor materials, with high specific capacitances (up to 446 F g^{-1} at 0.5 A g^{-1} in 3-electrode cell) and long cycle life. Gas sorption studies also demonstrated impressive H_2 and CO_2 adsorption capacities (up to 2.66 wt% or 13.3 mmol g^{-1} for H_2 adsorption at 77 K and 1 atm, and up to 30.6 wt% or 6.95 mmol g^{-1} for CO_2 adsorption at 273 K and 1 atm).

Owing to the high content of pendent alkyne groups in these polymers, complexation reactions with metallic carbonyl ligands are able to provide an effective

way of dispersing metallic and metal oxide nanoparticles within the synthesized copolymers, which could provide additional pseudocapacitive properties. An appropriate copolymer with high alkyne content was subjected to complexation with $Co_2(CO)_8$, and subsequently carbonized and oxidized to yield carbon-supported Co_xO_y/Co nanoparticles (Co_xO_y@C-CPD76%). In addition to pseudocapacitive contributions, the cobalt species also effectively catalyzed the production of graphitic networks within the carbon support, improving their conductive properties. Electrochemical measurements demonstrated impressive specific capacitance (310 F g^{-1} at 0.1 A g^{-1}) compared with non-activated carbons (160 – 177 F g^{-1} at 0.1 A g^{-1}) synthesized at identical conditions, and provided a large stable potential window (1.4 V) in an aqueous KOH solution. The combined electrochemical double layer capacitance and pseudocapactiance behaviour of the carbon and Co_xO_y/Co also provided improved energy densities (21 W h kg^{-1}), and uncompromised power densities (2017 W kg^{-1}) compared with the pristine carbons (~2034 W kg^{-1}).

Keywords: supercapacitor, electrochemical double layer capacitor, pseudocapacitor, energy storage, gas storage, carbon dioxide capture, hydrogen storage, polymer, cross-linked, phenylacetylene, diethynylbenzene, activated carbon, cobalt, cobalt oxide, palladium catalyst, cationic polymerization, thermal stability.

ACKNOWLEDGEMENTS

First and foremost, I would like to offer my sincerest gratitude to my supervisor, Dr. Zhibin Ye for his ever-present guidance, patience, knowledge, and encouragement throughout my thesis.

I would like to thank Dr. Eduard Guerra, my co-supervisor, and Dr. Jeffrey Shepherd who permitted me to use their equipment, and for providing me with their expert knowledge in electrochemistry, which helped me greatly.

I would also like to thank my group mates Peng Xiang, Zhongmin Dong, Vimal Tiwari, Zhe Chen, and Patakamuri Govindaiah, who provided both friendship and expertise during my research.

Lastly, and most importantly, I would like to thank my parents for their constant love and support in my entire life. Without their support and guidance, I would not have been able to achieve so much as I have so far.

Table of Contents

List of Schemes and Figures

List of Tables

Chapter 1: Introduction

Over the past century, society as a whole has become increasingly fast-paced, electronic-savvy, consumption-heavy, and highly dependent on efficient sources of energy. The burning of fossil fuels, as well as disposal of outdated electronics, batteries, and end-of life equipment have had a particularly negative impact on health of the environment. In 2006, it was estimated that 20 – 50 million metric tonnes of "E-waste" were accumulated in landfills each year, and has been increasing regularly ever since.[1] The E-waste, comprised of materials like computers, batteries, and photovoltaic cells, are leading sources of toxic and hazardous chemicals like mercury, lead, cadmium and other heavy metals.[1] With respect to global warming, greenhouse gas emissions continue to be result primarily from human activity. For example, emissions of CO_2 from human sources still account for up to 82% of all greenhouse gas emissions in the Unites States.[2] The accumulation of greenhouse gases, hazardous waste in the environment, and depletion of fossil fuel reserves have pushed researchers to develop new and more environmentally friendly energy storage materials,[3] greenhouse gas sequestration technologies, and hydrogen storage technologies for a vast array of applications.

Supercapacitors, a type of electrochemical capacitor, have been a particularly popular field of research since 1957, when a patent was published describing charge storage from an ionic double-layer formed at a carbon/aqueous-electrolyte interface.[4] This charge storage device was referred to as an electrochemical double layer capacitor (EDLC), and is the first of two categories of electrochemical supercapacitors discussed

and investigated in this work. Carbon was originally selected as the ion-adsorbing material because of its relatively unreactive nature and wide variety of allotropic forms, which results in nearly ideal polarizability in a 1 V potential range for aqueous solutions. Later, work by the Sohio corporation improved the energy limiting potential window offered by aqueous solutions (*ca.* 1.2 V) by utilizing dissolved salts in non-aqueous electrolytes, which widened the useful potential range up to 3.4 ~ 4 V, improving total energy densities. Then, in 1975, research conducted by Conway[4] described the so-called pseudocapacitive charge storage mechanism in an aqueous H_2SO_4 solution, which relied on the highly reversible oxidation and reduction reactions of RuO_2. This new charge storage system provided a slightly larger potential range (~1.4 V vs. ~1.2 V) in aqueous electrolytes, and much higher energy densities and capacitances than the previously proposed EDLC materials. The faradaically-induced charge storage mechanism is now commonly referred to as pseudocapacitance, and their respective active materials are called pseudocapacitors (PS). Unfortunately, the cycling life and power densities provided by PS materials were shown to be much lower than those of EDLCs.

Since their debut as viable charge storage mechanisms, a great deal of research has been conducted with the aim of improving electrochemical performance (*i.e.*, capacitance, energy, power, and useful potential ranges) of supercapacitors through the application of a plethora of synthesis strategies, novel materials, and fabrication methods. The subsequent sections in this chapter will review and discuss in detail the charge storage mechanisms, theory, models, materials, major advances and limitations of EDLC and PS materials, as well as their use in gas sorption technologies.[4]

1.1 Energy Storage in Capacitors

In its simplest form, a typical capacitor is made of two parallel conducting plates of equal area separated by an insulating dielectric material. The use of a dielectric material allows for charge storage when a potential is applied across the plates. The first capacitors, called condensers and later electrostatic capacitors, were constructed of metal plates separated by a dielectric material like glass or a vacuum, which were later improved upon by replacing the dielectric separator with an electrolyte in contact with an oxide layer of high surface area. The incorporation of electrolyte allowed for a double layer of ions to form on the surface of the oxide-coated plate, improving total charge stored. These were the first cases of electrolytic capacitors. To date, capacitors can be categorized as electrostatic, electrolytic, or electrochemical capacitors. The differences in performance between these capacitor types can be quantified in terms of their total specific capacitance (F g^{-1}), energy density (W h kg^{-1}) and power density (W kg^{-1}). Figure 1.1 shows a Ragone plot (Energy vs. Power) with the approximate ranges of electrostatic capacitors, electrochemical capacitors, batteries and fuel cells.[4,5] The advent of supercapacitors was essential to bridging the gap between electrostatic capacitors and conventional battery performances, providing fast charging and discharging rates like those of capacitors, but also providing high energy densities similar to those found in batteries. Additionally, supercapacitors have much better cycling life, charging times and charging efficiencies when compared with batteries. Table 1.1 shows typical values of performance indicators, and restrictions affecting the characteristics of capacitors and batteries.

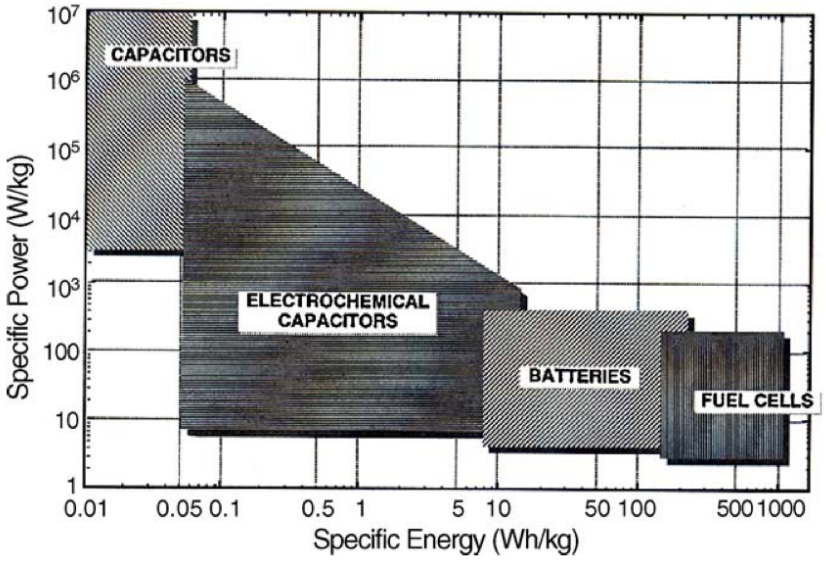

Figure 1.1 Ragone plot showing power densities and energy densities of capacitors, supercapacitors, batteries and fuel cells (adapted from ref. 5).

Table 1.1 Characteristics of electrolytic capacitors, carbon supercapacitors and batteries (adapted from ref. 5).

Characteristic	Electrolytic Capacitor	Carbon Supercapacitor	Battery
Specific energy (Wh/kg)	<0.1	1 – 10	10 - 100
Specific power (W/kg)	>>10000	500-10000	<1000
Discharge Time	10^{-6} to 10^{-3} seconds	Seconds to minutes	0.3 – 3h
Charging Time	10^{-6} to 10^{-3} seconds	Seconds to minutes	1 – 5h
Charge/Discharge Efficiency(%)	~100	85 – 98	70 – 85
Cycle-life	Infinite	>500000	~1000
Max. Voltage Restictions	Dielectric Thickness and Strength	Electrode and electrolyte stability window	Thermodynamics of phase reactions
Charge Stored Restrictions	Electrode Area and Dielectric	Electrode microstructure and electrolyte	Active mass and thermodynamics

The electrochemical capacitor region in Figure 1.1 could be further subcategorized into EDLC and PS categories, based on the differences between the charge storage mechanisms. The left side of the region would be occupied primarily by the EDLCs, which store charge similarly to the manner electrostatic capacitors do, while the right hand portion would be reserved for the battery-like charge storage of PS materials.

1.2 Electrochemical Double Layer Capacitors (EDLC)

EDLCs take advantage of the improved double-layer capacitance of electrolytic capacitors by utilizing conductive, chemically inert, and high surface area carbons as the electrode materials.[3-6] A schematic representation of a generalized supercapacitor cell is shown in Figure 1.2.

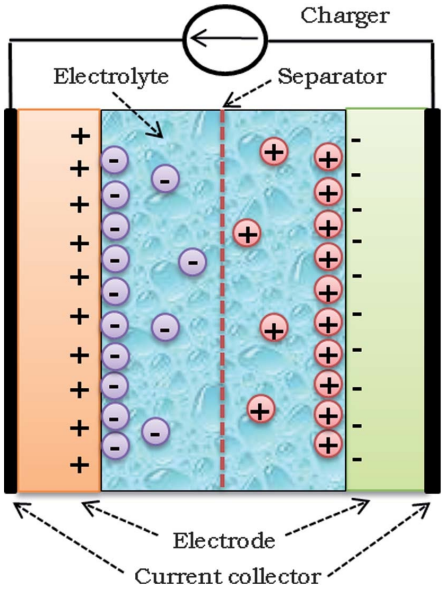

Figure 1.2 Schematic representation of a supercapacitor cell (adapted from ref. 7)

When a potential is applied across the cell, positive ions migrate towards the negatively charged electrode surface, and negative ions migrate towards the opposing positively charged electrode. The layers of opposing charges (called a double layer) that developed on the electrode surfaces was first described and modeled by von Helmholtz in the 19th century.[6] The formation of the double layer at each electrode is very similar to the conventional two plate capacitors, and can be described as two layers of opposing charge separated by a small atomic distance as shown in Figure 1.3(a). Later, Gouy and Chapman proposed a model in 1913 (Figure 1.3(b)) that described a distribution of ions in a diffuse layer near the electrode surface that was the result of thermally induced motion of the ions. However, the assumption of ions acting as point charges in the model resulted in a gross overestimation of capacitance.[4] In 1924 Stern combined the two aforementioned models to describe the double layer formation as the combination of a compact layer and diffuse layer.[4,6] In the compact layer, adsorption is described by a Langmuir adsorption isotherm, and the outer region is described through diffusion-controlled mechanisms. The Stern model (Figure 1.3(c)) also accounts for the atomic radii of the adsorbed and solvated ions within the electrolyte, allowing for an accurate estimation of the compact layer developed on the electrode surface.[4,6,8] The inner and outer Helmoltz layers are used to further categorize the two regions within the compact layer, based on their adsorption nature.

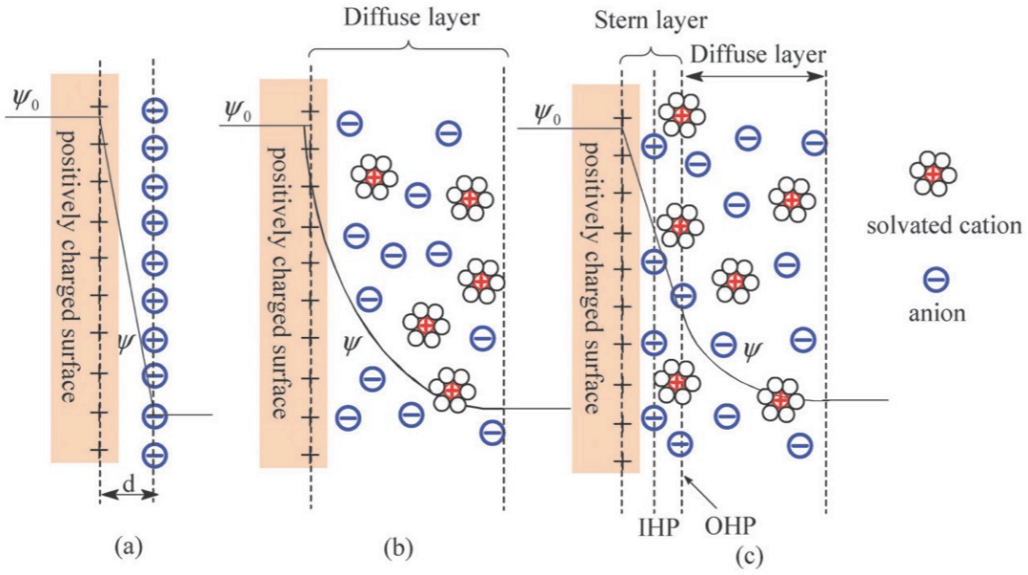

Figure 1.3 Models for a positively charged EDLC surface: (a) Helmholtz model, (b) Gouy-Chapman model, (c) Stern Model (adapted from ref. 6).

In Figure 1.3, Ψ_o and Ψ represent the potential of the electrode surface and electrode/electrolyte interface respectively for all three models, and IHP and OHP in Figure 1.3(c) refer to the inner and outer Helmholtz planes respectively of the Stern compact layer. IHP shows the distance of closest approach of the adsorbed ions to the surface, and OHP contains the ions that are non-specifically adsorbed.[4,6] The interface between the IHP and OHP also represents the beginning of the diffuse layer, first described in the Gouy-Chapment model (Figure 1.3(b)). Total double layer capacitance (C_{dl}) as described by the Stern model can be represented as the combined series capacitances of the compact layer (C_H), and diffuse layer (C_{diff}) as seen in Equation (1.1).[4,6,8]

$$\frac{1}{C_{dl}} = \frac{1}{C_H} + \frac{1}{C_{diff}} \qquad (1.1)$$

Because of the inverted nature of terms, the total double layer capacitance is dominated by the smaller of the two capacitances. Capacitances in conventional electrostatic capacitors separated by a dielectric medium are formally described using Equations (1.2) and (1.3):[4,6-8]

$$C = \frac{Q}{V} \tag{1.2}$$

$$C = \frac{A\varepsilon_0\varepsilon}{d} \tag{1.3}$$

where C is the capacitance measured in Farads (F), Q is the charge accumulated on the electrode, V is the potential applied between the electrodes, A is the total geometric area of the electrode, d is the distance between the two charged electrodes, ε_0 is the permittivity of a vacuum, ε is the dielectric constant of the insulating material, and the product of ε_0 and ε is the permittivity of the insulating material. Alternatively, specific areal capacitance or specific weight capacitance can be calculated by dividing by the surface area or mass of the electrode material respectively. The advent of high capacitance EDLCs took great advantage of the high surface area of carbon electrodes and the small distance of closest approach of ions at the electrode/electrolyte interface as per the Helmholtz layers, resulting in massive improvements in capacitance.

Considering that the work done to charge a capacitor is equal to the total energy stored within the capacitor, the energy stored by a capacitor can be derived. Substituting Equation (1.2) into Equation (1.4) and integrating, we obtain the capacitive energy given by Equation (1.5):[4]

$$E = \int_0^Q \frac{q}{C} dq = \frac{1}{2}\frac{Q^2}{C} \quad (1.4)$$

$$\mathrm{E} = \frac{1}{2} CV^2 \quad (1.5)$$

where E is the energy (J) stored in the capacitor, C is the capacitance, q and Q are the charges stored, and V is potential range used. Total power of the capacitor can then be represented as the rate of energy discharge given by Equation (1.6).[4]

$$P = \frac{E}{t} \quad (1.6)$$

where P is the power (W), and t is the discharge time (s).

It has been well established that the ultimate performance of EDLCs relies heavily on the physical and chemical properties, such as: accessible surface area, pore size distribution, pore volumes, surface properties and geometry of the carbon materials.[5,6,9] Notably, micropores (d < 2 nm) and mesopores (2 nm < d < 50 nm) have profound effects on total capacitance and power density respectively.[10,11] Micropores provide large adsorption areas, but restrict the flow of ions, while mesopores provide easy access of the ions to transport into the bulk of the carbon material, resulting in higher power densities. A combination of both micropores and mesopores are necessary for optimal performance in EDLCs, with intermediate energy and power densities. However, the electrochemical properties for specific carbons with change drastically with the use of different electrolytes.[5,8] Commonly used electrolytes in supercapacitors include aqueous solutions of H_2SO_4, KOH, NaOH, Li_2SO_4, and organic electrolytes like TEA-BF_4, and BMIM-BF_4

to mention a few.[8,12-14] Initial studies found that the total normalized capacitance is increased when the average pore size of the EDLC material is larger than the diameter of the solvated electrolytic ions that form the electric double layer.[15] Later studies, however, yielded an unexpected trend of increasing capacitance when pore sizes decreased below the diameter of the solvated ions (see Figure 1.4).[15] These pores were expected to be inaccessible to the ions and thus provide lower capacitances. It was later proposed that partial desolvation of the ions allowed them to access the sub-micron pores (d < 1 nm), forming a compact linear chain of ions within the pores that resulted in capacitance behaviour analogous to a wire-in-cylinder capacitor. However, the power density of such electrodes was shown to decrease greatly, due to restricted movement of the desolvated ions within the pores.[16-18]

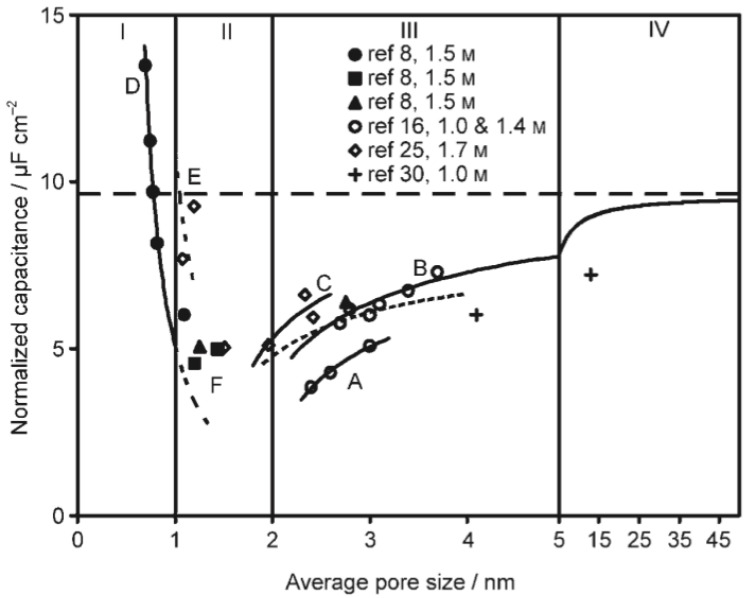

Figure 1.4 Relation of capacitance to pore size for different carbons in ionic liquids of TEA^+BF4^- and TEA^+MS^- (adapted from ref. 19).

1.3 Materials for EDLCs

As mentioned previously, the performances of EDLCs can vary greatly depending on the unique characteristics of the carbonaceous material. Porous carbons were the first materials utilized in EDLCs, and they have expanded to incorporate a variety of materials and synthesis methods to optimize capacitive properties. The most commonly utilized materials for EDLCs are described in the following section.

1.3.1 Activated Carbons (AC)

Activated carbons are highly microporous materials that have surface areas up to 3500 $m^2\ g^{-1}$, and they are the most commonly used EDLC materials because of their high stability, cycling life and chemical inertness.[9] The use of AC's in EDLCs improved capacitances by up to two orders of magnitude compared with electrostatic and electrolytic capacitors.[3,5,6,17,20] Synthesis of AC's is generally achieved by chemical or physical activation methods, including soft and hard templating, catalytic activation with alkali metal salts, carbonization of polymer blends, and carbonization of polymer aerogels.

Chemical and physical activations are the oldest and most commonly used methods in fabricating microporous and mesoporous ACs for use in a wide variety of applications, including gas adsorptions systems, water filtration, EDLCs, *etc*. Physical activation is accomplished with the gasification of carbons with CO_2 or stream at elevated temperatures, for example, while chemical activation is accomplished through chemical reactions with the carbon precursor. The most common chemicals used in the chemical activation processes are KOH, NaOH, KCl, $ZnCl_2$, and H_3PO_4.[16,21] Generally, chemical

activation starts with a non-porous carbon or carbon precursor that is doped with the activating agent through mixing in aqueous solutions. After mixing, the composite is subjected to high temperature conditions under inert gas atmospheres (N_2 or Ar) for a period of time. During high temperature treatment, the carbons undergo dehydrogenation and various chemical reactions with the activating agent, producing microporous ACs. Among the chemically activating agents, KOH is the most commonly used due to its low cost and ease of use.[16] The effects of differences in the precursors, textural properties, activating temperatures and times, and ratio of KOH to precursor ratios have been thoroughly studied.[22-25] Unfortunately, the large number of variables makes understanding the activation mechanisms difficult, but several reactions have been proposed and proven to contribute. These reactions can be seen in Equations (1.7) to (1.11).[24, 26-28]

$$6KOH + 2C \rightarrow 2K + 3H_2 + 2K_2CO_3 \quad (1.7)$$

$$2KOH \rightarrow K_2O + H_2O \quad (1.8)$$

$$K_2CO_3 \rightarrow 2C + 2K_2O \quad (1.9)$$

$$K_2CO_3 \rightarrow K_2O + CO_2 \quad (1.10)$$

$$K_2O + C \rightarrow 2K + CO \quad (1.11)$$

KOH has also been shown to act as a hard template, described in the next section, producing pores slightly larger than those produced through chemical reactions. In general, it was found that pores between 0.6 – 0.8 nm and pore around 1.2 nm were produced by chemical and physical activation route of KOH respectively.[26]

1.3.2 Templated Carbons

Templating methods can produce both microporous and mesoporous carbons depending on the templates and materials as well as the subcategory of templating used. Hard templating is a technique that utilizes a precursor with a rigid porous structure, such as a microporous zeolite or mesoporous silica. The structure of the carbon can also be tuned depending on the template structure. By controlling the structure of the template, its carbonization and subsequent removal can be tuned to produce a variety of highly structured carbons with narrow pore size distributions.[29-31] For example, hard-sphere colloidal systems (eg. silica spheres suspended in a precursor) can produce hollow sphere structures (Figure 1.5(a)), mesoporous silica can produce mesoporous carbon channels (Figure 1.5(b)), and microporous Zeolites can produce highly ordered interconnected microporous carbon spheres (Figure 1.5(c)).

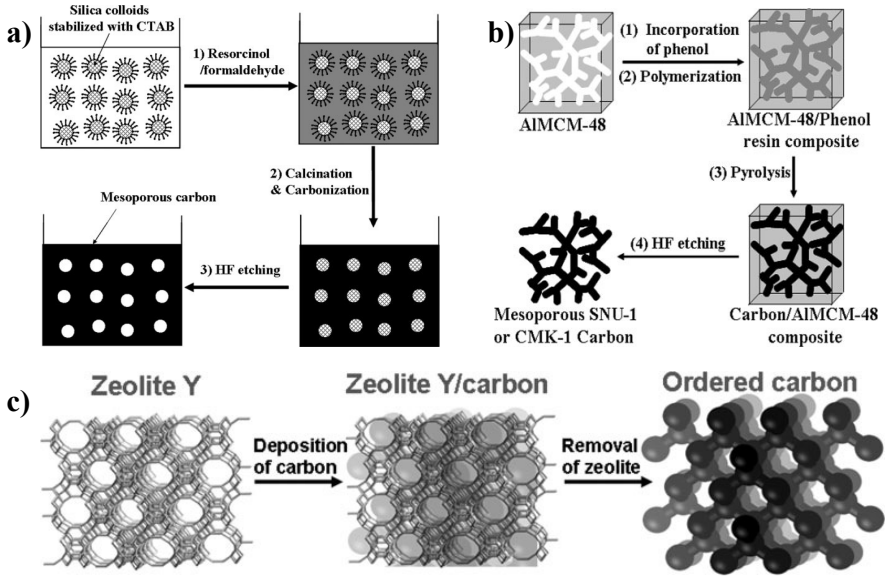

Figure 1.5 Examples of hard templating using (a) silica colloids, (b) mesoporous silica (c) microporous zeolitic framework (adapted from ref. 30).

Although hard templating provides well-ordered and highly controllable pores, the removal of the template usually requires the use of dangerous and hazardous chemicals like hydrofluoric acid.[30] Soft-templating technique utilizes the difference in thermal stabilities of co-polymers or micelle suspensions during carbonization to produce disordered mesoporous materials. In this method, harsh chemicals are not needed to remove the template, since it is decomposed at high temperature after the carbonization process. This method is also often referred to as the sacrificial template method.[30,32] Several conditions must be met for a successful synthesis using soft template method. In the case of the micelle route, surfactants or block co-polymers with different affinities to the precursor resin and solvent must be employed; these differences provide a driving force for micelle formation. Secondly, the precursor should have the ability to cross-link in order to withstand the harsh conditions of the carbonization process. A lack of cross-linking typically results in unstable frameworks that are more prone to pore collapse during carbonization. Finally, the decomposition temperatures of the two constituents should be relatively far apart to allow template removal without damaging the carbon structure.[29,30]

1.3.3 Graphenes and Carbon Nanotubes

Graphene and graphitic structures like carbon nanotubes (CNT) have been of great interest in a wide variety of scientific research in applications such as: electronics, biosensors, composite materials, and biotechnology, because of their unique chemical and physical properties.[33] However, their commercial use in these fields first requires that suitable technology for their bulk production be developed. For example few layer graphenes (FLG) were first produced through micromechanical exfoliation of graphite,

but this technique is limited to producing small quantities.[34] Later, chemical vapour deposition (CVD) techniques were shown to produce extremely well-defined 2-D graphene sheets as well as CNTs in much higher quantities. In this technique, graphene or CNT is typically grown onto metal substrates like nickel with controlled crystal structures, which catalyzes growth in the presence of an $Ar/H_2/CH_4$ gas feed. One shortcoming of this production method is that the graphene produced through CVD is very difficult to maintain in the 2-D structure while being incorporated into other materials as a result of interplanar attractions that cause irreversible restacking, and loss of their unique properties. Introducing spacer materials onto the surface of individual sheets, like CNTs, metal oxides, and conductive polymers, prevents this and has produced stable 3-D graphene structures.[35,36] Others have successfully grown single-layered 3-D graphene structures through CVD onto nickel foam supports, which are then threated with HCl to remove the nickel support, leaving behind a highly conductive, mesoporous 3-D graphene structure.[37,38]

Carbon nanotubes, like graphene, possess properties of high conductivity and high mechanical strength, and are used in similar applications to graphenes. Their tubular structures prevent the restacking problems faced by graphenes, but at the cost of surface area. Graphenes and CNTs can be used as standalone EDLCs, but are most often used as a conductive support for semiconducting pseudocapacitive metal oxides, and conducting polymers.[39,40]

Incorporation of pure graphene sheets into composite materials using CVD techniques still remains a challenge, since the composite material in question usually

require that the graphene be dispersed into solution with the aid of surfactants. Without surfactants, graphene sheets easily restack to form graphite, loosing their unique chemical and electrical properties. Alternatively, the incorporation of covalently bonded functional groups onto the surfaces of graphite can effectively exfoliate individual graphene sheets from the graphite, allowing their partial or total dissolution into aqueous and organic solutions. Hummer first attempted this in 1958 by reacting graphite and potassium permanganate ($KMnO_4$) in the presence of heat and H_2SO_4.[41] Owing to the highly oxidative properties of $KMnO_4$, the stacked graphite sheets are stripped apart though the incorporation of epoxy, hydroxyl and carboxylic functional groups along the edges and surface of the graphene layers. The as-produced oxidized graphenes were labeled as graphene oxides (GO), and they can be reduced back to graphene (called rGO) through chemical or thermal reduction. Graphene oxide's added functional groups prevent restacking in solutions, allowing their incorporation into polymerization reactions, and can provide a means of producing pseudocapacitive rGO/metallic-oxides on it's surface through hydrothermal treatment in the presence of metallic salts.

1.4 Pseudocapacitors (PS)

Pseudocapacitors typically store charge through the progress of reduction and oxidation reactions of transition metal oxides or conducting polymers at the electrode electrolyte interface. The progress of such reactions results in the accumulation of a charge gradient across the electrode/electrolyte double layer.[4]

1.4.1 Metal Oxides

The generalized redox reactions in Equations (1.12)-(1.17) show the reactions responsible for pseudocapacitive behaviour of Ru, Mn, Co, and Ni, which are amongst the most commonly researched materials:[20,42-45]

$$RuO_2 + xH^+ + xe^- \leftrightharpoons RuO_{2-x}(OH)_x \quad (1.12)$$

$$MnO_x(OC)_y + zC^+ + ze^- \leftrightharpoons MnO_{x-y}(OC)_{y+z} \quad (1.13)$$

$$3CoOOH + e^- \leftrightharpoons Co_3O_4 + OH^- + H_2O \quad (1.14)$$

$$NiOOH + e^- \leftrightharpoons NiO + OH^- \quad (1.15)$$

$$MOOH + H_2O + e^- \leftrightharpoons M(OH)_2 + OH^- \quad (1.16)$$

$$MO_2 + H_2O + e^- \leftrightharpoons MOOH + OH^- \quad (1.17)$$

where M = Ni or Co.

The changes in oxidation state undergone by metal oxides afford pseudocapacitors much higher specific capacitances and energy densities compared with EDLCs, but at the cost of lowed power densities since the progress of these redox reactions are often limited by the associated rate of change of the oxide structure. Unfortunately, volumetric changes are concomitant with these phase changes, which cause degradation of the PS over time, resulting in lower cycling lives.[20,46,47] Although the high theoretical capacitances of RuO_2 (1419 F/g), MnO_2 (1370 F/g), Co_3O_4 (3560 F/g) are highly desirable, conductive materials like graphenes, CNTs and ACs are often added to improve conductivity and power density at the cost of total energy and capacitance.[20,48,49] The carbonaceous additives can also provide a structural support, improving distribution of the metal oxides

and providing adequate free-volume for the volumetric changes undergone during charging and discharging.

Typically transition metal oxides/hydroxides are synthesized through wet chemistry, electrodeposition, and hydrothermal techniques.[42,50] In electrodeposition, electrolytic cells containing aqueous metallic salt solutions are subjected to applied voltages to drive cathodic metal deposition onto various substrates. Careful control of the salt precursor, substrate, ramping rates, potentials and holding times have been shown to grow a diverse range of metal oxides/hydroxides of differing morphologies and surface areas.[42,51-53] Hydrothermal techniques also use salt solutions, usually in the presence of ACs, GO and CNTs to produce carbon supported metal oxides with improved power densities and conductivities. Often, synthesis methods for incorporation of metal oxides into high surface area carbonaceous materials lack control over their distribution within the structure. However, some polymers and carbon materials containing particular pendent groups can provide anchor points for more uniform distribution of the oxides and prevent their agglomerations.[54-56]

1.4.2 Conductive Polymers

The underlying mechanism of charge storage for conductive polymers is the same for metal oxides; the conductive polymer provides chemically active sites for electrochemical phase changes to store energy rather than rely solely on EDLC behaviour. However, conducting polymers are generally categorized as P-doped or N-doped depending on the specific ion selectivity of the polymer. Equations (1.18) and

(11.9) show the generalized pseudocapacitive reactions undergone by conducting polymer pseudocapacitors.[47,57,58]

$$(A^-)_nCp^{n+} + ne^- \leftrightharpoons Cp + nA^- \quad (1.18)$$

$$Cp + nC^+ + ne^- \leftrightharpoons (C^+)_nCp^{n-} \quad (1.19)$$

where C_p refers to the conducting polymer, A^- and C^+ are the anion and cations of the electrolyte. Polyacetonitrile (PANI), polypyrrole (PPy), and poly(3,4-ethylene-dioxythiophene) (PEDOT) are amongst the most popularly studied conducting polymers for pseudocapacitive materials. [47,57,58]

1.5 Gas Sorption Technologies

Carbon dioxide emissions resulting from automobiles and industrial flue off-gases have had an enormous impact on our environment. Carbon dioxide (CO_2) has been proven to contribute to global warming, melting of polar ice caps, increasing the acidity of the oceans and more.[59, 60] Hydrogen has been investigated as an alternative fuel source to petroleum based fuels, since the resulting off gases are far less hazardous than those from typical petroleum based fuels.[61] High surface area materials comprised of activated carbons, metal organic frameworks (MOF), metal hydrides, zeolites, and polymers are well documented in literature as viable options for both the safe storage of H_2 and sequestration of CO_2 gases.[59-62]

Metal organic frameworks are hybrid materials composed of inorganic-organic compounds where a single metallic center is linked with an organic ligand compound, typically though coordination bonds. Metal organic frameworks are crystalline and, due to the high strength of the coordination bonds, can be produced with permanent porosities, which can be tuned through proper organic synthesis techniques. Because of their controllable pore sizes, molecular sieving can be easily applied for selective gas adsorption.[63] However, MOFs are often comprised of materials that are environmentally unfriendly.

Metal hydrides are used for the storage of hydrogen through the chemical adsorption of hydrogen gas onto a metallic surface (*eg.* Mg, Pd, Li, B).[64] The solid state storage of the hydrogen onto metallic surfaces give the metallic hydrides a significant improvement over traditional liquid and gas storage systems, in terms of both safety and total storage densities. Some disadvantages of metal hydride materials are: high costs, high weights, and slow discharge kinetics.[64]

Activated carbons, along with EDLC applications, have long been utilized for gas sorption and purification systems. Their abundance, low cost, environmentally friendliness, and chemically inert nature make them ideal for commercial applications.[61] Their performance in capacitor applications has been improved through the use of specific synthesis processes (ie. templating/chemical activation, precursors used *etc.*). However, these synthesis conditions might also be fine-tuned to provide ACs with improved gas sorption and textural properties. It has long been known that the high surface-areas provided by ACs, MOFs, metal hydrides etc., are strongly correlated to the

adsorption performances. In particular, the surface area and pore volume provided by micropores demonstrate the best correlations to CO_2 and H_2 adsorption capacities.[59-65]

1.6 Objective and Organization of Thesis

The objective of this thesis was to prepare and investigate the performance of a series of copolymers of phenylacetylene and 1,3-diethynylbenzene as: EDLC carbon precursors, gas storage materials, and carbon supports for pseudocapacitive charge storage. The thesis has been organized in a "sandwich" fashion.

Chapter 2 contains the research conducted to investigate copolymers of phenylacetylene and 1,3-diethynylbenzene as carbon precursors for EDLCs, hydrogen storage, and CO_2 adsorption. Copolymers with increasing cross-linking densities were synthesized and activated through carbonization in the presence of KOH, and characterized by gas sorption measurements, potentiometry studies, x-ray diffraction (XRD), thermogravimetric analysis (TGA), and transmission electron spectroscopy (TEM).

Chapter 3 explores their suitability as polymer precursors to obtain pseudocapacitive Co_xO_y nanoparticles distributed on a carbon support through complexation of dicobalt carbonyl with pendent alkyne groups. The chemical and physical characteristics of the carbon precursors were investigated throughout the different synthesis stages with nitrogen sorption measurements, potentiometry studies, XRD, TGA, TEM, and Fourier transform infrared spectroscopy.

Chapter 4 contains the conclusions derived from the research conducted in this thesis, and describes possible future work and the limitations of the application of these polymers for energy storage.

1.7 References

(1) United Nations Environment Programme. (2006, November) [Online]. http://www.unep.org/documents.multilingual/default.asp?DocumentID=485&ArticleID=5431&I=en

(2) United States Environmental Protcetion Agency. (2014, February). [Online]. http://www.epa.gov/climatechange/ghgemissions/gases/co2.html

(3) H. Chen, T. N. Cong, W. Yang, C. Tan, Y. Li, Y. Ding, *Prog. Nat. Sci.*, **2009**, *19*, 291-312.

(4) B. E. Conway, Electrochemical Supercapacitors - Scientific Fundamentals and Technological Applications. New York, N.Y., U.S.A.: Kluwer Academic/Plenum Publishers, 1999.

(5) A. G. Pandolfo and A. F. Hollenkamp, *J. Power Sources*, **2006,** *157*, 11-27.

(6) L. L. Zhang and X. S. Zhao, *Chem. Soc. Rev.*, **2009,** *38*, 2520-2531.

(7) S. Bose, T. Kuila, A. K. Mishra, R. Rajasekar, N. H. Kim, and J. H. Lee, *J. Mater. Chem.*, **2012,** *22*, 767-784.

(8) F. Beguin, V. Presser, A. Balducci, and E. Frackowiak, *Adv. Mater.*, **2014,** *26*, 2219–2251.

(9) L. Zhang, X. Yang, F. Zhang, G. Long, T. Zhang, K. Leng, Y. Zhang, Y. Huang, Y Ma, M. Zhang, Y. Chen, *J. Am. Chem. Soc.*, **2013,** *135*, 5921-5929.

(10) K. S. W. Sing, D. H. Everett, R. A. W. Haul, L. Moscou, R. A. Perotti, J. Rouquérol, T. Siemeineiwska, *Pure & Appl. Chem.*, **1985,** *57*, 603-619.

(11) A. D**ą**browski, *Adv. Colloid Interface Sci.,* **2001,** *93*, 135-224.

(12) T. Sato, G. Masuda, and K. Takagi, *Electrochim. Acta*, **2004,** *49*, 3603–3611.

(13) D.-E. Jiang, Z. Jin, D. Henderson, and J. Wu, *J. Phys. Chem. Lett.,* **2012,** *3*, 1727−1731.

(14) X. Sun, X. Zhang, H. Zhang, D. Zhang, and Y. Ma, *J. Solid State Electrochem.*, **2012,** *16*, 2597–2603.

(15) J. Huang, B. G. Sumpter, and V. Meunier, *Angew. Chem. Int.*, **2008,** *47*, 520 –524.

(16) L. L. Zhang, Y. Gu, and X. S. Zhao, *J. Mat. Chem. A*, **2013,** *1*, 9395–9408.

(17) J. Chmiola, G. Yushin, Y. Gogotsi, c. Portet, P. Simon, P. L. Taberna, *Science*, **2006,** *313*, 1760-1763.

(18) C. Largeot, C. Portet, J. Chmiola, P.-L. Taberna, Y. Gogotsi, and P. Simon, *J. Am. Chem. Soc.*, **2008,** *130*, 2730-2731.

(19) J. Huang, B. G. Sumpter, and V. Meunier, *Chem. Eur. J.*, **2008,** *14*, 6614–6626.

(20) K. Fic, E. Frackowiak, and F. Béguin, *J. Mater. Chem.,* **2012,** *22*, 24213–24223.

(21) M. J. Bleda-Martinez, J. A. Maciá-Agulló, D. Lozano-Catelló, E. Morallón, D. Cazaorla-Amorós, A. Linares-Solano, *Carbon*, **2005,** *43*, 2677-2684.

(22) K. Kierzek, E. Frackowiak, G. Lota, G. Gryglewicz, and J. Machnikowski, *Electrochim. Acta*, **2004,** *49*, 515–523.

(23) Y. Guo, J. Qi, Y. Jiang, S. Yang, Z. Wang, and H. Xu, *Mater. Chem. Phys.*, **2003,** *80*, 704–709.

(24) M. A. Lillo-Ródenas, D. Cazorla-Amoróa, and A. Linares-Solano, *Carbon*, **2003,** *41*, 267–275.

(25) C.-W. Huang, C.-T. Hsieh, P.-L. Kuo, and H. Teng, *J. Mater. Chem.*, **2012,** *22*, 7314-7322.

(26) Y. Li, T. Ben, B. Zhang, Y. Fu, and S. Qiu, *Sci. Rep.*, **2013,** *3*, 2420.

(27) R.-L. Tseng, S.-H. Tseng, F.-C. Wu, C.-C. Hu, and C.-C. Wang, J. *Chin. Inst. Chem. Eng*., **2008,** *39*, 37–47.

(28) L. Qie, W. Chen, H, Xu, X. Xiong, Y. Jian, F. Zou, X. Hu, Z. Zhang, and Y. Huang, *Energy Environ. Sci.*, **2013,** *6*, 2497–2504.

(29) M. Inagaki, H. Konno, and O. Tanaike, *J. Power Sources*, **2010,** *195*, 7880–7903.

(30) J. Lee, J. Kim, and T. Hyeon, *Adv. Mater.*, **2006,** *18*, 2073–2094.

(31) A.-H. Lu and F. Schüth, *Adv. Mater.*, **2006,** *18*, 1793-1805.

(32) L. Chuenchom, R. Kraehnert, and B. M. Smarsly, *Soft Matter*, **2012,** *8*, 10801–10812.

(33) C. Li and G. Shi, *Nanoscale*, **2012,** *4*, 5549–5563.

(34) K. S. Novoselov, A. K. Geim, S. V. Morozov, D. Jiang, Y. Zhang, S. V. Dubonos, I. V. Grigorieva, A. A. Firsov, *Science*, **2004,** *306*, 666-669.

(35) M. V. Kiamahalleh, S. H. S. Zein, G. Najafpour, S. A. Sata, and S. Buniran, *Nano*, **2012,** *7*, 1230002-1 – 123002-27.

(36) H. Jiang, P. S. Lee, and C. Li, *Energy Environ. Sci.*, **2013,** *6*, 41-53.

(37) S. Ye, J. Feng, and P. Wu, *Appl. Mater. Interfaces*, **2013,** *5*, 7122−7129.

(38) Y. He, W. Chen, X. Li, Z, Zhang, J. Fu, C. Zhao, and E. Xie, *ACS Nano*, **2013,** *7*, 174–182.

(39) H. Zhang, G. Cao, and Y. Yang, *Energy Environ. Sci.*, **2009,** *2*, 932-943.

(40) A. L. M. Reddy, S. R. Gowda, M. M. Shaijumon, and P. M. Ajayan, *Adv. Mater.,* **2012,** *24*, 5045–5064.

(41) W. S. Hummers and R. E. Offerman, *J. Am. Chem. Soc.*, **1958,** *80*, 1339-1339.

(42) C. D. Lokhande, D. P. Dubal, and O.-S. Joo, *Curr. Appl. Phys.*, **2011,** *11*, 255-270.

(43) M. Zhi, C. Xiang, J. Li, M. Li, and N. Wu, *Nanoscale*, **2013,** *5*, 72-88.

(44) V. Augustyn, P. Simon, and B. Dunn, *Energy Environ. Sci.*, **2014,** *7*, 1597–1614.

(45) J. Yan, W. Sun, T. Wei, Q, Zhang, Z. Fan, *J. Mater. Chem.*, **2012,** *22*, 11494–11502.

(46) A. S. Aricò, P. Bruce, B. Scrosati, J.-M. Tarascon, and W. van Schalkwijk, *Nat. Mater.,* **2005,** *4*, 366-377.

(47) G. Wang, L. Zhang, and J. Zhang, *Chem. Soc. Rev.*, **2012,** *41*, 797–828.

(48) C.-M. Chuang, C.-W. Huang, H. Teng, and H.-M. Ting, *Compos. Sci. Technol.,* **2012,** 72, 1524–1529.

(49) M. Zhi, A. Manivannan, F. Meng, and N. Wu, *J. Power Sources*, **2012,** *208*, 345–353.

(50) D. R. Rolison, J. W. Long, J. C. Lytle, A. E. Fischer, C. P. Rhodes, T. M. McEvoy, M. E. Bourg, A. M. Lubers, *Chem. Soc. Rev.*, **2009,** *38*, 226-252.

(51) X. Xiao, X. Liu, H. Zhao, D. Chen, F. Liu, J. Xiang, Z. Hu, and Y. Li, *Adv. Mater.,* **2012,** *24*, 5762–5766.

(52) C. Yuan, L. Yang, L. Hou, L. Shen, X. Zhang, and X. Wen, *Energy Environ. Sci.*, **2012,** *5*, 7883–7887.

(53) G. R. Peterson, F. Hung-Low, C. Gumeci, W. P. Basset, C. Koreniewski, and J. Hope-Weeks, **2014,** *6*, 1796−1803.

(54) G. He, J. Li, H. Chen, J. Shi, X. Sun, X. Wang, *Mater. Lett.*, **2012,** *82*, 61-63.

(55) C. Xiang, M. Li, M. Zhi, A. Manivannan, and N. Wu, *J. Power Sources*, **2013,** *226*, 65-70.

(56) D. Zhang and W. Zou, *Curr. Appl. Phys.*, **2013,** *13*, 1796-1800.

(57) G. A. Snook, P. Kao, and A. S. Best, *J. Power Sources*, **2011,** *196*, 1-12.

(58) P. Pieta, I. Obraztsov, F. D'Souza, and W. Kutner, *J. Solid State Sci. Technol.,* **2013,** *2*, M3120-M3134.

(59) N. P. Wickramaratne and M. Jaroniec, *J. Mater. Chem. A*, **2013,** *1,* 112-116.

(60) H. Furukawa and O. M. Yaghi, *J. Am. Chem. Soc.*, **2009,** *131*, 8875–8883.

(61) H. Jin, Y. S. Lee, and I. Hong, *Catal. Today*, **2007,** *120*, 399–406.

(62) M. Sevilla, J. B. Parra, A. B. Fuertes, *Appl. Mater. Interfaces*, **2013,** *5*, 6360−6368.

(63) J.-R. Li, R. J. Kuppler and H.-C. Zhou, *Chem. Soc. Rev*., **2009,** *38*, 1477-1504.

(64) B. Sakintuna, F. Lamari-Darkrim and M. Hirscher, Int. J. Hydrogen Energy, **2007,** *32*, *1121-1140.*

(65) C. D. Wood, B. Tan, A. Trewin, H. Niu, D. Bradshaw, M. J. Rosseinsky, Y. Z. Khimyak, N. L. Campbell, R. Kirk, E. Stöckel, and A. I. Cooper, *Chem. Mater.,* **2007,** *19,* 2034-2048

Chapter 2: Cross-linked polymers of diethynylbenzene and phenylacetylene as new polymer precursors for high-yield synthesis of high-performance nanoporous activated carbons for supercapacitors, hydrogen storage, and CO_2 capture

This chapter is organized based on manuscript published in

J. Mater. Chem. A, 2014, 2, 20316–20330

Abstract

We demonstrate in this article the first use of a family of cross-linked polymers synthesized from acetylenic monomers (diethynylbenzene and phenylacetylene) as new polymer precursors for high-yield synthesis of nanoporous activated carbons of tuneable textural properties. A range of cross-linked polymers of varying cross-linking densities has been tailor synthesized via catalytic polymerization of the monomers. Their carbonization in the presence of KOH as the activation agent renders effectively high-surface-area, predominantly microporous activated carbons of unique textural properties (surface area up to 1418 $m^2\ g^{-1}$; pore volume up to 0.78 $cm^3\ g^{-1}$) at high yields (ca. 70 wt%). It is discovered that the textural properties of the resulting carbon materials (including surface area, pore volume, pore size and pore size distribution) depend sensitively on the cross-linking density of the polymer precursors and are thus tuneable through polymer design. With their unique textural properties, the high-surface-area activated carbons exhibit superior performance in applications both as electrode materials in supercapacitors and as sorbents for H_2 storage and CO_2 capture. High specific capacitance (up to 446 F g^{-1} at 0.5 A g^{-1} in 3- electrode cell; 334 F g^{-1} at 0.1 A g^{-1} and

287 F g^{-1} at 0.5 A g^{-1} in 2-electrode cell) has been obtained for the electrodes fabricated with these carbons. Gas sorption study confirms that these carbons show remarkably high capacities for the adsorption of both H_2 and CO_2 (up to 2.66 wt% for H_2 adsorption at 77 K and 1 bar; up to 6.95 mmol g^{-1} along with a high CO_2/N_2 selectivity of 11 for CO_2 adsorption at 0 °C and 1 bar). These performance properties in all three applications are well comparable to or even better than the best results obtained with various activated carbons to date. The nanoporous activated carbons obtained from this new family of polymer precursors are thus the rare carbon materials that show combined superior performance in all three important applications.

2.1 Introduction

Nanostructured porous carbon materials of high surface area have recently received tremendous attention in energy and environmental technologies including hydrogen storage,[1] electric double layer capacitance (EDLC) supercapacitor,[2] and CO_2 capture.[3] They have been extensively studied and used as electrode materials for the EDLC supercapacitors and as the solid adsorbents for hydrogen storage and CO_2 capture, with some demonstrated to exhibit outstanding performance properties.[1-3] The performance of porous carbon materials in these applications is correlated strongly to their textural properties, such as pore size, pore size distribution, surface area, pore volume, pore geometry, surface properties, etc., in complex ways.[1-3] With regard to the pore size effect as a most important factor, on the basis of many studies, micropores smaller than 8 Å (optimum size of 6–7 Å for H_2 adsorption) play the key role in the adsorption of both H_2 and CO_2, particularly in the low-pressure range (e.g., 1 bar), with the amount of adsorption linearly proportional to the volume/surface area of these

micropores.[4,5] In EDLC supercapacitors, a bimodal porosity containing well-balanced micropores and either meso- or macro-pores or both is instead believed to be ideal, with the micropores (optimum size of around 7–8 Å) contributing predominantly to the actual energy storage and the larger pores facilitating fast transfer of ions to and from the micropores to ensure high power densities.[2,6] Designing porous carbon materials with tunable textural structures has thus been crucial to render high performance properties in these applications. In this regard, numerous nanostructured porous carbon materials with different textural properties have been developed with the use of various synthetic techniques, with activated carbons, carbon nanotubes, graphene, templated hierarchically structured nanoporous carbons, carbide-derived carbons, etc. being the notable examples in the three themed applications.[1-3,7]

Among the various porous carbon materials, activated carbons produced by carbonization of various precursors via different activation processes (physical and chemical) are most widely used in both EDLC supercapacitor and gas storage applications due to their high surface area, convenient synthesis, availability of precursor materials, low cost but with satisfactory performance properties.[1-3] In their production, the carbon precursors play a crucial role in determining the textural properties, chemical composition, and application performance properties of the resulting carbon materials. Enormous efforts have been focused on the discovery of carbon precursors and appropriate processing methods to obtain activated carbons with desired textural properties for optimum performance properties.[8] Currently, the common carbon precursors are various naturally occurring materials, including biomass (such as woods, coconut shells, carbohydrates, etc.), petroleum (such as petroleum pitch and coke) and

coal derived stocks.[9] Synthetic organic polymers are another important class of carbon precursors for activated carbons. Compared to naturally occurring carbon precursors, synthetic polymers as well-defined macromolecular precursors have the unique advantage of rendering the resulting carbon materials with fine-tuneable textural properties and compositions by controlling synthetic conditions of the polymers and have attracted significant interest for applications in EDLC supercapacitors and gas storage. Nevertheless, the types of polymer precursors are still restricted despite extensive research. Most commonly used polymer precursors include polyacrylonitrile,[10] condensation polymers of phenol- or resorcinol-formaldehyde or other combinations of monomers alike,[2b,c,e,6f,7a,c,d,11] cross-linked polystyrene,[12] poly(furfuryl alcohol),[13] ionic liquids and poly(ionic liquids),[8b–d,14] porous coordination polymers or metal–organic frameworks (MOF),[15] *etc*. These common polymer precursors, however, generally show low carbonization yields, with typical values being 40–65% for poly- acrylonitrile,[16] *ca*. 45% for polyfurfuryl alcohol,[13a] about 30% or less for ionic liquids or poly(ionic liquids),[8b–d,14a] about 45% for phenol-formaldehyde resins,[17] and 20% or less for cross-linked polystyrenes.[18] New polymer precursors rendering carbon materials of superior performance while at high yield are thus highly desired for practical applications.

Polymer precursors are often required to possess cross-linking structures, which affect carbonization yield and textural properties of resulting carbon materials. Generally, polymers are believed to decompose thermally into volatile low-molecular-weight molecules at elevated temperatures. The presence of cross-linking can often enhance their stability and thus increase the carbonization yield by reducing the formation of volatile molecules.[18] For most polymer precursors, such as cross-linked polystyrene, poly(furfuryl

alcohol), and condensation polymers of phenol- or resorcinol-formaldehyde, the cross-linking structures are built in during polymer synthesis. In the special case of polyacrylonitrile that does not intrinsically contain cross-linking structures, its oxidative stabilization pretreatment renders ladder structures (of pyridinic heterocyclic six-membered rings) and cross-linked structures that serve as precursors for subsequent carbonization.[10] Although the importance of cross-linking in polymer carbonization has long been recognized, little attention has been paid to the effects of cross-linking on the textural properties as well as performances of resulting carbon materials in EDLC supercapacitor and gas storage applications.

In this paper, we report the first use of a family of tailor- designed cross-linked polymers of 1,3-diethynylbenzene (DEB) and phenylacetylene (PA) having various cross-linking densities as a new family of polymer precursors for the synthesis of porous carbon materials. Synthesized from commercially available acetylenic monomers of high carbon content (95 and 94 wt% for DEB and PA, respectively), these polymers give rise to porous carbon materials through carbonization at yields (up to 85%) much higher than common polymer precursors. The yield and textural properties of the carbon materials have been systematically studied and correlated to the cross-linking density or composition of the polymer precursors. The performance properties of the resulting carbon materials as the electrode materials in EDLC supercapacitors and sorbents for H_2 and CO_2 adsorption have been systematically investigated. In particular, the high-surface-area activated carbons obtained from these polymer precursors have been found to show superior performance properties (high electrocapacitance as electrode materials in EDLC supercapacitors and high capacity for the adsorption of H_2 and CO_2 at 1 bar), which

compete well with the best performance data reported for activated carbons in the literature in all three applications. Not only reporting a new family of polymer precursors for high-yield carbon synthesis, this paper also discloses the dramatic effects of cross-linking on the textural properties of resulting carbons and their performance properties in these applications.

2.2 Experimental section

2.2.1 Materials

DEB (97%, Aldrich), PA (98%, Aldrich), palladium acetate ($Pd(OAc)_2$, min 98%, Strem Chemicals), α,α'-bis(di-t-butylphosphino)-o-xylene (97%, Strem Chemicals), methanesulfonic acid (99.5%, Aldrich), dichloromethane (HPLC grade, Aldrich), methanol (ACS reagent, Fisher Scienti¢c), sulfuric acid (96%+, Aldrich), titanium foil (99.95%, Aldrich), Nafion solution (5 wt% in lower aliphatic alcohols, Aldrich), platinum wire (0.5 mm in diameter, 99.95%, Strem Chemicals), conducting carbon (acetylene black 100%, Soltex), and potassium hydroxide (Flakes, reagent grade, 90%, Aldrich) were all used as received without any additional purification. Deionized water was obtained from a Barnstead/Synbron Nanopure II water purification system.

2.2.2 Synthesis of poly(DEB) and copolymers of DEB with PA

All the polymers, including both homopolymers and copolymers of DEB and PA, were synthesized through catalytic polymerization with the use of an in situ generated diphosphine-ligated cationic Pd(II) catalyst system, $Pd(OAc)_2$/α,α'-bis(di-t-butylphosphino)-o-xylene/methanesulfonic acid. For each polymerization, fixed molar ratios of DEB:Pd:diphosphine = 150:1:3 were used. A typical polymerization procedure

(for synthesis of CPD91% with 91 mol% of DEB in the monomer feed) is as follows. DEB (1 g), PA (0.081 g), and 10 mL of methanol were charged into a Schlenk flask equipped with a magnetic stirring bar under nitrogen protection. In a separate flask, $Pd(OAc)_2$ (0.0119 g) and diphosphine ligand (0.059 g) were mixed in 10 mL methanol under sonication to form the catalyst solution. The catalyst solution was injected into the Schlenk flask, followed with the addition of two drops of methanesulfonic acid, to start the polymerization. The polymerization lasted for 18 hours, and the polymer product was precipitated out in acidified methanol. The polymer was washed with methanol 3 times, and was then dried for 2 days under vacuum at room temperature.

2.2.3 Preparation of carbon materials by carbonization

Direct carbonization of the polymers without any activation agent was carried out by heating the polymers in a tube furnace to 800 °C at a rate of 10 °C min^{-1} in a N_2 atmosphere, which were subsequently cooled down to room temperature naturally. In the case of carbonization with KOH as the activation agent, the polymer/KOH mixture at a mass ratio of 1:2 was first prepared by mixing the polymer and KOH in methanol, followed with the removal of methanol by evaporation under vacuum. Carbonization was then performed using the same procedure as above in N_2. The carbonization product was washed with a large amount of water acidified with 2% HCl and then with deionized water until a pH of ~7 was reached. It was finally washed twice with methanol and then dried under vacuum to render the activated carbon.

2.2.4 Characterization and measurement

Thermogravimetric analysis (TGA) of the polymers was carried out on a Q50 TGA from TA instruments. Measurements were performed in a N_2 atmosphere with a

continuous N_2 low of 60 mL min^{-1} through the sample furnace and a flow of 40 mL min^{-1} through the balance compartment. In a typical measurement, the sample (*ca*. 10 mg) was heated to 100 °C at a rate of 10 °C min^{-1}, held at 100 °C for 10 min, and then heated to 800 °C at 10 °C min^{-1}. Braunauer–Emmett–Teller (BET) specific surface area, pore volume, and pore size distribution of all carbon samples were determined by N_2 sorption at 77 K using a Micromeritics ASAP 2020 physiosorption analyzer. The micropore size distribution was calculated using the Horvath–Kawazoe (HK) model. The pore size distribution for pores greater than 20 Å (i.e., mesopores and macropores) was calculated from N_2 desorption data using the Barrett–Joyner–Halenda (BJH) model. The adsorption of CO_2 and H_2 with the carbon samples were measured with the same instrument at 0 °C and -196 °C, respectively. Before the sorption measurements, the carbon samples were degassed under vacuum at 300 °C for *ca.* 20 h. X-ray photoelectron spectroscopy (XPS) measurements of carbon samples were carried out on a Thermo Scientific Theta Probe XPS spectrometer. A monochromatic Al Kα X-ray source was used, with a spot area of 400 μm. The samples were run in a standard mode, *i.e*., all angles collected (60° angular acceptance) for the survey spectra, and for the region spectra. X-ray diffraction (XRD) patterns of the carbon samples were recorded on an X' Pert Pro diffractometer with Co radiation (wavelength 1.79 Å) at room temperature. Transmission electron microscopy (TEM) images were taken on a JEOL 2010F field emission electron microscope operated at 200 keV. The TEM samples were prepared by depositing a few drops of a dilute dispersion of the carbon samples in methanol on holey grids, followed with drying.

All electrochemical measurements, including cyclic voltammetry (CV), galvanostatic charge/discharge (GCD), and electrochemical impedance spectroscopy

(EIS), were conducted with a Metrohm Autolab PGSTAT100 potentiostat/galvanostat on both 3-electrode and 2-electrode cells. In the case of measurements on three-electrode cells, a coiled platinum wire and a saturated calomel electrode were used as the counter and the reference electrode, respectively, with aqueous 1M H_2SO_4 as the electrolyte. The working electrodes for the electrochemical characterization were prepared with a titanium foil (4 cm^2) as the current collector. To prepare the electrode, the carbon sample (80 wt%), conducting carbon (10 wt%), and Nafion (10 wt%) were dispersed in a water-acetone (1:1 in vol) solution under sonication in a small vial. The dispersion was then evenly coated onto the titanium current collector. Subsequently, the electrode was dried in an oven at 130 °C for ca. 15 min. The typical mass of active carbon on the electrode was 1.25 mg cm^{-2}. CV curves were obtained between -0.2 and 0.8 V at different scan rates (100, 50, 25, 10, 5 mV s^{-1}, respectively). The specific capacitance (C_{sp} in F g^{-1}) was calculated from the CV curves through the following equation:[19]

$$C_{sp} = \frac{\frac{1}{2}\int idV}{m\Delta V v} \tag{2.1}$$

where i and V are the current and voltage, respectively, in the CV curves, $\int idV$ is the integration of the current loop over the whole voltage range, m is the mass of the active carbon, and v is the rate of voltage scan. GCD measurements were performed at current densities of 10, 5, 3, 2, 1, 0.5, and 0.1 A g^{-1}, respectively, within -0.2 and 0.8 V. The specific capacitance was calculated from the discharge curve through the following equation:[19]

$$C_{sp} = \frac{i}{m\, dV/dt} \tag{2.2}$$

where i is the discharge current, m is carbon mass, and dV/dt is calculated as the slope of the discharge curve within the voltage range following the end of ohmic drop to the end of the discharge curve. In all CV and GCD measurements, the cell was cycled until negligible changes prior to recording the data for calculation. EIS measurements were conducted at static potentials of 0 V over the frequency range from 10 kHz to 0.01 Hz with an AC perturbation of 10 mV.

Besides the measurements on 3-electrode cells, a symmetric 2-electrode cell was also fabricated with AC-CPD71% as the active carbon. In the assembly of the cell, the two electrodes, prepared on titanium foil in the same way as above, were separated with a filtration paper and were filled with aqueous 1M H_2SO_4 solution. CV measurements were performed within a voltage range of 0–1 V at the voltage sweep rate of 100, 50, 25, 10, 5, 1 mV s^{-1}, respectively. The specific capacitance was calculated from the CV curves through the following equation:[19]

$$C_{sp} = \frac{\int idV}{m\Delta V v} \tag{2.3}$$

where i and V are the current and voltage, respectively, in the CV curves, $\int idV$ is the integration of the current loop over the whole voltage range, m is the mass of the active carbon in each electrode, and v is the rate of voltage scan. GCD measurements were performed within voltage range of 0–1 V at current densities of 10, 5, 3, 2, 1, 0.5, and 0.1

A g^{-1}, respectively. The specific capacitance was calculated from the discharge curve through the following equation:[19]

$$C_{sp} = \frac{2i}{dV/dt} \tag{2.4}$$

where i is the discharge current, m is carbon mass in each electrode, and dV/dt is calculated as the slope of the discharge curve within the voltage range following the end of ohmic drop to the end of the discharge curve. The energy density (E, in W h kg^{-1}) and power density (P, W kg^{-1}) were calculated according to:

$$E = \frac{1}{2} C_{sp} V^2 \cdot \frac{1}{4} \cdot \frac{1}{3.6} \tag{2.5}$$

$$P = \frac{E}{t} \tag{2.6}$$

where V is the cell voltage after ohmic drop and t is the discharge time (in h). The EIS measurement was also conducted on the 2-electrode cell as above for the 3-electrode cells.

2.3 Results and discussion

2.3.1 Polymer synthesis, carbonization, and textural properties of nanoporous carbons

The polymer precursors, including seven copolymers of PA and DEB featured with different cross-linking density and their homopolymers, were synthesized herein via a convenient one-step chain-growth polymerization catalyzed with an in situ generated

cationic diphosphine-ligated Pd(II) catalyst system, $Pd(OAc)_2$/α,α'-bis(di-t-butylphosphino)-o-xylene/methanesulfonic acid. The copolymers are termed as CPDX% (*i.e.*, CPD91%, CPD84%, CPD71%, CPD63%, CPD45%, CPD39%, CPD26%, CPD17%, and CPD8%) with the number X representing the molar percentage of DEB in the two monomers fed for the polymerization. The homopolymers are termed as PDEB and PPA, respectively. Synthesized from acetylenic monomers (PA and DEB) containing alkyne groups, these polymers belong to the family of acetylenic polymers. In the polymerization system, DEB, a difunctional monomer, works effectively as a cross-linker. During the polymerization, incorporation of DEB through one of its two alkyne groups renders a pendant alkyne group, which can be subsequently enchained to render a cross-linking structure (see Scheme 2.1). Adjusting the molar percentage of DEB in the fed monomer mixture should tune effectively the cross-linking density of the copolymers, with PDEB homopolymer having the highest cross-linking density among the polymers and PPA

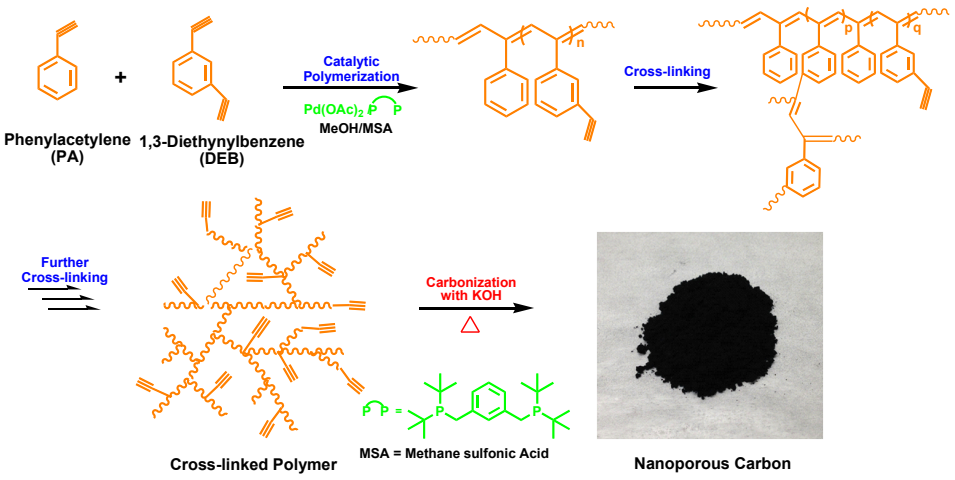

Scheme 2.1 Schematic synthesis of the cross-linked polymers and nanoporous carbons.

being linear without any cross-linking. As shown below, the cross-linking density plays an important role in determining the carbonization yield, textural properties, and application performance of resulting carbon materials.

This polymerization system was previously developed by us to synthesize soluble hyperbranched poly(phenacetylene)s containing pendant alkyne groups.[20] Unlike the earlier work, the cross-linking densities in the polymers herein are significantly higher due to the much higher DEB percentages in the monomers, rendering insoluble polymer gels. Given their insoluble highly cross-linked nature, precise determination of the cross-linking density in the polymers was not possible. Nevertheless, it should increase qualitatively with the increase of the percentage of DEB in the monomers during the polymerization following the mechanism of cross-linking. As per our earlier study, the composition of the polymers should be identical or nearly identical to that of the monomer mixture fed in the polymerization.[20]

One-step direct carbonization of the polymers without any activation agent was first performed by heating them to 800 °C in a N_2 atmosphere. To monitor the carbonization process, TGA measurements were also performed in parallel by following the identical heating procedure. Figure 2.1(a) displays the TGA curves of representative polymers for brevity; Figure 2.1(b) shows the dependence of the carbonization yield at 800 °C as a function of DEB molar percentage in the polymerization. While linear PPA without any cross-linking structures shows nearly complete weight loss (negligible residual mass of only 3%) at 800 °C, PDEB having the highest cross-linking density has a very high carbonization yield of 83%. For the copolymers, decreasing the DEB molar

percentage in the polymerization leads to a consistent pronounced decrease in the carbonization yield from 85% for CPD91% to 66% for CPD45% and 26% for CPD8% (see Figure. 2.1(b)). For polymers synthesized at DEB molar percentage >45%, their carbonization yield (66–85%) is notably higher than the typical values (35–65%) for most other polymers reported in the literature. Previously, polyacetylene, another acetylenic polymer, was reported to give rise to carbon materials by pyrolysis.[21] However, its carbonization yield was very low, below 20%.

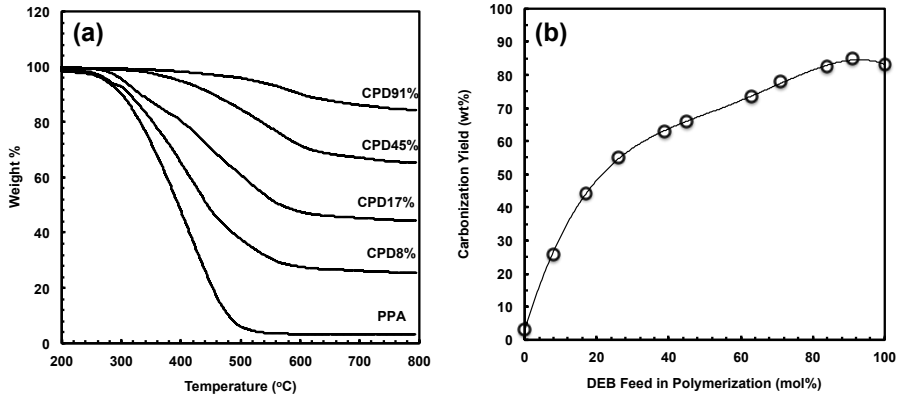

Figure 2.1 a) TGA curves of representative polymers of different cross-linking density measured at 10 °C min^{-1} in N_2; (b) carbonization yield (weight retention at 800 °C in TGA) as a function of DEB molar percentage in the polymerization.

On the basis of the corresponding 1st-order TGA derivative curves shown in Figure. 2.S1 in ESI, decreasing the DEB molar percentage also reduces significantly the temperature at maximum rate of weight loss from 580 °C for CPD91% to 550 °C for CPD45%, 427 °C for CPD8%, and 412 °C for PPA. The nearly complete weight loss observed with PPA indicates its high tendency towards thermal decomposition to render volatile low-molecular-weight molecules at elevated temperatures due to its linear chain

structure. In sharp contrast to linear PPA, the presence of covalent cross-linking helps significantly reduce the thermal decomposition of the polymers and renders dramatically enhanced carbonization yield. The effects become increasingly pronounced with the increase of cross-linking density. This is consistent with others studies showing the positive effect of cross-linking on improving thermal stability and increasing char yield in other polymer systems.[18,22]

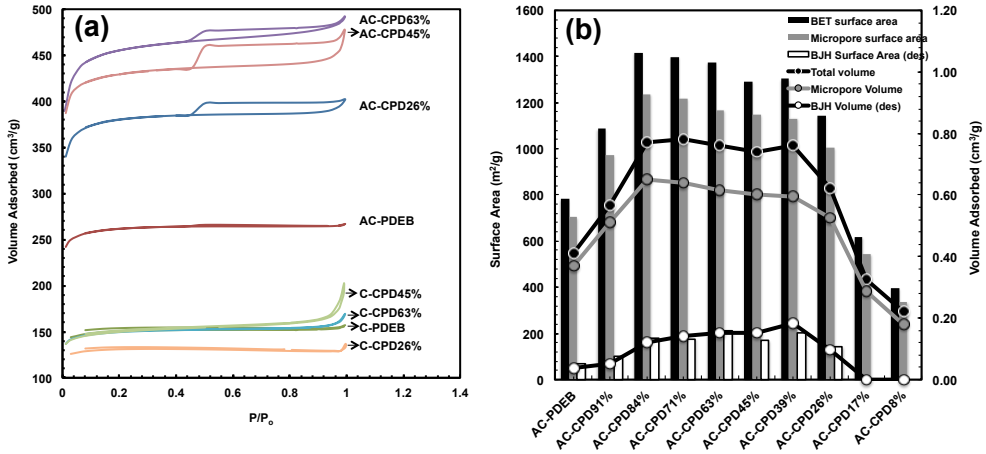

Figure 2.2 (a) N_2 adsorption–desorption isotherms of representative non-activated carbons and activated carbons; (b) dependencies of surface area and pore volume data of the activated carbons on the polymer precursors.

The carbon materials (termed correspondingly as C-PDEB or C-CPDX% with prefix C representing the nonactivated carbons) obtained above from carbonization without activation were characterized with N_2 sorption and XRD to elucidate their textural properties. In Figure. 2.2(a), the N_2 sorption isotherms of representative carbons (C-PDEB, C-CPD63%, C-CPD45%, and C-CPD26%) are shown, with the related characterization results (surface area, pore volume, and average pore size) summarized in

Table 2.1. All these carbons except C-CPD17% and C-CPD8% show typical type I isotherms,[23] with sharp uptakes at low relative pressure ($P/P_0 < 0.1$) and slight uptakes at high relative pressure ($P/P_0 > 0.95$). These isotherms indicate that the carbons without activation are predominantly microporous (containing micropores with sizes below 2 nm) with marginal mesopores (sizes between 2 and 50 nm) or macropores (sizes above 50 nm).[23] BET surface area (S_{BET}) of these carbons is generally low in the range of 305–500 $m^2 g^{-1}$, with the majority (>84%) originating from micropores (see Table 2.1). Their pore volume is in the range of 0.21–0.31 $cm^3 g^{-1}$, also resulting predominantly (*ca.* 85%) from micropores. The ranges of surface area and pore volume data are typically found with nonactivated carbons obtained from polymer precursors.[10a,11c,12] The majority of micropores have the diameter below 6 Å, contributing to 58–81% of total pore volume (see Figure 2.S2(a) for micropore size distribution curves and Table 2.1). In particular, micropores with size in the narrow range of 4.5 and 6 Å have *ca.* 40% of total pore volume. The average micropore size is about 4.8 Å for all samples. These micropore structures should be generated by the loss of hydrogen and/or the decomposition of the polymer chain segments during the carbonization process. With the decrease of cross-linking density from PDEB to CPD26%, there are no pronounced changes in the surface area, pore volume, average micropore size, and micropore size distribution. C-CPD17% and C-CPD8% obtained from polymers (CPD17% and CPD8%, respectively) with low cross-linking densities instead showed negligible N_2 sorption with marginal surface area and pore volume. This indicates the possible collapse of pore structures during the carbonization of the latter two polymers without having sufficient cross-linking.

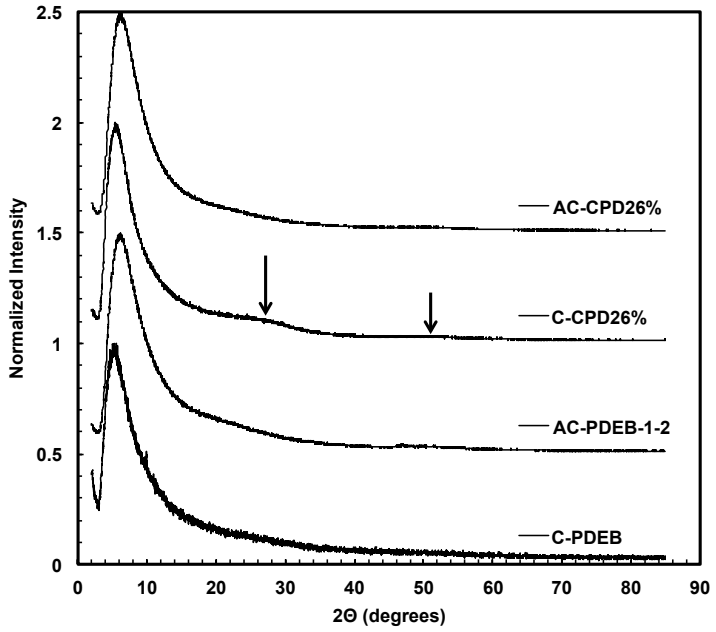

Figure 2.3 XRD patterns of representative carbon materials.

In Figure 2.3, the XRD spectra of two representative carbons (C-PDEB and C-CPD26%) are shown. In the spectra of both samples, there is an intense diffraction peak with peak maximum at *ca.* 5°, indicating the presence of high-density pores within the carbon materials.[15c] In addition, very weak but broad peaks are noticed near 28° and 50°, which are attributed to the (002) and (100) peaks, respectively, of graphitic structures.[14,15,24] The very weak and broad nature of the peaks indicates a low degree of graphitization with a low concentration of parallel single layers in these carbon materials, which is typical of amorphous carbon materials prepared by pyrolysis at the relatively low temperature of 800 °C herein due to insufficient graphitization.[14,15,25]

Table 2.1 Results from N_2 sorption characterization

Carbon Sample	Surface Area [a] (m^2/g)		Pore Volume [b] (cm^3/g)					Average Pore Size [c] (Å)	
	S_{BET}	$S_{d<20\ Å}$ (%)	V_{total}	$V_{d<20\ Å}$ (%)	$V_{d<6\ Å}$ (%)	$V_{4.5\ Å<d<6\ Å}$ (%)	$V_{d<4.5\ Å}$ (%)	d_{meso}	d_{micro}
C-PDEB	450	404 (90%)	0.24	0.21 (88%)	0.17 (71%)	0.10 (42%)	0.07 (29%)	28	4.7
C-CPD91%	500	446 (89%)	0.26	0.23 (88%)	0.20 (77%)	0.13 (50%)	0.07 (27%)	21	4.8
C-CPD84%	461	409 (89%)	0.25	0.21 (84%)	0.17 (68%)	0.11 (44%)	0.06 (24%)	24	4.9
C-CPD71%	468	415 (89%)	0.26	0.22 (84%)	0.17 (65%)	0.11 (42%)	0.06 (23%)	38	4.9
C-CPD63%	450	393 (87%)	0.26	0.21 (81%)	0.15 (58%)	0.10 (38%)	0.05 (19%)	43	5.0
C-CPD45%	452	381 (84%)	0.31	0.20 (64%)	0.18 (58%)	0.11 (35%)	0.07 (22%)	70	4.7
C-CPD39%	305	256 (84%)	0.22	0.16 (73%)	0.14 (64%)	0.07 (32%)	0.07 (32%)	109	4.7
C-CPD26%	391	359 (92%)	0.21	0.19 (90%)	0.17 (81%)	0.11 (52%)	0.06 (28%)	-	4.8
C-CPD17%	45	44 (98%)	0.02	0.02				-	-
C-CPD8%	0	0	0	0				-	-
AC-PDEB	784	704 (90%)	0.41	0.37 (90%)	0.31 (76%)	0.14 (34%)	0.17 (41%)	22	4.6
AC-CPD91%	1087	973 (90%)	0.57	0.51 (89%)	0.39 (68%)	0.22 (35%)	0.17 (30%)	20	5.0
AC-CPD84%	1418	1236 (87%)	0.77	0.65 (84%)	0.45 (64%)	0.37 (48%)	0.08 (10%)	27	5.3
AC-CPD71%	1399	1218 (87%)	0.78	0.64 (82%)	0.44 (56%)	0.37 (47%)	0.07 (9%)	32	5.3
AC-CPD63%	1374	1168 (85%)	0.76	0.61 (80%)	0.42 (55%)	0.36 (47%)	0.06 (8%)	29	5.3
AC-CPD45%	1292	1148 (89%)	0.74	0.60 (81%)	0.45 (61%)	0.38 (51%)	0.07 (9%)	36	5.2
AC-CPD39%	1303	1132 (87%)	0.76	0.59 (78%)	0.44 (58%)	0.36 (47%)	0.08 (10%)	36	5.2
AC-CPD26%	1143	1004 (88%)	0.62	0.53 (85%)	0.40 (64%)	0.33 (53%)	0.07 (11%)	28	5.1
AC-CPD17%	619	545 (88%)	0.32	0.29 (91%)	0.22 (69%)	0.15 (47%)	0.07 (22%)	22	5.0
AC-CPD8%	398	338 (85%)	0.22	0.18 (82%)	0.12 (54%)	0.09 (41%)	0.03 (14%)	29	5.4

[a] BET surface area (S_{BET}) and surface area of micropores ($S_{d<20\ Å}$) determined with t-plot method. [b] Total pore volume (V_{total}), micropore volume ($V_{d<20\ Å}$) determined with t-plot method, pore volume of micropores with size below 6 Å ($V_{d<6\ Å}$), pore volume of micropores with size between 4.5 and 6 Å ($V_{4.5\ Å<d<6\ Å}$), and pore volume of micropores with size below 4.5 Å. The percentage data in parentheses denote the percentage of pore volume of micropores of respective sizes relative to the total pore volume. c Average mesopore size (d_{meso}) determined from the N_2 desorption data with BJH model and median micropore size (d_{micro}) determined with HK model.

The above non-activated carbon materials all possess low surface area and low porosity, which makes them unsuitable for applications as electrode materials of high electrocapacitance for EDLC supercapacitors or sorbents of high capacity for H_2 and CO_2. To obtain carbons of significantly enhanced surface area and pore volume, we subsequently prepared activated carbons (termed correspondingly as AC-PDEB or AC-CPDX% with prefix AC noting activated carbons) from the polymer precursors (PDEB and CPDX%) by carbonizing them in the presence of KOH as the chemical activation agent with the use of the same heating procedure as above. KOH has been one of the most common chemical activation agents for carbon materials and its mechanism of activation has been studied in the literature.[26] For all polymer precursors, the mass ratio of KOH to polymer precursors was kept at 2:1.

This carbonization method produced efficiently activated carbons of significantly higher surface area and pore volume while at a high carbonization yield of *ca*. 70% for polymer precursors including PDEB and copolymers (CPDX%) with X≧26%. From N_2 sorption, all activated carbons show combined type I/IV isotherms (see Figure 2.2(a) for isotherms of representative activated carbons), with a steep adsorption to reach a plateau at the low relative pressure range ($P/P_0 < 0.1$), and the presence of a distinct hysteresis of type H4 at various sizes in the P/P_0 range of 0.45–1.0 and a slight uptake at high relative pressure ($P/P_0 > 0.95$).[23] These isotherms indicate that the activated carbons are highly microporous with the presence of some mesopores and macropores. Meanwhile, the type H4 hysteresis suggests that the mesopores are narrow slit-like.[23]

As listed in Table 2.1, the BET surface area (S_{BET}) of these activated carbons is within the range of 398–1418 $m^2\ g^{-1}$ with about 90% originating from micropores ($S_{d<20}$ Å); their total pore volume (V_{total}) is within the range of 0.22–0.78 $cm^3\ g^{-1}$ with the majority (78–91%, see Table 2.1) being micropore volume ($V_{d<20}$). The surface area and pore volume data are within typical ranges found with activated carbons obtained by activation with KOH at the KOH/precursor ratio of 2.[6g] Figure 2.2(b) shows the dependencies of the surface area (total surface area, micropore surface area, and BJH mesopore surface area) and pore volume (total pore volume, micropore volume, and BJH mesopore volume) on the polymer precursors having different cross-linking density. One can note a similar trend of change in these textural parameters with the change of polymer precursors. With the gradual decrease of cross-linking density from PDEB to CPD84%, the surface area and pore volume data all show a pronounced increase. For example, S_{BET} increases sharply from 784 $m^2\ g^{-1}$ for AC-PDEB to 1418 $m^2\ g^{-1}$ for AC-CPD84%. This increase is reasoned to result from the significantly enhanced diffusion of KOH into the cross-linked polymer matrix, during the polymer/KOH mixing procedure, following the decrease in cross-linking density, which helps the generation of more pore structures by chemical activation during the carbonization process. With the continued decrease in the cross-linking density from CPD84% to CPD39%, all the data, however, show only small changes, with S_{BET} changing marginally to 1303 $m^2\ g^{-1}$ for AC-CPD39%. This suggests that, within this intermediate range of cross-linking density, the polymer matrix is fully assessable to KOH without diffusional restriction. A further decrease in cross-linking density afterwards from CPD39% to CPD8%, however, leads to dramatic decreases in all the data. For example, S_{BET} drops sharply to 619 $m^2\ g^{-1}$ for AC-CPD17% and further to 398 $m^2\ g^{-1}$ for AC-CPD8%. This latter trend of decrease is ascribed to the increasingly

severe collapse of the pore structures during the carbonization process as a result of insufficient, decreasing cross-linking.

The cross-linking density of the polymer precursors also affects significantly the average pore size and pore size distribution of the resulting activated carbons. Figure 2.S2(b) shows the micropore size distribution of the activated carbons obtained from N_2 adsorption data with the HK model under the assumption of slit pores. It can be noted that the majority of micropores in these activated carbons also have their sizes below 6 Å with their pore volume ($V_{d<6\ Å}$) being 54–76% of the total pore volume (see Table 2.1). In particular, those (AC-PDEB, AC-CPD91%, and AC-CPD17%) prepared from polymer precursors having high or low cross-linking densities have a monomodal micropore size distribution and have an average micropore size of 4.6–5.0 Å. In particular, with the gradual decrease of cross-linking density from AC-PDEB to AC-CPD84%, the pore volume of micropores less than 4.5 Å ($V_{d<4.5\ Å}$) and its percentage among V_{total} drop significantly (from 0.17 to 0.08 $cm^3\ g^{-1}$ and from 41 to 10%, respectively, see Table 2.1) while those of micropores within 4.5–6 Å ($V_{4.5\ Å<d<6\ Å}$) instead increase pronouncedly (from 0.14 to 0.37 $cm^3\ g^{-1}$ and from 34 to 48%, respectively). Meanwhile, the average micropore size increase from 4.6 to 5.3 Å. These reflect the sensitive, pronounced change in micropore size distribution following the decrease of cross-linking density. Those (from AC-CPD84% to AC-CPD26%) prepared from polymer precursors of intermediate cross-linking densities instead all have a similar bimodal micropore size distribution, with one minor population in the range with size below 4.5 Å (10% of V_{total}) and the other major one in the size range of 4.5–6 Å (notably, *ca.* 48% of V_{total}). In consequence, these activated carbons have a slightly higher average micro- pore size of *ca*. 5.3 Å. These

different micropore size distributions are also reasoned to result from the different cross-linking densities in the polymer precursors. Again, polymers (PDEB and CPD91%) with high cross-linking densities restrict the diffusion of KOH into their matrix for activation during the carbonization while enhanced KOH diffusion occurs within those (CPD84% to CPD26%) of intermediate cross-linking density. With polymers (CPD17%) of low cross-linking density, the collapse of larger micropores occurs, leaving only smaller micropores in the resulting carbons.

Figure 2.S3 shows the mesopore size distribution of the activated carbons. Activated carbons (AC-PDEB, AC-CPD91%, and AC-CPD17%) obtained from polymer precursors of high and low cross-linking densities do not possess significant mesopores with mesopore volume at about 10% of V_{total}. With the gradual decrease of cross-linking density in their polymer precursors from AC-PDEB to AC-CPD84%, the mesopore volume increases from 0.04 to 0.12 $cm^3\ g^{-1}$. Those (AC-CPD84% to AC-CPD26%) obtained from polymers of intermediate cross-linking densities all have similar high mesopore volume (*ca.* 0.12–0.17 $cm^3\ g^{-1}$, at 15–20% of total pore volume). There is a sharp intense peak (within the range of 28–43 Å) in their mesopore distribution curves, with an average mesopore size of 27–36 Å (see Table 2.1). It is generally considered that the mesopores are formed from further activation of micropores through pore widening, fusing, and wall collapsing.[27] The absence of significant mesopores in the former activated carbons (AC-PDEB, AC-CPD91%, and AC-CPD17%) is also attributed to the high cross-linking densities of their polymer precursors or the collapse of pore structures during carbonization. The intermediate levels of cross-linking densities in CPD84% to CPD26% make them most appropriate for the synthesis of activated carbons of high

surface area, high pore volume, and significant mesopores in addition to the dominant micropores. The significant presence of mesopores is deemed particularly important for the application of these porous carbons as the electrode materials for EDLC supercapacitors. Given their unique pronounced effects elucidated above, adjusting the cross-linking density in this family of polymer precursors provides a valuable key to fine tune the textural parameters of the resulting carbon materials.

XRD patterns of representative activated carbons (AC-PDEB and AC-CPD26%) are shown in Figure 2.3. Like the non-activated carbons, the activated carbons are also amorphous with negligible graphitic content on the basis of the very weak broad graphitic peaks near 28° and 50°. Figure 2.4 shows the TEM images taken from selected activated carbons (AC-PDEB, AC-CPD45%, and AC-CPD26%), as well as that of a representative polymer precursor (PDEB). The polymer PDEB appears to be aggregates of many small particles (image (a) in Figure 2.4). A dramatic difference can be noted in the activated carbons made from polymer precursors of different cross-linking densities. In AC-CPD45% and AC-CPD26% obtained from polymer precursors of intermediate cross-linking densities, numerous pores with the size in the range of 10–100 nm can be clearly visualized from the images (images (d) and (f) in Figure 2.4). This provides the further direct evidence confirming the significant presence of both mesopores and macropores in these activated carbons in addition to the dominant micropores, which is consistent with the above results on mesopore size distribution from N_2 sorption. On the contrary, such pore morphology is not seen in the image of AC-PDEB obtained from PDEB of the highest cross-linking density. In agreement with the XRD results, the high-resolution TEM images (images (c) and (e) in Figure 2.4 for AC-PDEB and AC-CPD45%,

respectively) show that both activated carbons are featured with disordered randomly oriented graphene single layers. Apparent oriented multilayer domains and parallel graphene sheets are very few and not apparently distinguishable.

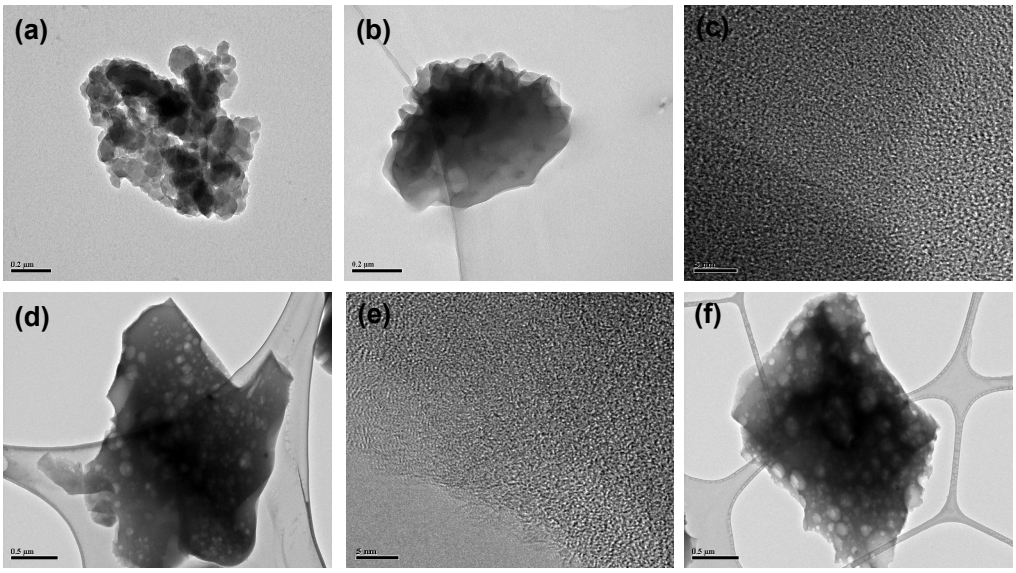

Figure 2.4 TEM images of PDEB (a), AC-PDEB (b and c), AC-CPD45% (d and e), and AC-CPD26% (f). In particular, image (c) is a high-resolution image of AC-PDEB taken from the spot indicated by an arrow in image (b) and image (e) is a high-resolution image of AC-CPD45% taken from the spot indicated by an arrow in image (d). Scale bars: 0.2 μm in (a) and (b); 5 nm in (c) and (e); 0.5 μm in (d) and (f).

XPS measurements were performed on a representative pair of carbon samples, C-CPD45% and AC-CPD45%, to determine their elemental composition and chemical identity. The atomic composition survey reveals that nonactivated C-CPD45% contains C at *ca.* 95% and O at *ca.* 5%, and activated AC-CPD45% contains C at *ca.* 91% and O at *ca.* 8%. The use of KOH during activation clearly enhances the content of O in the activated carbon material. In particular, their C 1s XPS spectra (see Figure 2.S4) confirm the presence of C–OH, C–O and C=O functionalities in both carbon samples.

2.3.2 Electrocapacitive performance of activated carbons as electrode materials for EDLC supercapacitor

Given their high surface area, the various activated carbons obtained above were used as the electrode materials for EDLC supercapacitors. Their electrocapacitive performance was first evaluated with a three-electrode cell in 1 M H_2SO_4 aqueous solution. Electrodes were prepared by loading activated carbons on a titanium foil at a density of *ca.* 1.25 mg cm^{-2} (equivalent thickness of *ca*. 15 μm), which is within the typical range of carbon loading in commercial EDLC supercapacitors.[19] CV, GCD, and EIS measurements were undertaken. Typically, Figure 2.5(a) and (b) show the CV and GCD curves, respectively, of electrodes fabricated with a representative carbon, AC-CPD45%. It can be seen from Figure 2.5(a) that the CV curves are slanted upwards at higher voltage sweep rates (≥25 mV s^{-1}). This indicates that the predominant micropore structures in the carbon restrict the diffusion of ion species at high voltage sweep rates.[28] At lower sweep rates (10 and 5 mV s^{-1}), the curves are more rectangular-like as is expected for ideal ECDL capacitors. Very weak, broad redox peaks at about 0.3 V are present in the CV curve obtained at 5 mV s^{-1} (see inset in Figure 2.5(a)), indicating some functionalization of the carbon sample. From XPS results, the most possible functionalities should be oxygen groups introduced during the activation with KOH. Carbon nanotubes containing oxygen functionalities (such as carbonyl groups) have been shown to exhibit redox peaks at nearly identical positions.[29] Herein, given the very weak nature of these redox peaks, the resulting pseudocapacitance should be marginal and its contribution towards the overall capacitance can be neglected.

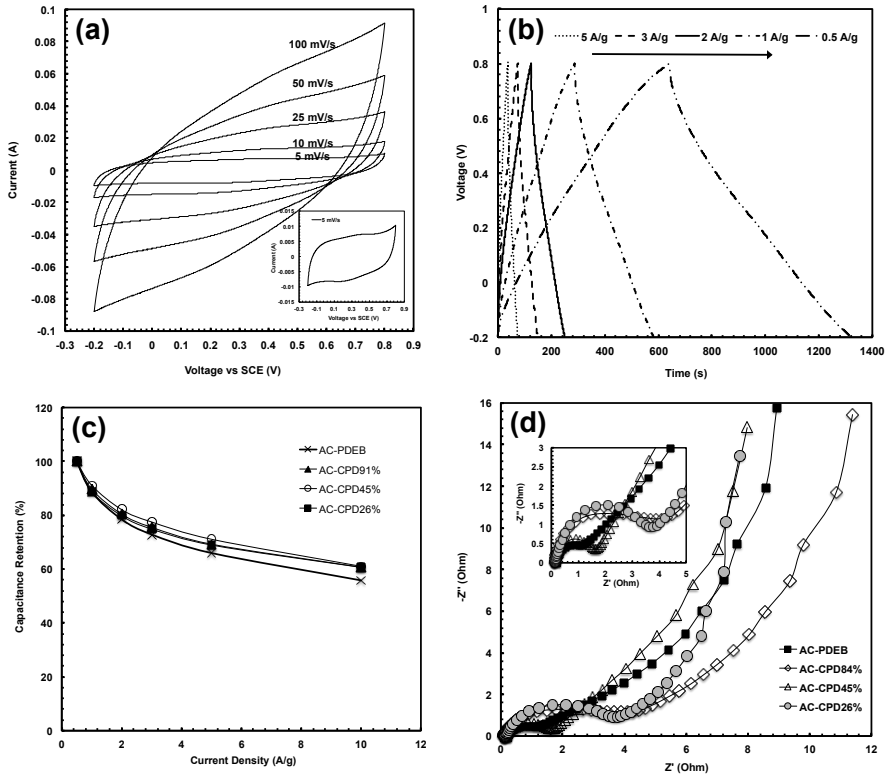

Figure 2.5 (a) Cyclic voltammogram with AC-CPD45% at different scan rates, with inset showing the curve at 5 mV s^{-1}; (b) GCD curves with AC-CPD45% at different current densities; (c) relative specific capacitance obtained from GCD curves (relative to the specific capacitance at 0.5 A g^{-1}) vs. current density for various carbons; (d) Nyquist plot for various carbons, with inset showing the high frequency region. These results were all measured with 3-electrode system in 1 M H_2SO_4 electrolyte.

The GCD curves shown in Figure 2.5(b) generally exhibit a triangle-like shape and show a strong dependence of discharge time on current density. The voltage drop resulting from equivalent series resistance (ESR) is favourably very small (see the curve at 0.5 A g^{-1}), which is also confirmed with EIS to be shown below. Specific capacitance data of the various carbon materials have been calculated from their CV and GCD curves and are listed in Table 2.2. Generally, the activated carbons except AC-CPD17% and AC-CPD8% all show very high specific capacitance values. In particular, AC-CPD8%

showed negligible specific capacitance (<1 F g^{-1} at 0.5 A g^{-1}). From the CV measurements, the specific capacitance is within the ranges of 254–313, 181–220, and 96–186 F g^{-1} at 5, 25, and 100 mV s^{-1}, respectively. From the GCD measurements, the specific capacitance is within the ranges of 350–446, 319–392, and 262–334 F g^{-1} at 0.5, 1, and 3 A g^{-1}, respectively. These specific capacitance values are very high when compared to those reported by others for carbon-based electrode materials in 3-electrode cell in aqueous electrolyte at identical/similar voltage sweep rate or current density (see literature results listed in Table 2.S1). Due to the low surface area and low porosity, the non-activated carbons represented by C-PDEB show low specific capacitance values (*e.g.*, 60 F g^{-1} at 5 mV s^{-1} for C-PDEB) and are thus not further investigated.

Table 2.2 Specific capacitance of carbon samples determined in the 3-electrode cell in 1 M H_2SO_4 aqueous solution

Carbon Sample	Specific Capacitance (F/g)					
	CV@ 5 mV/s	CV @ 25 mV/s	CV @ 100 mV/s	GCD @ 0.5 A/g	GCD @ 1 A/g	GCD @ 3 A/g
C-PDEB	60	35	20			
AC-PDEB	254	181	96	360	319	262
AC-CPD91%	278	233	170	396	354	299
AC-CPD84%	313	260	186	435	392	334
AC-CPD71%	296	198	93	446	384	312
AC-CPD63%	292	220	128	418	366	305
AC-CPD45%	264	206	125	350	319	271
AC-CPD39%	283	207	106	395	358	298
AC-CPD26%	258	202	124	361	321	270
AC-CPD17%	86	85	74	57	43	30

With the increase of cross-linking density in their polymer precursors, the specific capacitance of activated carbons shows a similar trend of change as their specific surface area and pore volume data (see Figure 2.2(b)). From AC-PDEB to AC-CPD91% and to AC-CPD84% obtained from polymers of high cross-linking densities, a gradual increase

in the specific capacitance at all voltage sweep rates or current densities can be noticed. From AC-CPD84% to AC-CPD39% obtained from polymers of intermediate cross-linking densities, the specific capacitance shows only marginal changes without a particular pattern. From AC-CPD39% to AC-CPD17%, a clear consistent drop in specific capacitance is seen. In particular, AC-CPD17% has the smallest capacitance values among all the activated carbons investigated as a result of its low surface area and pore volume. From this trend of change, it can be concluded that the specific capacitance of this family of activated carbons that are predominantly microporous is largely dependent on their surface area or pore volume. Adjusting the cross-linking density of the polymer precursor thus facilitates the tuning of the specific capacitance. Figure 2.5(c) shows the capacitance retention (relative to the values at 0.5 A g^{-1}) at different current densities for four representative carbons, AC-PDEB, AC-CPD91%, AC-CPD45%, and AC-CPD26%. Generally, these activated carbons exhibit similar capacitance retention curves, except the slightly down-shifted curve found with AC-PDEB. At 10 A g^{-1}, AC-CPD91%, AC-CPD45%, and AC-CPD26% all have a capacitance retention of 61% while the value is 56% for AC-PDEB. Though slight, the reduced capacitance retention of AC-PDEB is ascribed to its lowest mesopore surface area and mesopore volume among the four carbons, which lead to more restricted ion movement within the pore structures at high current densities.

Figure 2.5(d) shows the Nyquist plots of four representative activated carbons, AC-PDEB, AC-CPD84%, AC-CPD45%, and AC-CPD26%, obtained from EIS measurements within the frequency range of 10 kHz to 0.01 Hz. All the carbons show the three distinct parts often found with EDLC supercapacitors, with a semicircle at high

frequency, a nearly vertical line at low frequency, and an inclined Warburg-type line (with slope at about 45°) between them at intermediate frequency. The expanded semicircle in the high frequency region is given in the inset. The intercept of the semicircle at real axis (Z') represents the ESR, which is the combination of ionic resistance of the electrolyte, internal resistance of the active material and current collector, and contact resistance at the active material/current collector interface.[30] Low ESR values in the range of 0.1–0.2 Ω are found with all the activated carbons, which are in good agreement with the low voltage drop resulting from ESR noted above in the GCD curves. While the semicircle corresponding to the faradic charge-transfer resistance arises primarily from the ion transport in the mesopores, the Warburg-type line is ascribed to the ion movement within micropores. It can be noted that the length of 45º line is fairly long for all carbons, indicating the slow transport of ions within the micropores of these predominantly microporous carbons. [15b,31,32]

Cyclic stability tests were preformed on two electrodes made with AC-CPD45% and AC-CPD26%, respectively, for 2500 charge–discharge cycles at 1 A g^{-1}. Figure 2.S5 shows the capacitance retention curves. About 93% of the initial capacitance was retained with both electrodes, confirming the excellent electrochemical stability of the electrodes fabricated with these activated carbon materials.

On the basis of above results obtained from 3-electrode cell, we have further fabricated a symmetric two-electrode cell with AC-CPD71% as the electrode materials since it has nearly highest specific capacitance among the activated carbons from the measurements on 3-electrode cell. Electrochemical measurements were performed on the

2-electrode cell in aqueous 1 M H_2SO_4 solution. Figure 2.6 summarizes all the results. From Figure 2.6(a), the CV curve at 5 mV s^{-1} is nearly rectangular as expected for ideal EDLC supercapacitors, giving a specific capacitance of 248 F g^{-1}. From the GCD measurements, the specific capacitance of the cell is 334, 287, 266, and 227 F g^{-1} at 0.1, 0.5, 1, and 3 A g^{-1}, respectively. The capacitance values are relatively lower compared to the corresponding ones measured on AC-CPD71% in 3-electrode cell at the same voltage sweep rate/current density. Often seen with other electrode materials, this should result from the heightened sensitivity of the three-electrode cell as pointed out by Ruoff and Stoller.[19] Compared to the values reported by others for carbon-based electrode materials in 2-electrode cell in aqueous electrolytes at similar voltage sweep rate/current density, the specific capacitance values achieved herein are very high and compete well with those reported in the literature (see literature results listed in Table 2.S2).

From Figure 2.6(c), a high specific capacitance of 176 F g^{-1}, with a percentage of retention of 52%, is achieved at the high current density of 10 A g^{-1}. The Ragone plot correlating the energy density with power density calculated from GCD data is shown in Figure 2.6(d). The highest energy density obtained is 11.6 W h kg^{-1} with a corresponding power density of 25 W kg^{-1} at 0.1 A g^{-1} and drops to 6.1 W h kg^{-1} with a power density of 3060 W kg^{-1} at 10 A g^{-1}. The Nyquist plot (Figure 2.6(e)) of the 2-electrode cell resembles that of the single electrode in 3-electrode cell and is also featured with a relatively long 45° line give the predominantly microporous nature of the carbon. As per the intercept at the real axis, the cell has a higher ESR of 0.37 Ω, about double of that

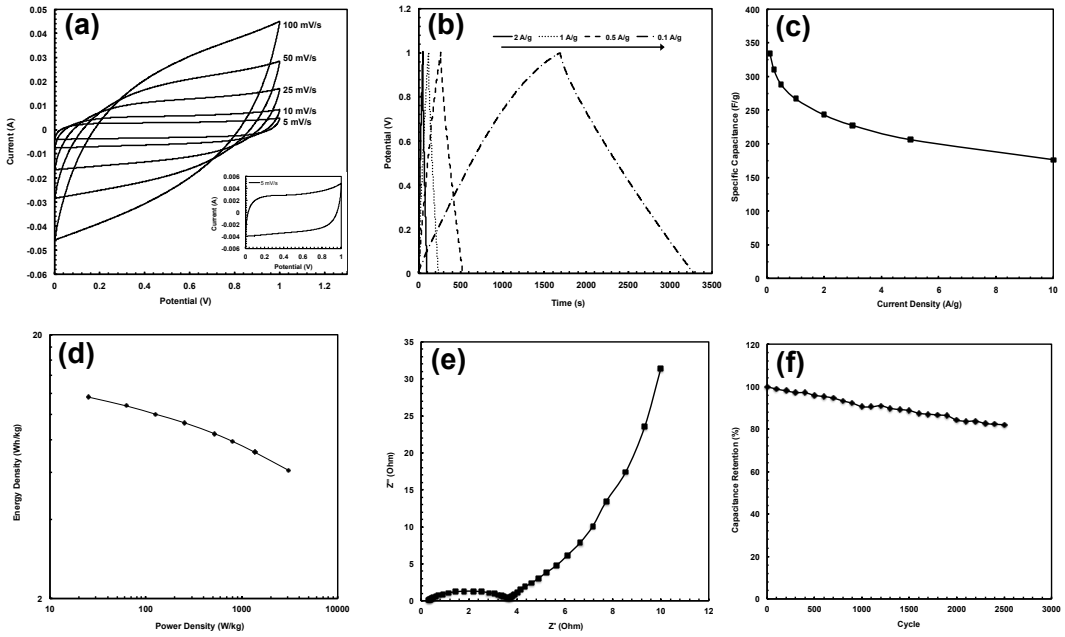

Figure 2.6 Electrochemical results for a symmetrical 2-electrode cell built with AC-CPD71% as electrode materials in 1 M H2SO4: (a) cyclic voltammogram at different voltage sweep rates; (b) GCD curves at different current densities; (c) plot of specific capacitance vs. current density obtained from the GCD data; (d) Ragone plot; (e) Nyquist plot; (f) cyclic stability at the current density of 2 A g-1 over 2500 charge–discharge cycles.

(0.15 Ω) found in the 3-electrode cell. After 2500 charge–discharge cycles at 2 A g^{-1}, the cell maintains good electrochemical stability with 82% of capacitance retained. In summary, all these electrochemical results from both 3-electrode and 2-electrode cells confirm the superior performance (high specific capacitance, excellent stability, and low ESR) of the activated carbons synthesized from this family of polymer precursors as the electrode materials for EDLC supercapacitors, relative to other activated carbons reported in the literature.

2.3.3 Performance of activated carbons for adsorption of H_2 and CO_2

The activated carbons (AC-CPD91% to AC-CPD17%) were subsequently

evaluated as the sorbents for the adsorption of H_2 at 77K (-196°C) and 1 bar, and of CO_2 at 0 °C and 1 bar, with superior performance found in both cases. Figure 2.7(a) shows the H_2 adsorption isotherms of representative activated carbons within the pressure range of 0–1 bar. Hysteresis is absent in the isotherms, confirming reversible adsorption and desorption with these activated carbons. The corresponding adsorption capacity data at 1 bar are listed in Table 2.3. In general, the capacity is in the range of 12.1–13.3 mmol g^{-1} or 2.42–2.66 wt% (except the lower values of 8.6 mmol g^{-1} or 1.73 wt% for AC-CPD17% due to its lower surface area and pore volume), which compete well with the highest values reported in the literature for H_2 adsorption with activated carbons under identical conditions. To the best of our knowledge, the highest H_2 storage capacity of carbon-based materials at 77 K and 1 bar is 3.25 wt% reported by Park *et al*. with a MOF-derived porous carbon (S_{BET} = 3174 m^2 g^{-1}, V_{total} = 4.06 cm^3 g^{-1}, $V_{d<20\ Å}$ = 1.01 cm^3 g^{-1}).[33] Other notable carbons materials with high H_2 storage capacity from special precursors include a H_2-annealed carbide-derived carbon reported by Gogotsi et al.[4a,b] (capacity = 3.0 wt%), MOF-templated nanoporous carbons by Xu et al.[34] (capacity = 2.77 wt%, S_{BET} = 3405 m^2 g^{-1}, V_{total} = 2.58 cm^3 g^{-1}), a super-activated carbide-derived carbon reported by Mokaya *et al*.[35] (capacity = 2.7 wt%, S_{BET} = 2770 m^2 g^{-1}, V_{total} = 1.47 cm^3 g^{-1}, $V_{d<20\ Å}$ = 0.98 cm^3 g^{-1}, maxima micropore size = 12 Å). The highest H_2 storage capacity reported for activated carbons obtained directly from common carbon precursors in the literature at identical conditions is 2.55 wt% achieved by Chen *et al*. with a biomass-derived microporous carbon (S_{BET} = 3100 m^2 g^{-1}, V_{total} = 1.68 cm^3 g^{-1}, maximum distributed pore size of total 9.1 Å).[36] With a high-surface-area activated carbon after further KOH activation (S_{BET} = 3190 m^2 g^{-1}, V_{total} = 1.69 cm^3 g^{-1}, $V_{d<20\ Å}$ = 1.09 cm^3 g^{-1}, HK median micropore size of 6.7 Å), Gao *et al*. reported a high H_2 storage

capacity of 2.49 wt% at77K and 1 bar.[37]

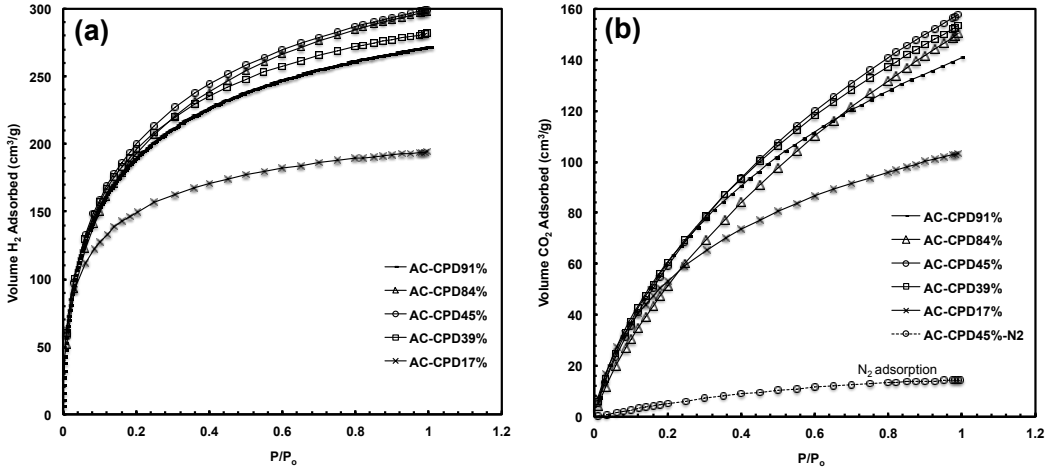

Figure 2.7 a) Hydrogen adsorption isotherms of five representative carbon materials from 0 to 1 bar at 77 K; (b) their CO_2 adsorption isotherms from 0 to 1 bar at 0 °C, with the N_2 adsorption isotherm for AC-CPD45% at identical conditions included for comparison.

Given their significantly lower surface area and pore volume (1292–1418 $m^2\ g^{-1}$ and 0.77 $cm^3\ g^{-1}$, respectively) in comparison with the activated carbons used in the literature, the higher H_2 storage capacity (2.66 wt%) achieved herein with our activated carbons (AC-CPD84% to AC-CPD39%) is highly remarkable. This is believed to result from their unique textural properties elucidated earlier, including high microporosity ($V_{d<2\ nm}/V_{total}$ = 78–84%), matching median micropore size (5.3 Å) that is close to the optimum size of about 6–7 Å for hydrogen storage,[4] and narrow micropore size distribution with the majority of micropores having the size below 6 Å ($V_{d<6\ Å}/V_{total}$ = 55–68%). Figure 2.8(a) shows the correlations between the H_2 adsorption capacity with various pore volume data (V_{total}, $V_{d<20\ Å}$, $V_{d<6\ Å}$, $V_{4.5\ Å<d<6\ Å}$) for this range of activated carbons. It can be seen that the correlation with $V_{d<6\ Å}$ provides the best linear fit with the

highest R^2 value among the four different correlations, with the adsorption capacity increasing linearly with $V_{d<6\ Å}$. This also indicates that the micropores smaller than 6 Å are most important in effecting H_2 adsorption.

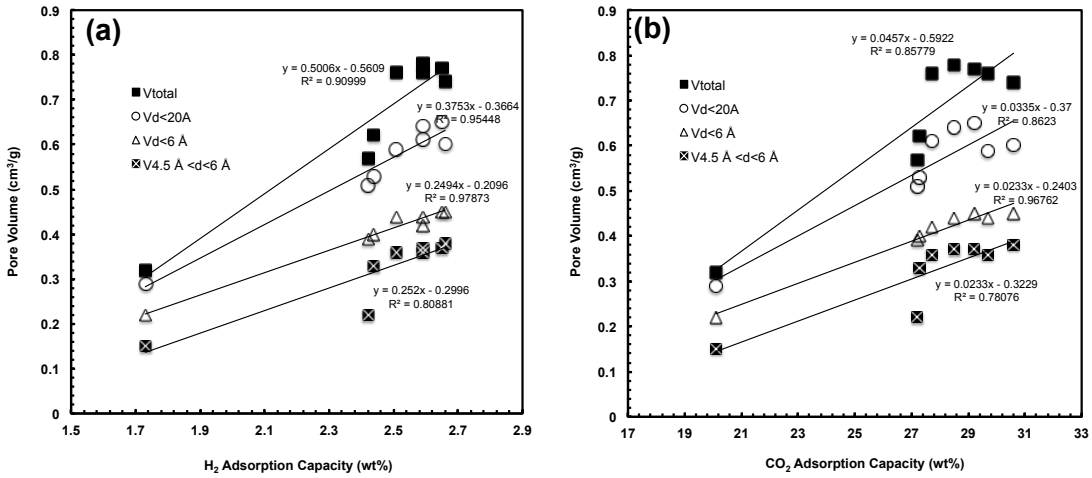

Figure 2.8 Correlations of the adsorption capacity of the activated carbons for (a) H_2 and (b) CO_2 with their pore volume data, including total pore volume (Vtotal), micropore volume($V_{d<20\ Å}$), volume of micropores smaller than 6 Å ($V_{d<6\ Å}$), and volume of micropores between 4.5 and 6 A˚($V_{4.5\ Å<d<6\ Å}$).

Figure 2.7(b) shows the CO_2 adsorption isotherms of representative carbons within 0–1 bar at 0 °C, where hysteresis is also absent. The adsorption capacity data at 1 bar are also included in Table 2.3. All activated carbons except AC-CPD17% possess high capacity for CO_2 adsorption (6.19–6.95 mmol g^{-1} or 27.2– 30.6 wt%). In CO_2 capture from flue gas, the selectivity of sorbents towards CO_2 relative to other species such as N_2 is also critically important besides the adsorption capacity.[5d] In order to investigate the CO_2/N_2 selectivity of the activated carbons herein, a typical N_2 adsorption was also undertaken with AC-CPD45%, which shows the highest CO_2 adsorption

capacity of 6.95 mmol g^{-1} among all the carbons herein, at identical conditions. The isotherm is also displayed in Figure 2.7(b), with the adsorbed amount of 0.64 mmol g^{-1} at 1 bar. Calculated on the basis of the amounts adsorbed at 1 bar, the CO_2/N_2 selectivity is 11 (mol per mol), which is high for pure carbon-based sorbents. At 0 °C and 1 bar, the highest CO_2 adsorption capacity reported for carbon-based materials to date is 8.9 mmol g^{-1} achieved by Jaroniec and Wickramaratne with KOH-activated phenolic resin-based carbon spheres (S_{BET} = 2400 $m^2\,g^{-1}$, V_{total} = 1.07 $cm^3\,g^{-1}$).[5c] Its CO_2/N_2 selectivity was not directly disclosed in their report. But as per our estimation from their presented experimental data, the CO_2/N_2 selectivity with their carbon spheres is well below 1.0, which is very low. A high capacity of 8.64 mmol g^{-1} was also achieved by Silvestre-Albero *et al*. with an activated carbon obtained from petroleum pitch precursors (S_{BET} = 2450 $m^2\,g^{-1}$, V_{total} = 1.12 $cm^3\,g^{-1}$, $V_{d<20\ Å}$ = 1.03 $cm^3\,g^{-1}$), but also at a low CO_2/N_2 selectivity of 2.8.[5d] In addition, the adsorption capacity of up to 7.09 mmol g^{-1} was reported by Gogotsi *et al*. with carbide-derived carbons, but with no information given on the selectivity.[5a]

Compared to these literature data, the high CO_2 adsorption capacity (up to 6.95 mmol g^{-1}) in combination with the high CO_2/N_2 selectivity (11) makes the activated carbons synthesized herein from the family of cross-linked DEB–PA copolymers highly unique. Given their significantly lower surface area and pore volume relative to the above-mentioned carbons reported in the literature for high-capacity CO_2 adsorption, their unique textural properties mentioned above in H_2 adsorption are also reasoned to render their superior CO_2 adsorption properties. Based on the study with carbide-derived carbons, CO_2 uptake at 1 bar and 77 K correlates with the volume of micropores smaller

than 8 Å and the uptake at 0.1 bar and 77 K correlates with the volume of micropores smaller or equal to 5 Å.[5a] The matching micropore size and narrow micropore size distribution in these activated carbons clearly contributes their high CO_2 adsorption capacity. Figure 2.8(b) shows the correlations of CO_2 adsorption capacity with different pore volume data. Similar to that in H_2 adsorption, the best-fitting linear correlation is with $V_{d<6\ Å}$, which is consistent with literature results and confirms the important role of these micropores for CO_2 adsorption.

Meanwhile, the high CO_2/N_2 selectivity found with AC-CPD45% also suggests that the micropores within this range of activated carbons also have a good molecular sieving effect and can discriminate the molecules on a shape and/or size basis.

2.4 Conclusions

A family of cross-linked polymers (PDEB and CPD91%–CPD8%) having different cross-linking densities has been synthesized from DEB and PA via catalytic polymerization and has been demonstrated as the novel polymer precursors for high-yield synthesis of nanoporous carbons. In the absence of any activation agent, carbonization of the polymers renders low-surface area carbons (S_{BET} up to 500 $m^2\ g^{-1}$, V_{total} up to 0.31 $cm^3\ g^{-1}$) at a high yield up to 85% depending on the cross-linking density. Carbonization of the polymers in the presence of KOH as the activation agent gives rise to predominantly microporous activated carbons of significantly enhanced surface area (S_{BET} up to 1418 $m^2\ g^{-1}$) and pore volume (V_{total} up to 0.78 $cm^3\ g^{-1}$) while at high yields (*ca*. 70% for PDEB and CPD91%–CPD26%). Textural properties of the resulting activated carbons depend sensitively on the cross-linking density of the polymer

precursor. For polymers of high cross-linking density (PDEB, AC-CPD91%), the gradual decrease of cross-linking density leads to enhanced surface area, pore volume, median micropore size, and the evolvement of mesopores/macropores. Activated carbons obtained from polymers with intermediate cross-linking densities (AC-CPD84% to AC-CPD26%) show similar textural properties with little effects from the change in cross-linking density. For those with low cross-linking densities (AC-CPD17% and AC-CPD8%), the occurrence of severe structural collapse during carbonization due to insufficient cross-linking results in low-surface-area carbons instead.

The high-surface-area activated carbons obtained from this family of polymer precursors have been demonstrated to possess superior performance properties both as electrode materials in EDLC supercapacitors and as sorbents for H_2 and CO_2 adsorption. As electrode materials, high specific capacitance values (up to 446 F g^{-1} at 0.5 A g^{-1} in 3-electrode cell; 334 F g^{-1} at 0.1 A g^{-1} and 287 F g^{-1} at 0.5 A g^{-1} in 2-electrode cell) have been achieved and they are comparable to the best values achieved with carbon-based materials in 1 M H_2SO_4 at similar conditions to date. As the sorbents, the activated carbons have been demonstrated to show high capacities for the adsorption of both H_2 and CO_2 (up to 2.66 wt% for H_2 adsorption at 77 K and 1 bar; up to 6.95 mmol g^{-1} along with a high CO_2/N_2 selectivity of 11 for CO_2 adsorption at 0 °C and 1 bar), which are comparable to or even better than those achieved with best-performing activated carbons to date. These combined remarkable performance properties are ascribed to their unique textural properties, including desired micropore size matching the optimum ones and narrow micropore size distribution.

2.5 References

(1) Representative reviews on hydrogen storage: (a) A. F. Dalebrook, W. Gan, M. Grasemann, S. Moret and G. Laurenczy, *Chem. Commun.*, 2013, **49**, 8735–8751; (b) L. Wang and R. T. Wang, *Energy Environ. Sci.*, 2008, **1**, 268–279; (c) L. Zubizarreta, A. Arenillas and J. J. Pis, *Int. J. Hydrogen Energy*, 2009, **34**, 4575–4581; (d) R. Ströbel, J. Garche, P. T. Moseley, L. Jörissen and G. Wolf, *J. Power Sources*, 2006, **159**, 781–801; (e) Y. Yürüm, A. Taralp and T. N. Veziroglu, *Int. J. Hydrogen Energy*, 2009, **34**, 3784–3798.

(2) Representative reviews on EDLC supercapacitors: (a) P. Simon and Y. Gogotsi, *Nature Mater.*, 2008, **7**, 845–854; (b) L. L. Zhang and X. S. Zhao, *Chem. Soc. Rev.*, 2009, **38**, 2520–2531; (c) L. L. Zhang, Y. Gu and X. S. Zhao, *J. Mater. Chem. A*, 2013, **1**, 9395–9408; (d) P. Simon and Y. Gogotsi, *Acc. Chem. Res.*, 2013, **46**, 1094–1103; (e) Y. Zhai, Y. Dou, D. Zhao, P. F. Fulvio, R. T. Mayes and S. Dai, *Adv. Mater.* 2011, **23**, 4828–4850; (f) G. Wang, L. Zhang and J. Zhang, *Chem. Soc. Rev.*, 2012, **41**, 797–8281; (g) F. Béguin, V. Presser, A. Balducci and E. Frackowiak, *Adv. Mater.* 2014, **26**, 2219–2251; (h) L. Borchardt, M. Oschatz and S. Kaskel, *Mater. Horiz.*, 2014, **1**, 157–168; (i) M. Inagaki, H. Konno and O. Tanaike, *J. Power Sources*, 2010, **195**, 7880–7903.

(3) Representative reviews on CO_2 capture with different sorbents: (a) S. Choi, J. H. Drese and C. W. Jones, *ChemSusChem*, 2009, **2**, 796–854; (b) N. Hedin, L. Chen and A. Laaksonen, *Nanoscale*, 2010, **2**, 1819–1841; (c) Y.-S. Bae and R. Q. Snurr, *Angew. Chem. Int. Ed.*, 2011, **50**, 11586–11596; (d) J. Liu, P. K. Thallapally, B. P. McGrail, D. R. Brown and J. Liu, *Chem. Soc. Rev.*, 2012, **41**, 2308–2322.

(4) Representative papers on pore size effect on H_2 adsorption: (a) Y. Gogotsi, R. K. Dash, G. Yushin, T. Yildirim, G. Laudisio and J. E. Fischer, *J. Am. Chem. Soc.*, 2005, **127**, 16006–16007; (b) G. Yushin, R. Dash, J. Jagiello, J. E. Fischer, Y. Gogotsi, *Adv. Funct. Mater.*, 2006, **16**, 2288–2293; (c) Y. Gogotsi, C. Portet, S. Osswald, J. M. Simmons, T. Yildirim, G. Laudisio and J. E. Fischer, *Int. J. Hydrogen Energy*, 2009, **34**, 6314–6319; (d) N. Texier-Mandoki, J. Dentzer, T. Piquero, S. Saadallah, P. David and C. Vix-Guterl, *Carbon*, 2004, **42**, 2735–2777; (e) K. Xia, Q. Gao, C. Wu, S. Song and M. Ruan, *Carbon*, 2007, **45**, 1989–1996; (f) Z. Yang, Y. Xia and R. Mokaya, *J. Am. Chem. Soc.*, 2007, **129**, 1673–1679.

(5) Representative papers on pore size effect on CO_2 capture: (a) V. Presser, J. McDonough, S.-H. Yeon and Y. Gogotsi, *Energy Environ. Sci.*, 2011, **4**, 3059–3066; (b) J. Silvestre-Alberto, A. Wahby, A. Sepúlveda-Escribano, M. Martínez-Escandell, K. Kaneko and F. Rodríguez-Reinoso, *Chem. Commun.*, 2011, **47**, 6840–6842; (c) N. P. Wickramaratne and M. Jaroniec, *J. Mater. Chem. A*, 2013, **1**, 112–116; (d) A. Wahby, J. M. Ramos-Fernández, M. Martínez-Escandell, A. Sepúlveda-Escribano and F. Rodríguez-Reinoso, *ChemSusChem*, 2010, **3**, 974–981; (e) X. Hu, M. Radosz, K. A. Cychosz and M. Thommes, *Environ. Sci. Tech.*, 2011, **45**, 7068–7074.

(6) Representative papers on pore size effect on the electrocapacitive performance of nanostructured porous carbons: (a) J. Chmiola, G. Yushin, Y. Gogotsi, C. Portet, P. Simon and P. L. Taberna, *Science* 2006, **313**, 1760–1762; (b) C. R. Pérez, S.-H. Yeon, J. Ségalini, V. Presser, P.-L. Taberna, P. Simon and Y. Gogotsi, *Adv. Funct. Mater.*, 2013, **23**, 1081–1089; (c) C. Largeot, C. Portet, J. Chmiola, P. L. Taberna, Y. Gogosti and P. Simon, *J. Am. Chem. Soc.*, 2008, **130**, 2730–2731; (d) J. Chmiola, C. Largeot, P. L. Taberna, P. Simon and Y. Gogosti, *Angew. Chem. Int. Ed.*, 2008, **47**,

3392–3395; (e) Y. Korenbit, M. Rose, E. Kockrick, L. Borchardt, A. Kvit, S. Kaskel and G. Yushin, *ACS Nano*, 2010, **4**, 1337–1344; (f) D.-D. Zhou, Y.-J. Du, Y.-F. Song, Y.-G. Wang, C.-X. Wang and Y.-Y. Xia, *J. Mater. Chem. A*, 2013, **1**, 1192–1200; (g) L. Zhang, X. Yang, F. Zhang, G. Long, T. Zhang, K. Leng, Y. Zhang, Y. Huang, Y. Ma, M. Zhang and Y. Chen, *J. Am. Chem. Soc.*, 2013, **135**, 5921–5929; (h) J. Chmiola, G. Yushin, R. Dash and Y. Gogotsi, *J. Power Sources*, 2006, **158**, 765–772.

(7) (a) J. Lee, J. Kim and T. Hyeon, *Adv. Mater.*, 2006, **18**, 2073–2094; (b) V. Presser, M. Heon and Y. Gogotsi, *Adv. Funct. Mater.*, 2011, **21**, 810–833; (c) H. Nishihara and T. Kyotani, *Adv. Mater.*, 2012, **24**, 4473–4498; (d) B. Fang, J. H. Kim, M.-S. Kim and J.-S. Yu, *Acc. Chem. Res.*, 2013, **46**, 1397–1406; (e) C. Liang, Z. Li and S. Dai, *Angew. Chem. Int. Ed.*, 2008, **47**, 3696–3717; (f) T.-Y. Ma, L. Liu and Z.-Y. Yuan, *Chem. Soc. Rev.*, 2013, **42**, 3977–4003; (g) W. J. Lee, U. N. Maiti, J. M. Lee, J. Lim, T. H. Han and S. O. Kim, *Chem. Commun.*, 2014, **50**, 6818–6830; (h) C. Xu, B. Xu, Y. Gu, Z. Xiong, J. Sun and X. S. Zhao, *Energy Environ. Sci.*, 2013, **6**, 1388–1414.

(8) (a) T. N. Hoheisel, S. Schrettl, R. Szilluweit and H. Frauenrath, *Angew. Chem. Int. Ed.,* 2010, **49**, 6496–6515; (b) T.-P. Fellinger, A. Thomas, J. Yuan and M. Antonietti, *Adv. Mater.*, 2013, **25**, 5838–5855; (c) J. P. Paraknowitsch and A. Thomas, *Macromol. Chem. Phys.* 2012, **213**, 1132−1145; (d) J. S. Lee, X. Wang, H. Luo, G. A. Baker and S. Dai, *J. Am. Chem. Soc.*, 2009, **131**, 4596−4597; (e) S. Zhang, M. S. Miran, A. Ikoma, K. Dokko and M. Watanabe, *J. Am. Chem. Soc.*, 2014, **136**, 1690−1693.

(9) See a review: L. Wei and G. Yushin, *Nano Energy*, 2012, **1**, 552–565.

(10) (a) T. Kowalewski, N. V. Tsarevsky and K. Matyjaszewski, *J. Am. Chem. Soc.*, 2002, **124**, 10632−10633; (b) B. Saha and G. C. Schatz, *J. Phys. Chem. B*, 2012, **116**, 4684−4692; (c) M. S. A. Rahaman, A. F. Ismail and A. Mustafa, *Polym. Degrad. Stab.*, 2007, **92**, 1421−1432.

(11) (a) C. Liang, K. Hong, G. A. Guiochon, J. W. Mays and S. Dai, *Angew. Chem. Int. Ed.*, 2004, **43**, 5785−5789; (b) C. Lei, N. Amini, F. Markoulidis, P. Wilson, S. Tennison and C. Lekakou, *J. Mater. Chem. A*, 2013, **1**, 6037−6042; (c) A. M. ElKhatat and S. A. Al-Muhtaseb, *Adv. Mater.*, 2011, **23**, 2887–2903.

(12) D. Hulicova-Jurcakova, A. M. Puziy, O. I. Poddubnaya, F. Suárez-Garcíia, J. M. D. Tascón and G. Q. Lu, *J. Am. Chem. Soc.*, 2009, **131**, 5026−5027.

(13) (a) R. Janus, A. Wach, P. Kustrowski, B. Dudek, M. Drozdek, A. M. Silvestre-Albero, F. Rodríguez-Reinoso and Pegie Cool, *Langmuir*, 2013, **29**, 3045−3053; (b) M. Choura, N. M. Belgacem and A. Gandini, *Macromolecules*, 1996, **29**, 3839–50.

(14) (a) Q. Zhao, T.-P. Fellinger, M. Antonietti and J. Yuan, *J. Mater. Chem. A*, 2013, **1**, 5113−5120; (b) D. Puthusseri, V. Aravindan, S. Madhavi and S. Ogale, *Energy Environ. Sci.*, 2004, **7**, 728−735.

(15) (a) W. Chaikittisilp, M. Hu, H. Wang, H.-S. Huang, T. Fujita, K. C.-W. Wu, L.-C. Chen, Y. Yamauchi and K. Ariga, *Chem. Commun.*, 2012, **48**, 7259−7261; (b) J. Hu, H. Wang, Q. Gao and H. Guo, *Carbon*, 2010, **48**, 3599−3606; (c) A. J. Amali, J.-K. Sun and Q. Xu, *Chem. Commun.*, 2014, **50**, 1519−1522; (d) N. L. Torad, R. R. Salunkhe, Y. Li, H. Hamoudi, M. Imura, Y. Sakka, C.-C. Hu and Y. Yamauchi, *Chem. Eur. J.*, 2014, **20**, 7895–7900.

(16) J. Sun, G. Wu and Q. Wang, *J. Mater. Sci.*, 2005, **40**, 663−668.

(17) T. Horikawa, K. Ogawa, K. Mizuno, J. Hayashi and K. Muroyama, *Carbon*, 2003, **41**, 465–472.

(18) (a) G. F. Levchik, K. Si, S. V. Levchik, G. Camino and C. A. Wikle, *Polym. Degrad. Stab.*, 1999, **65**, 395−403; (b) Y. Li, Y. Fan and J. Ma, *Polym. Degrad. Stab.*, 2001, **73**, 163–167; (c) F. M. Uhl, G. F. Levchik, S. V. Levchik, C. Dick, J. J. Liggat, C. E. Snape and C. A. Wilkie, *Polym. Degrad. Stab.*, 2001, **71**, 317–325.

(19) M. D. Stoller and R. S. Ruoff, *Energy Environ. Sci.*, 2010, **3**, 1294–1301.

(20) Z. Dong and Z. Ye, *Macromolecules*, 2012, **45**, 5020−5031.

(21) (a) A. Goto, M. Kyotani, K. Tsugawa, G. Piao, K. Akagi and Y. Koga, *Carbon*, 2001, **39**, 2082−2086; (b) A. Goto, M. Kyotani, K. Tsugawa, G. Piao, K. Akagi, C. Yamaguchi, H. Matsui and Y. Koga, *Carbon*, 2003, **41**, 131−138.

(22) S. Rondeau-Gagné and J.-F. Morin, *Chem. Soc. Rev.*, 2014, **43**, 85−98.

(23) K. S. W. Sing, D. H. Everett, R. A. W. Haul, L. Moscou, R. A. Pierotti, J. Rouquerol and T. Siemieniewska, *Pure Appl. Chem.*, 1985, **57**, 603−619.

(24) L. Xu, J.-W. McGraw, F. Gao, M. Grundy, Z. Ye, Z. Gu and J. L. Shepherd, *J. Phys. Chem. C*, 2013, **117**, 10730−10742.

(25) S. B. Yoon, G. S. Chai, S. K. Kang, J.-S. Yu, K. P. Gierszal and M. Jaroniec, *J. Am. Chem. Soc.*, 2005, **127**, 4188−4189.

(26) M.A. Lillo-Ródenas, D. Cazorla-Amorós and A. Linares-Solano, *Carbon*, 2003, **41**, 267−275.

(27) N. Shiratori, K. J. Lee, Jin. Miyawaki, S.-H. Hong, I. Mochida, B. An, K. Yokogawa, J. Jang and S.-H. Yoon, *Langmuir*, 2009, **25**, 7631–7637.

(28) L.-F. Chen, X.-D. Zhang, H.-W. Liang, M. Kong, Q.-F. Guan, P. Chen, Z.-Y. Wu and S.-H. Yu, *ACS Nano*, 2012, **6**, 7092–7102.

(29) H. Pan, C. K. Poh, Y. P. Feng and J. Lin, *Chem. Mater.*, 2007, **19**, 6120–6125.

(30) L. Wei, M. Sevilla, A. B. Fuertes, R. Mokaya and G. Yushin, *Adv. Funct. Mater.*, 2012, **22**, 872–834.

(31) X. Yang, J. Zhu, L. Qiu and Dan Li, *Adv. Mater.*, 2011, **23**, 2833–2838.

(32) H. Wang, Z. Xu, A. Kohandehghan, Z. Li, K. Cui, X. Tan, T. J. Stephenson, C. K. King'ondu, C. M. B. Holt, B. C. Olsen, J. K. Tak, D. Harfield, A. O. Anyia and D. Mitlin, *ACS Nano*, 2013, **7**, 5131–5141.

(33) S. J. Yang, T. Kim, J. H. Im, Y. S. Kim, K. Lee, H. Jung and C. R. Park, *Chem. Mater.*, 2012, **24**, 464–470.

(34) H.-L. Jiang, B. Liu, Y.-Q. Lan, K. Kuratani, T. Akita, H. Shioyama, F. Zong and Q. Xu, *J. Am. Chem. Soc.*, 2011, **133**, 11854–11857.

(35) M. Sevilla, R. Foulston and R. Mokaya, *Energy Environ. Sci.*, 2010, **3**, 223–227.

(36) F. Cheng, J. Liang, J. Zhao, Z. Tao and J. Chen, *Chem. Mater.*, 2008, **20**, 1889–1895.

(37) H. Wang, Q. Gao and J. Hu, *J. Am. Chem. Soc.*, 2009, **131**, 7016–7022.

2.6 Supporting Information

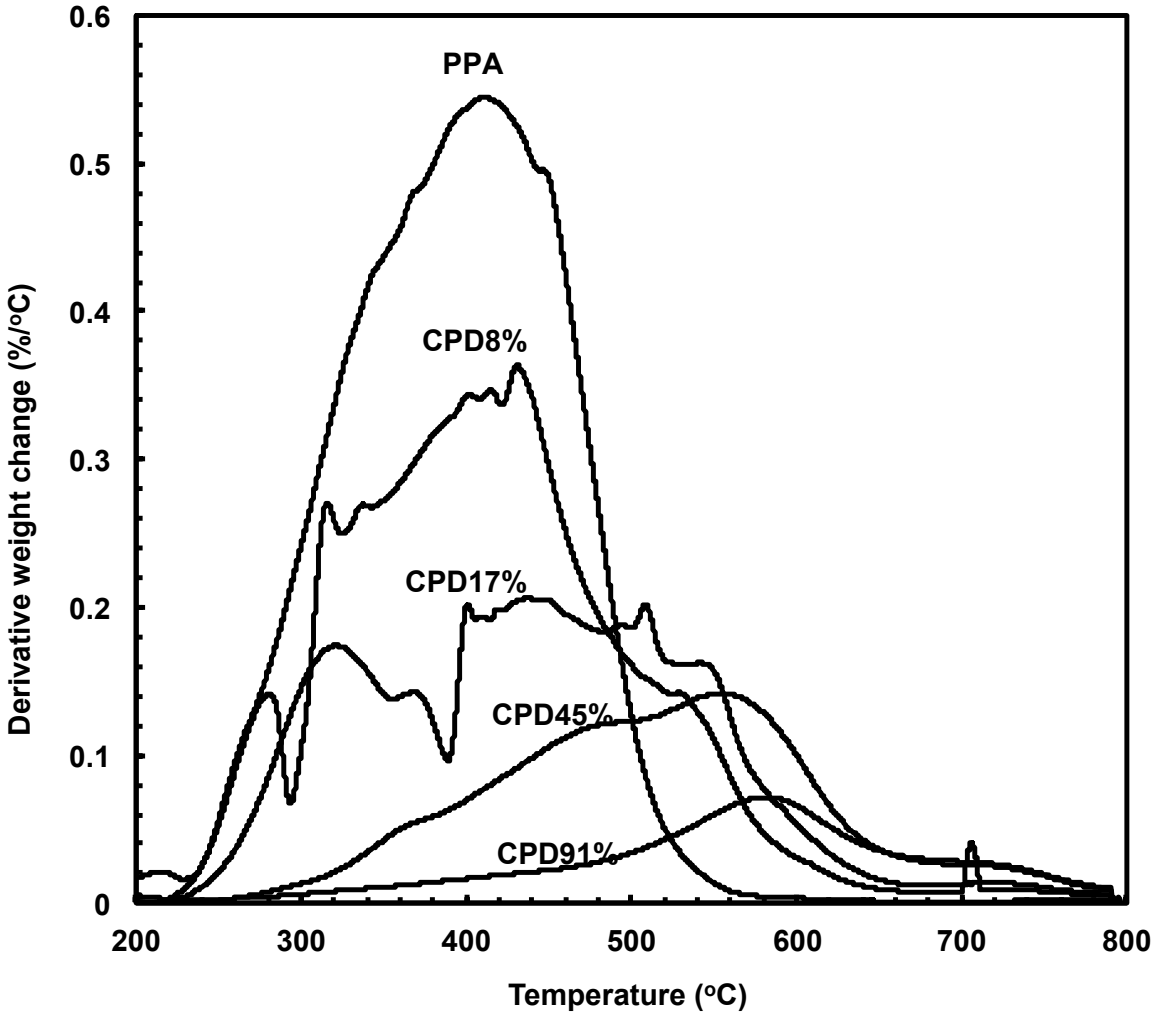

Figure 2.S1 First-order derivative TGA curves of representative polymers (corresponding to the TGA curves in Figure 1).

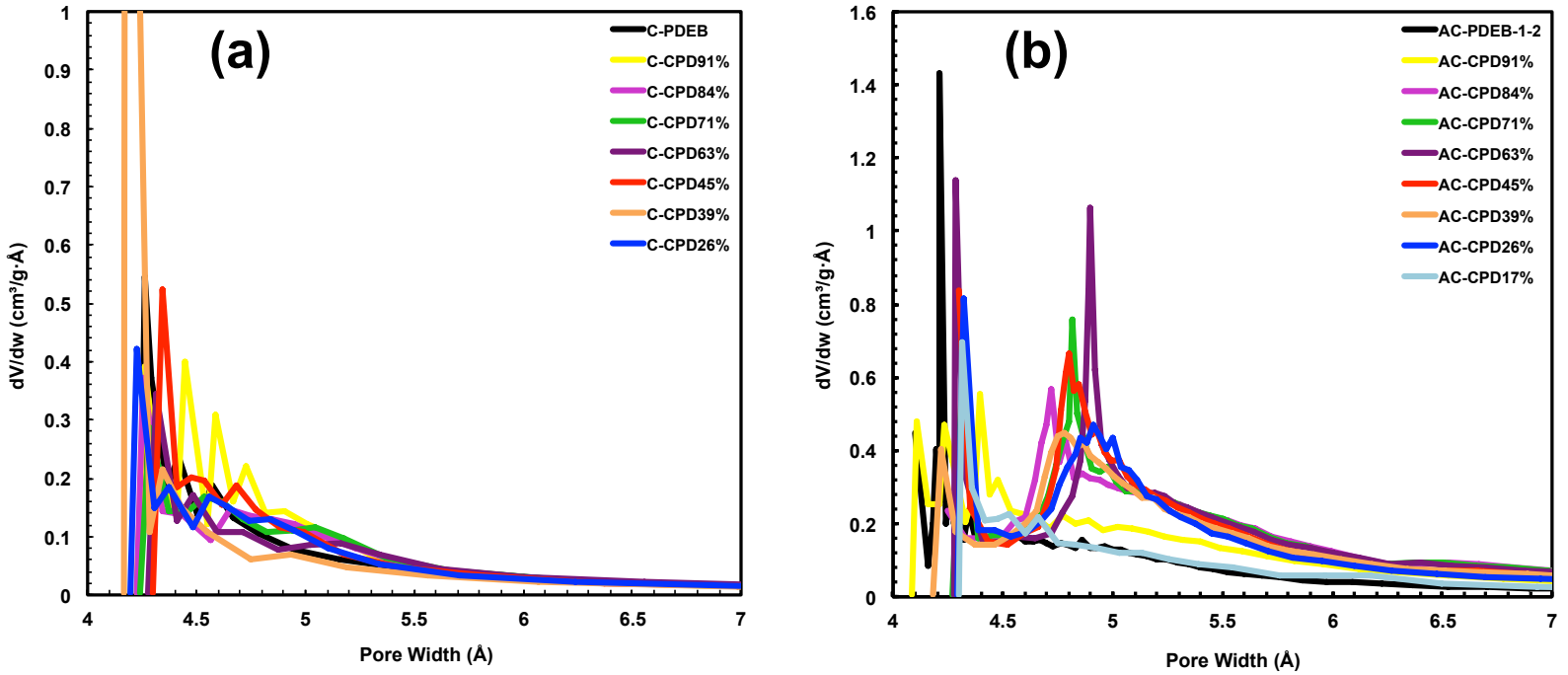

Figure 2.S2 Micropore size distribution curves of (a) the nonactivated carbons and (b) activated carbons determined from N_2 sorption isotherm ($P/P_o < 0.02$) with the HK model.

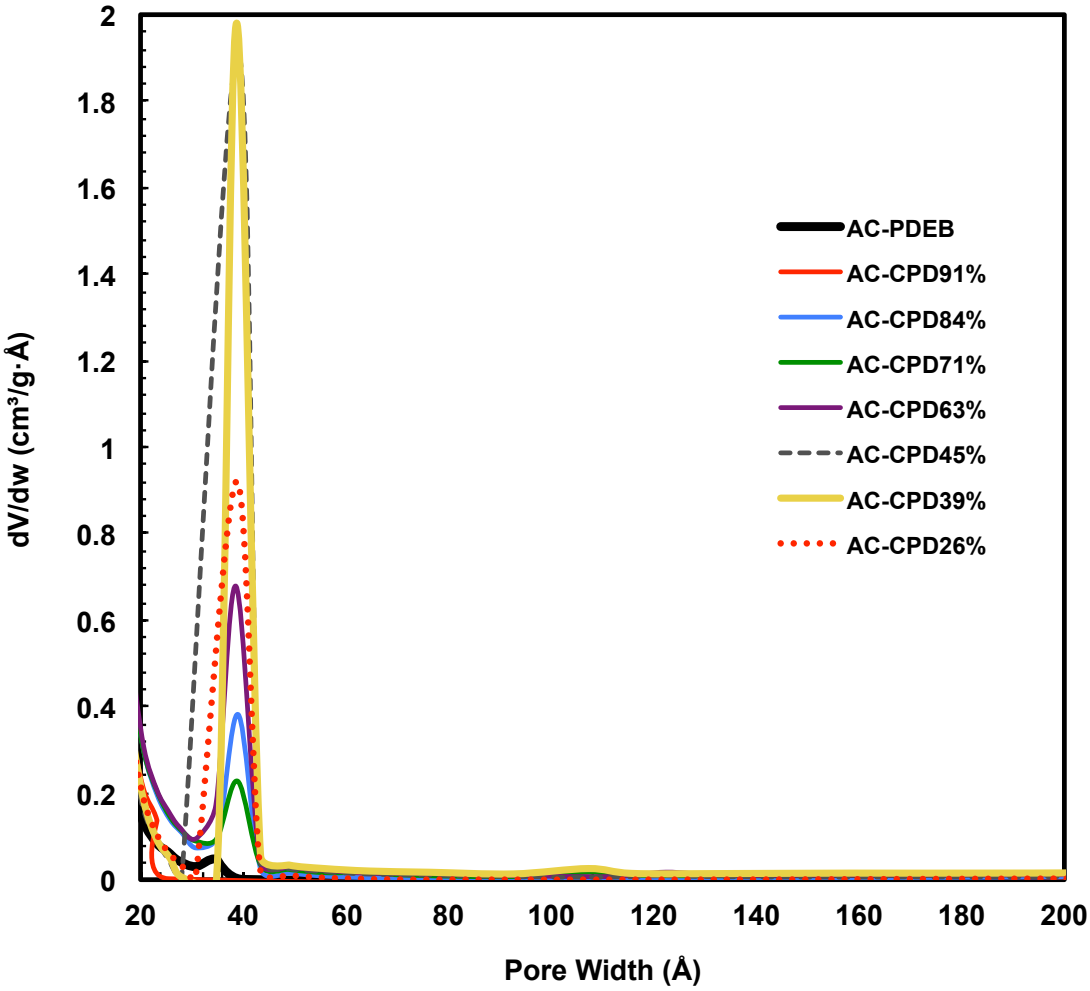

Figure 2.S3 Mesopore size distribution of the activated carbons determined from N_2 desorption data with BJH model.

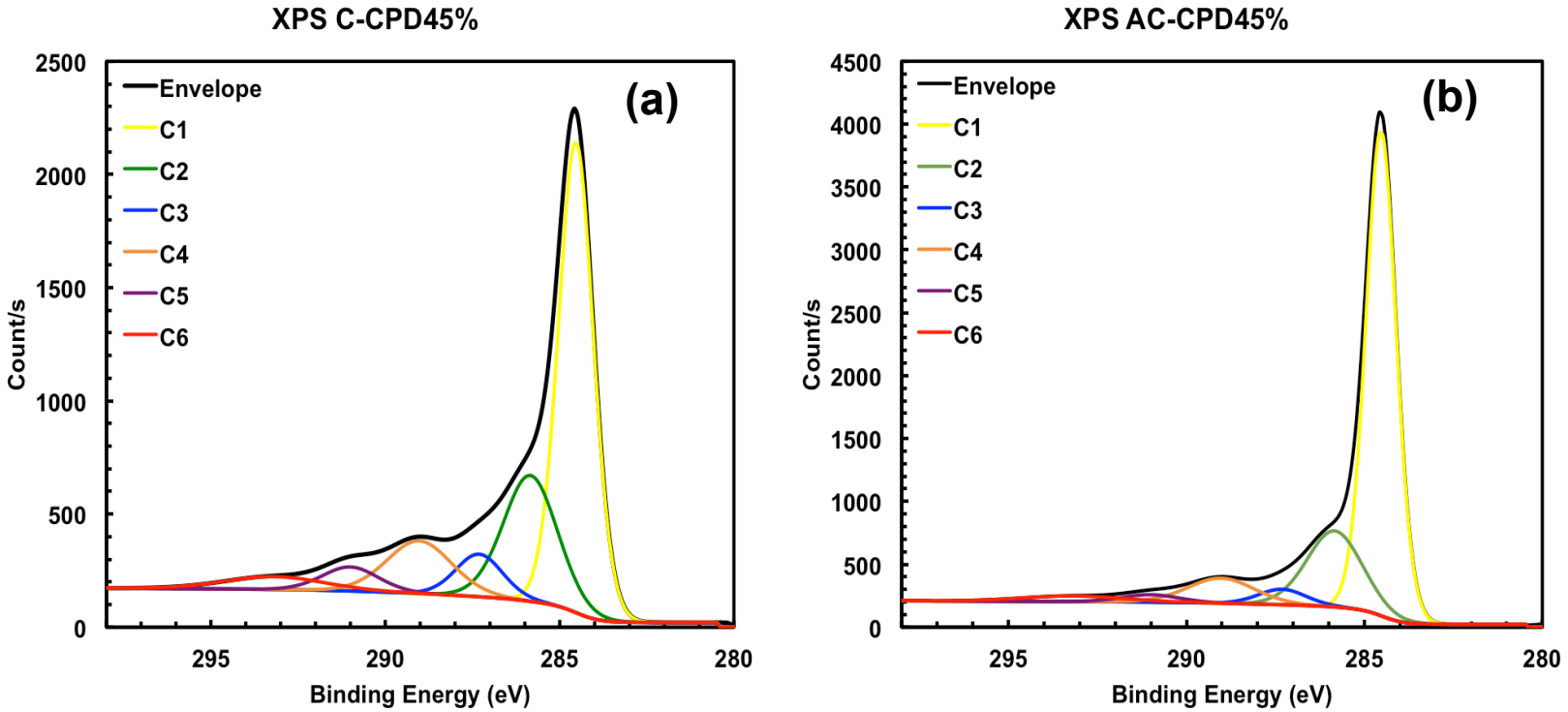

Figure 2.S4 C 1s XPS spectra of (a) C-CPD45% and (b) AC-CPD45%. Peaks labeled as C1–C4 (binding energy at 284.53, 285.84, 287.31, 289.03 eV, respectively) arise, respectively, from the sp3 C–C and sp2 C=C, C–OH, C=O, O–C=O functional groups. Peaks C5 (291.01 eV) and C6 (293.19 eV) are satellite peaks resulting from π-π* electronic transition (see Ref. 13 and 15d in the article). The atomic content of C1–C6 in C-CPD45% is 65.8%, 18.8%, 3.3%, 7.5%, 1.9%, and 2.6%, respectively; and the corresponding content in AC-CPD45% is 52.4%, 21.8%, 6.4%, 11.0%, 4.3%, and 4.1%, respectively.

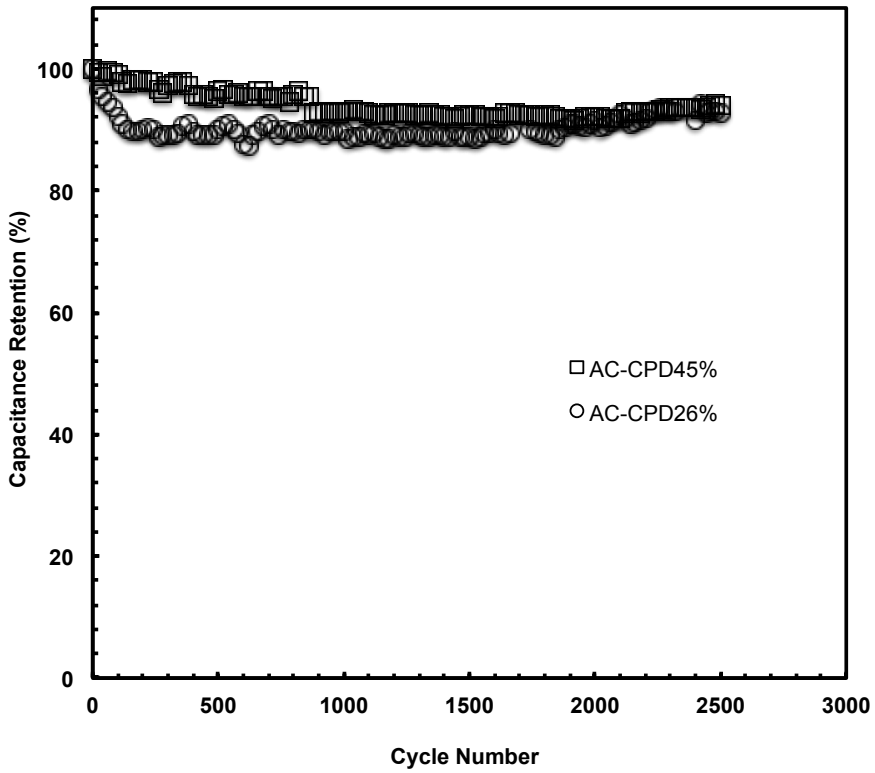

Figure 2.S5 Cyclic stability of electrodes made with AC-CPD45% and AC-CPD26%, respectively, at the current density of 1 A/g over 2500 charge-discharge cycles. The tests were performed on three-electrode cells in 1 M H_2SO_4 solution.

Table 2.S1 Specific capacitance results reported in the literature for representative carbon-based materials in 3-electrode cells.

Name	Electrolyte	Potential Range	CV Measurement		GCD Measurement		Gas Sorption Measurement					Reference
			Scan rate	Specific Capacitance	Current Density	Specific Capacitance	BET Surface Area	Pore Volume V_{total} (V_{mic})	Pore Size d_{micro} (d_{meso})	CO_2 Adsorption	Hydrogen adsorption	
			mV/s	*F/g*	*A/g*	*F/g*	*m^2/g*	*cm^3/g*	*nm*	*mmol/g (cm^3/g)*	*wt%*	
Carbon Microspheres												
USP-C2	1M H_2SO_4	0 to 0.9 V (Ag/AgCl)	5	360 ± 11	--	--	698	--	0.82	--	--	S1
Activated Carbon												
PIR-4	6M KOH	-0.9 to 0 V (Ag/AgCl)	5	258	--	--	2350	0.88(0.44)	(2.25)	--	--	S2
AKN	1M H_2SO_4	0 to 0.75 V (Ag/AgCl)	0.5	358	0.125(1)	355(329)	2062	1.99(0.95)	1.4	(0.37)	--	S3
AK	1M H_2SO_4	0 to 0.75 V (Ag/AgCl)	0.5	321	0.125(1)	325(291)	2132	2.18(0.96)	1.4	(0.44)	--	S3
N22AC	1M H_2SO_4	0 to 1 V (Ag/AgCl)	10	426	--	--	2204	1.17(0.69)	(2.12)	--	--	S4
RAC	1M H_2SO_4	0 to 1 V (Ag/AgCl)	10	241	--	--	1913	0.86(0.51)	1.79	--	--	S4
	0.5M						~2000	~1.1(~0.95)	--	--	--	
CobK3	H_2SO_4	-0.1 to 0.9 V (Ag/AgCl)	25	127	--	--						S5
CNSs-6	6M NaOH	-0.8 to 0.2 V (Hg/HgO)	5	328	--	--	~1700	~0.86	2.00	--	--	S6
KOH-500	1M $NaNO_3$	−1.0 to 0.3 V (MSE).	5	226	--	--	--	1.375	--	--	--	S7
Carbide-derived Carbon												
Nano-CDC	1M H_2SO_4	0.4 to 0.9 V (Ag/AgCl)	--	--	0.0025 mA	132	952	0.90	0.85	--	--	S8
CCDC–KOH	6M KOH	-1 to 0 V (Hg/HgO)	1	280.1	--	--	1100	1.74(0.17)	(8.83)	--	--	S9
ACA-K2CO3	6M KOH	-1 to 0 V (Ag/AgCl)	--	--	1	152	1166	1.71	--	--	--	S10
PCNFW	6M KOH	-1 to 0 V (Hg/HgO)	5	171	--	--	416	0.19(0.18)	--	--	--	S11
N-CNFs-900	6M KOH	-1 to 0 V (Hg/HgO)	--	--	1	202	563	0.51	(3.64)	--	--	S12
CNT in Activated Carbon												
tube-in-AC	6M KOH	0 to 1 V (SCE)	1	378	--	--	1626	~1 – 2	--	--	--	S13
CO2-Derived Boron Doped Porous Carbon												
K-BPC	1M Na_2SO_4	-0.4 to 0.6 (Ag/AgCl)	20	139	--	--	--	--	--	--	--	S14
Graphene												
NGS	6M KOH	-1.1 to -0.1 V (SCE)	--	--	0.2	326	593	0.092	3	--	--	S15
Graphene in Activated Carbon												
GSNCs-1%	1M H_2SO_4	-0.2 to 0.8 V (Ag/AgCl)	--	--	0.3	324.6	1256		(2-50)	--	--	S16
RG3	2M H_2SO_4	-0.2 to 0.8 V (Ag/AgCl)	--	--	1	316	1652	0.94(0.39)	(2.28)	--	--	S17

RG3	6M KOH	-0.2 to 0.8 V (Ag/AgCl)	--	--	1	397	1652	0.94(0.39)	(2.28)	--	--	S17
P-F-GO-E	1M H_2SO_4	0 to 1 (Ag/AgCl)	--	--	1	327	181.6	0.74	(<5)	--	--	S18
Hiearchically Porous Carbon												
THPC	6M KOH	-1 to 0 (Hg/HgO)	--	--	0.5	318.2	2870	2.19	(2.73)	--	--	S19
Mesoporous Carbon by Soft-templating Approach												
COU-2	1M H_2SO_4	-0.2 to 0.8 V (Ag/Ag/Cl)	2	184	--	--	694	0.66(0.16)	(5.5)	--	--	S20
K-COU-2	1M H_2SO_4	-0.2 to 0.8 V (Ag/AgCl)	2(20)	244(187)	--	--	1685	1.25(0.47)	(5.5)	--	--	S20
AMC-6	0.1M NaCl	-0.4 to 0.6 V (Ag/AgCl)	1(10)	188(32)	--	--	1940	1.57(0.62)	(10)	--	--	S21
BP-800	1M H_2SO_4	-0.6 to 0.4 (Hg/HgO)	20	192	--	--	1578	1.092	<2	--	--	S22
BP-800	6M KOH	-1.2 to 0 V (Hg/HgO)	20	237	--	--	1578	1.092	<2	--	--	S22
MOF-derived Carbon												
NPC-800	0.5M H_2SO_4	0 to 0.8 V (Ag/Ag/Cl)	20	238	--	--	943	0.84	0.8(2-4)	--	--	S23
CZIF69a	0.5M H_2SO_4	-0.241 to 0.759	20	156	--	--	2264	--	<1.3	4.76	2.16	S24
C-S700	6M KOH	-1 to 0 V (Ag/AgCl)	2(20)	182(163)	--	--	817	0.85	0.8(2.7-10.6)	--	--	S25
Z-900	0.5M H_2SO_4	-0.2 to 1 V (Ag/AgCl)	5	214	--	--	1075	0.57(0.38)	(10.2)	--	--	S26
Z-900	0.5M H_2SO_4	-0.2 to 1 V (Ag/Ag/Cl)	5(20)	214(158)	--	--	1075	0.57(0.38)	(10.2)	--	--	S26
Carbon-700	6M KOH	-1 to 0 V (SCE)	10	218	--	--	672	0.38(0.34)	(2.3)	--	--	S27
MAC-A	6M KOH	-1 to 0 V (Ag/AgCl)	2	271	--	--	2222	1.14(1.01)	0.68	--	--	S28
MC-A	6M KOH	-1 to 0 V (Ag/AgCl)	2	208	--	--	1673	1.33(0.68)	0.9	--	--	S28
MPC-A	6M KOH	-1 to 0 V (Ag/AgCl)	2	196	--	--	1271	1.92(0.59)	0.9	--	--	S28
OMC-derived Carbon												
KF1– 90	6M KOH	-0.8 to 0 V (Hg/HgO)	--	--	0.5	200	1410	0.73(0.38)	1.5-4	--	--	S29
KNOMC-850	2M KOH	-1 to 0 V (SCE)	--	--	1	320	693	0.75(0.69)	(3.27)	--	--	S30
Surface Treated Carbon Black												
BP2	1M H_2SO_4	-0.4 to 0.75 V (Ag/AgCl)	2	250	--	--	270	--	1-2, 2-4	--	--	S31
Templated Porous Carbon by Hard and Soft Templating												
MHCS	2M H_2SO_4	0 to 1 V (Ag/AgCl)	--	--	0.25	404	935	2.14(0.45)	(6.67)	--	--	S32
Templated Porous Carbon by Nanocasting												
carbon hollow spheres	6M KOH	-1 to 0 V (Hg/HgO)	--	--	1(0.5)	266(269)	658	1.07	<1, 1-2, (>50)	--	--	S33
MPM-2	6M KOH	0 to -0.9 V (Hg/HgO)	--	--	0.1	224	349	0.339(0.051)	(3.88)	--	--	S34
ARP-CTs-30	6M KOH	-1 to 0 V (Hg/HgO)	50	230	--	--	2415.68	1.55	--	--	--	S35
BMC-I	1M H_2SO_4	0 to 0.8 V (Hg/HgO)	2	112	--	--	660	0.54	(4.9)	--	--	S36
BMC-II	1M H_2SO_4	0 to 0.8 V (Hg/HgO)	2	99	--	--	470	0.49	(6.8)	--	--	S36

Table 2.S2 Specific capacitance results reported in the literature for representative carbon-based materials in 2-electrode cells.

Name	Electrolyte	Potential Range	CV Measurement		GCD Measurement		Gas Sorption Measurement					Reference
			Scan rate *mV/s*	Specific Capacitance *F/g*	Current Density *A/g*	Specific Capacitance *F/g*	BET Surface Area m^2/g	Pore Volume V_{total} (V_{mic}) cm^3/g	Pore Size micropore (mesopore) *nm*	CO_2 Adsorption *mmol/g(cm^3/g)*	Hydrogen adsorption *wt%*	
Activated Carbon												
PAN-A	1M H_2SO_4	0 to 0.8 V	1(5)	201(176)	0.1(0.5)	176(157)	807	--	--	--	--	S37
aMP	2M H_2SO_4	-1 to 1 V	--	--	0.125	295	3160	1.58	0.6-2, 2-4	--	--	S38
KOH-A	1M H_2SO_4	0 to 1 V	--	--	0.1	176±9	2570	3	--	--	--	S39
KOH-A	6M KOH	0 to 1 V	--	--	0.1	173±7	2570	3	--	--	--	S39
H-CMN	1M H_2SO_4	0 to 1 V	--	--	0.1	264	2557.3	--	<4	--	--	S40
SCC-750-1	1M H_2SO_4	0 to 1 V	--	--	0.25	300	1452	0.81(0.48)	<2	(0.27)	--	S41
CGC	1M H_2SO_4	0 to 1 V	--	--	0.05	368	1019	0.48(0.21)	<1, (2-4)	(~0.275)	--	S42
AK3P-0.30	30wt% KOH	0 to 0.8 V	--	--	0.12	218	1759	0.93(0.61)	(3.5-4.5)	--	--	S43
NC-700-3	30wt% KOH	0 to 1 V	--	--	0.125	311	2509	1.34(1.12)	(2.1)	--	--	S44
Carbide-derived Carbon												
TiC-CDC	1M H_2SO_4	-0.5 to 0.5 V	5	190	--	--	600-2000	--	0.7-1.85	--	--	S45
Carbon Aerogel												
ACA	6M KOH	-1 to 0 V	--	--	1	136	1447	--	(3.4)	--	--	S46
Carbon Fiber-based Material												
ACF4	6M KOH	0 to 1 V	1	371	--	--	3291	2.162(0.721)	~1.5, (~3)	--	--	S47
Activated Carbon Containing Graphene or CNT												
CNAGs/SMF-Ni-5	5M KOH	-1 to 0 V	1(5)	359(321)	--	--	155	0.138(0.05)	(3.6)	--	--	S48
hGO	6M KOH	0 to 1 V	10	110	--	--	--	--	--	--	--	S49

GAC	KOH	0 to 1.2 V	--	--	0.1	122	798	--	2	--	--	S50
Hiearchically Porous Carbon												
HPCs-3	6M KOH	0 to 1 V	1	272	--	--	689	0.61(0.19)	(3.84)	--	--	S51
MOF-derived Carbon												
C1000	1M H_2SO_4	-0.5 to 0.5 V	5	161	--	--	3405	2.58(1.54)	--	--	2.77	S52
C800	1M H_2SO_4	-0.5 to 0.5 V	5	188	--	--	2169	1.5(0.9)	--	--	2.23	S52
NPC	1M H_2SO_4	-0.5 to 0.5 V	5	204	--	--	2872	2.06	--	--	2.6	S53
NPC650	1M H_2SO_4	-0.5 to 0.5 V	5	167	--	--	1521	1.48(0.06)	(3.9)	--	--	S54
Templated Porous Carbon by Nanocasting												
OMC-M-6	30wt% KOH	-1 to -0.2 V	5	205.3	--	--	868.5	1.75(0.18)	(8.5)	--	--	S55
CNC700	1M H_2SO_4	0 to 1 V	10	251	--	--	1854	--	(5-8)	--	--	S56
HPC-242	1M H_2SO_4	-0.2 to 0.8 V	--	--	0.1	165	940	1.2(0.33)	242*	--	--	S57
Y-Ac	1M H_2SO_4	0 to 1 V	2	240	--	--	1814	1.03(0.508)	<0.7, 1.7	--	--	S58
Y-AN	1M H_2SO_4	0 to 1 V	2	340	--	--	1680	0.86(0.51)	<0.7, 1.7	--	--	S58

***macroporous**

2.7 References

S1. H. Kim, M. E. Fortunato, H. Xu, J. H. Bang and K. S. Suslick, *J. Phys. Chem. C*, 2011, **115**, 20481–20486.

S2. S.-J. Han, Y.-H. Kim, K.-S. Kim and S.-J. Park, *Curr. Appl Phys.*, 2012, **12**, 1039–1044.

S3. A. Elmouwahidi, Z. Zapata-Benabithe, F. Carrasco-Marín and C. Moreno-Castilla, *Bioresource Technol.*, 2012, **111**, 185–190.

S4. J. W. Lim, E. Jeong, M. J. Jung, S. I. Lee and Y.-S. Lee, *J. Ind. Eng. Chem.,* 2012, **18**, 116–122.

S5. R.-L. Tseng, S.-K. Tseng, F.-C. Wu, C.-C. Hu and C.-C. Wang, *J. Chin. Inst. Chem. Eng*., 2008, **39**, 37–47.

S6. D. Yuan, J. Chen, J. Zeng and S. Tan, *Electrochem. Commun.*, 2008, **10**, 1067–1070.

S7. S.-E. Chun, J. F. Whitacre, *Electrochim. Acta*, 2012, **60**, 392–400.

S8. C.R. Pérez, S.-H. Yeon, J. Ségalini, V. Presser, P.-L. Taberna, P. Simon and Y. Gogotsi, *Adv. Funct. Mater.*, 2013, **23**, 1081–1089.

S9. H. Wu, X. Wang, X. Wang, X. Zhang, L. Jiang, B. Hu and Y. Wang, *J. Solid State Electrochem.,* 2012, **16**, 2941–2947.

S10. Y. J. Lee, H. W. Park, U. G. Hong and I. K. Song, *Curr. Appl. Phys.*, 2012, **12**, 1074–1080.

S11. C. Ma, Y. Song, J. Shi, D. Zhang, M. Zhong, Q. Guo and L. Liu, *Mater. Lett.*, 2012, **76**, 211–214.

S12. L-F. Chen, X-D. Zhang, H-W. Liang, M. Kong, Q-F. Guan, P. Chen, Z-Y. Wu and S-H. Yu, *ACS NANO*, 2012, **6(8)**, 7092–7102.

S13. C. Zheng, W. Qian and F. Wei, *Mater. Sci. Eng., B*, 2012, **177**, 1138–1143.

S14. J. Zhang and J.W. Lee, *ACS Sustainable Chem. Eng.*, 2014, **2(4)**, 735–740.

S15. L. Sun, L. Wang, C. Tian, T. Tan, Y. Xie, K. Shi, M. Li and H. Fu, *RSC Adv.,* 2012, **2**, 4498–4506.

S16. M-X. Wang, Q. Liu, H-F. Sun, E. A. Stach, H. Zhang, L. Stanciu and J. Xie, *Carbon*, 2012, **50**, 3845–3853.

S17. K. Zhang, B. T. Ang, L. L. Zhang, X. S. Zhao and J. Wu, *J. Mater. Chem.*, 2011, **21**, 2663–2670.

S18. H. Sun, L. Cao and L. Lu, *Energy Environ. Sci.*, 2012, **5**, 6206–6213.

S19. L. Qie, W. Chen, H. Xu, X. Xiong, Y. Jiang, F. Zou, X. Hu, Y. Xin, Z. Zhang and Y. Huang, *Energy Environ. Sci.*, 2013, **6**, 2497–2504.

S20. J. Jin, S. Tanaka, Y. Egashira and N. Nishiyama, *Carbon*, 2012, **48**, 1985–1989.

S21. X. Wang, J.S. Lee, C. Tsouris, D. W. DePaoli and S. Dai, *J. Mater. Chem.*, 2010, **20**, 4602–4608.

S22. H. Zhu, J. Yin, X. Wang, H. Wang and X. Yang, *Adv. Funct. Mater.*, 2013, **23**, 1305–1312.

S23. N. L. Torad, R. R. Salunkhe, Y. Li, H. Hamoudi, M. Imura,Y. Sakka, C.-C. Hu and Y. Yamauchi, *Chem. Eur. J.*, 2014, **20**, 7895–7900.

S24. Q. Wang, W. Xia, W. Guo, L. An, D. Xia and R. Zou, *Chem. Asian J.*, 2013, **8**, 1879–1885.

S25. P. Su, L. Jiang, J. Zhao, J. Yan, C. Li and Q. Yang, *Chem. Commun.*, 2012, **48**, 8769–8771.

S26. W. Chaikittisilp, M. Hu, H. Wang, H-S. Huang, T. Fujita, K. C.-W. Wu, L-C. Chen, Y. Yamauchi and K. Ariga, *Chem. Commun.*, 2012, **48**, 7259–7261.

S27. Z. J. Zhang, P. Cui, C. Chen, X. Y. Chen, and J. W. Liu, *J. Solid State Electrochem.,* 2014, **18**, 59–67.

S28. J. Hu, H. Wang, Q. Gao and H. Guo, *Carbon*, 2010, **48**, 3599–3606.

S29. Y. Lv, F. Zhang, Y. Dou, Y. Zhai, J. Wang, H. Liu, Y. Xia, B. Tu and D. Zhao, *J. Mater. Chem.*, 2012, **22**, 93–99.

S30. D. Zhang, L. Zheng, Y. Ma, L. Lei, Q. Li, Y. Li, H. Luo, H. Feng and Y. Hao, *ACS Appl. Mater. Interfaces* 2014, **6**, 2657−2665.

S31. G. Pognon, C. Cougnon, D. Mayilukila and D. Beĺanger, *ACS Appl. Mater. Interfaces*, 2012, **4**, 3788−3796.

S32. Y. Wang, S. Tao and Y. An, *Microporous Mesoporous Mater.*, 2012, **163**, 249–258.

S33. Y. Han, X. Dong, C. Zhang and S. Liu, *J. Power Sources*, 2012, **211**, 92–96.

S34. C. Ma, J. Shi, Y. Song, D. Zhang, X. Zhai, M. Zhong, Q. Guo and L. Liu, *Int. J. Electrochem. Sci.*, 2012, **7**, 7587–7599.

S35. Y. Chen, B. Wang, S. Dong, Y. Wang and Y. Liu, *Electrochim. Acta*, 2012, **80**, 34–40.

S36. D-W. Wang, F. Li, Z.-G. Chen, G. Q. Lu and H-M. Cheng, *Chem. Mater.,* 2008**,** ***20,*** 7195–7200.

S37. G. Lota, B. Grzyb, H. Machnikowska , J. Machnikowski and E. Frackowiak, *Chem. Phys. Lett.*, 2005, **404**, 53–58.

S38. C-W. Huang, C-T. Hsieh, P-L. Kuo and H. Teng, *J. Mater. Chem.*, 2012, **22**, 7314–7322.

S39. M. Zhong, E. K. Kim, J. P. McGann, S-E. Chun, J. F. Whitacre, M. Jaroniec, K. Matyjaszewski and T. Kowalewski, *J. Am. Chem. Soc.* 2012, **134**, 14846−14857.

S40. Y. S. Yun, S. Y. Cho, J. Shim, B. H. Kim, S-J. Chang, S. J. Baek, Y. S. Huh, Y. Tak, Y. W. Park, S. Park and H.-J. Jin, *Adv. Mater.*, 2013, **25**, 1993–1998.

S41. T.E. Rufford, D. Hulicova-Jurcakova, K. Khosla, Z. Zhu and G.Q. Lu, *J. Power Sources*, 2010, **195**, 912–918.

S42. T.E. Rufford, D. Hulicova-Jurcakova, Z. Zhu and G.Q. Lu, *Electrochem Commun.,* 2008, **10**, 1594–1597.

S43. S. Guo, F. Wang, H. Chen, H. Ren, R. Wang and X. Pan, *J. Solid State Electrochem.*, 2012, **16**, 3355–3362.

S44. X. Li, W. Xinga, S. Zhuoa, J. Zhoua, F. Li, S-Z Qiao and G-Q. Luc, *Bioresource Technol.,* 2011, **102**, 1118–1123.

S45. J. Chmiola, G. Yushin, R. Dash and Y. Gogotsi, *J. Power Sources*, 2006, **158**, 765–772.

S46. Y.J. Lee, H.W. Park, S. Park and I.K. Song, *Curr. Appl Phys.*, 2012, **12**, 233–237.

S47. B. Xu , F. Wu , R. Chen , G. Cao , S. Chen , Z. Zhou and Y. Yang, *Electrochem. Comm.*, 2008, **10**, 795–797.

S48. Y. Fang, F. Jiang, H. Liu, X. Wu and Yong Lu, *RSC Adv.*, 2012, **2**, 6562–6569.

S49. S. Zhang and N. Pan, *J. Mater. Chem. A*, 2013, **1**, 7957.

S50. Y. Chen, X. Zhang, H. Zhang, X. Sun, D. Zhang and Y. Ma, *RSC Adv.,* 2012, **2**, 7747–7753.

S51. X.Zhang, X. Wang, J. Su, X. Wang, L. Jiang, H. Wu and C. Wu, *J. Power Sources*, 2012, **199**, 402–408.

S52. H-L. Jiang, B. Liu, Y-Q. Lan, K. Kuratani, T. Akita, H. Shioyama, F. Zong and Q. Xu, *J. Am. Chem. Soc.,* 2011, **133**, 11854–11857.

S53. B. Liu, H. Shioyama, T. Akita and Q. Xu, *J. Am. Chem. Soc.* 2008, **130**, 5390–

5391.

S54. B. Liu, H. Shioyama, H. Jiang, X. Zhang and Q. Xu, *Carbon*, 2010, **48** ,456–463.

S55. H. Lu, W. Dai, M. Zheng, N. Li, G. Ji and J. Cao, *J. Power Sources*, 2012, **209**, 243–250.

S56. K. Xie, X. Qin, X. Wang, Y. Wang, H. Tao, Q. Wu, L. Yang and Z. Hu, *Adv. Mater.*, 2012, **24**, 347–352.

S57. Q. Cheng, Y. Xia, Vl. Pavlinek, Y. Yan, C. Li and P. Saha, *J. Mater. Sci.*, 2012, **47**, 6444–6450.

S58. C.O. Ania, V. Khomenko, E. Raymundo-Piñero, J.B. Parra and F. Béguin, *Adv. Funct. Mater.*, 2007, **17**, 1828–1836.

Chapter 3: Highly Graphitic Carbon Containing Uniformly Dispersed Co_xO_y and Co Nanoparticles for Hybrid EDLC/Pseudocapacitor Applications

Abstract

In this chapter, the use of a highly cross-linked acetylenic co-polymer (CPD76%) with a high content of pendent alkyne groups, as a reactive polymer precursor for production of a carbon/Co_xO_y/Co nanocomposite is demonstrated. The high alkyne content of CPD76% facilitates the production of highly dispersed $Co_2(CO)_6$/alkyne moieties within CPD76% when reacted with $Co_2(CO)_8$, which can be subsequently carbonized and oxidized to produce Co/Co_xO_y nanoparticles within a carbon supported matrix (Co_xO_y@C-CPD76%). Not only does this route provide a facile approach to evenly distributing Co/Co_xO_y within the carbon, but also produces a highly graphitized carbon support, improving electrochemical properties. Electrochemical measurements show that this composite material is able to exhibit both electrochemical double layer (EDLC) and pseudocapacitive (PS) behaviour in different potential ranges as a result of the highly graphitized activated carbon and the electrochemically active Co/Co_xO_y nanoparticles, respectively. Measurements performed in 2 M KOH solutions within a wide potential window (-1 to 0.4 V vs. SCE) show high specific capacitance (310 F g^{-1}), energy density (21 W h kg^{-1}) and power density (2017 W kg^{-1}).

3.1 Introduction

With the growing concerns about global climate change, fossil fuel depletion, and environmental pollution, green and sustainable energy technologies have become increasingly popular topic amongst researchers. In particular, there is a growing interest in the development of electrochemical capacitors (EC) with high specific capacitances, energy densities and power densities. Depending on their charge-discharge mechanisms, ECs are classified as either electrochemical double layer capacitors (EDLC) or pseudocapacitors (PS).[1-17] EDLCs are typically made from carbonaceous materials like activated carbons (AC), graphenes, carbon nanotubes (CNT), carbon onions, carbon fibers, fullerenes, carbide derived carbons, *etc*.[1-9,18] Energy storage is accomplished through purely physical adsorption of ions of an electrolyte on the surface of the carbonaceous material, and have relatively high specific capacitances and energy densities compared with conventional capacitors. The performance of EDLCs has been shown to be highly dependent on the surface area, pore volume, pore size distributions, textural properties, *etc*., of the carbonaceous materials. In particular, controlling the size and proportion of micropores ($d < 2$ nm) and mesopores ($2 \leq d \leq 50$ nm) is believed to be critical to optimum performance in EDLCs.[1-9]

PS materials are composed of transition metal oxides/hydroxides or conducting polymers, and rely primarily on faradaic reactions to store charge. Although PSs provide much higher energy densities and specific capacitances relative to EDLCs, they suffer from lower power densities due to slow reaction rates, low conductivities, and diffusion problems.[1,2,10-18] In addition, irreversible structural changes resulting from physiochemical

changes during charging and discharging result in much lower cycling abilities of the PS's compared with EDLCs.[1,19] Currently, the most common PS materials being researched include oxides and hydroxides of Ni, Co, Mn, Ru, as well as composites of two or more metal oxides.[1,2,10-18] A material that could combine the high power densities of EDCLs with the high energy densities and capacitances of PSs is desirable.

In Chapter 2, we explored the use of a new family of cross-linked polymers of 1,3-diethynylbenzene (DEB) and phenylacetylene (PA) with varying crosslinking densities for their use as EDLCs. DEB feed content higher than that of CPD71% suffered form an excess of cross-linking density. Excess cross-linking resulted in carbons with high microporosity, but low micropore volume and narrow pore size distribution, and correspondingly provided less than ideal EDLC performance. Polymers with DEB content ranging between 71 mol% and 39 mol% produced carbons with broader pore size distribution, while maintaining high microporosity and optimal EDLC performance. Therefore, the polymer with 71 mol% DEB content (76% by weight) was chosen a candidate for production of PSC materials in this chapter.

Amongst the transition metals studied for use in PSs, much attention has been given to oxides and hydroxides of cobalt (*i.e.*, Co_3O_4, $Co(OH)_2$, and CoO) due to their relative environmentally friendliness, low cost, and high theoretical specific capacitances (3560 F g^{-1}, 3460 F g^{-1}, and 4292 F g^{-1} for Co_3O_4, $Co(OH)_2$, and CoO respectively).[19-21] Achieving specific capacitances approaching those of the theoretical values has been a challenge, and several strategies have been developed to synthesize cobalt-based

pseudocapacitors with optimized properties. The semiconducting nature and low conductivity of transition metal oxides/hydroxides provide a challenge to improve power densities in pseudocapacitors.[1,10,18,22,23] A common approach to improving conductivity is to disperse graphene oxide (GO), CNTs, or ACs into a cobalt salt solution, and then subject the solution to hydrothermal conditions. The resulting metal hydroxide/carbonaceous composites can then be used as is, or annealed at high temperatures (*ca*. 250 ºC) to form oxide/carbon PS materials.[23,24] Alternatively, electrodeposition of transitional metal oxides onto Ni foam or graphene substrates has been demonstrated to greatly improve PS power densities.[18,25-27] Structural and chemical differences such as grain size, morphology and crystal structure have also been found to profoundly affect the electrochemical performance of pseudocapacitor materials.[1,10,18,28] Flower–like structures, nanocages, nanoparticles, cones, scrolls, needles etc. of $Co(OH)_2$, CoO and Co_3O_4, have been synthesized by hydrothermal, electrochemical deposition, and precipitation synthesis routes in an effort to increase surface areas and pore volumes, and improve the electrochemical performances.[1,18,24,29-32]

Careful selection of cobalt salt precursors for synthesizing $Co(OH)_2$, CoO and Co_3O_4 can also have profound effects on their performance. For example, in the case of production of $Co(OH)_2$, different cobalt salts ($CoSO_4$, $CoCl_2$, $Co(NO_3)_2$, $Co(CH_3COO)_2$, *etc*.) can produce α-$Co(OH)_2$ sheets with differing intercalated anions resulting in significantly differing performances and morphologies.[23,32] However, the use of cobalt salt solutions for the synthesis of $Co(OH)_2$/carbon composites provides little control of its distribution within carbon supports.

An alternative method of distributing cobalt evenly within a supporting material is possible, provided that certain requirements are met. Previous research has shown that materials containing alkyne groups are able to coordinate with metallic carbonyls, effectively distributing the metal to all areas with alkyne bonds present. Equation 3.1 below demonstrates the complexation reaction of $Co_2(CO)_8$ with an alkyne group.

$$Co_2(CO)_8 + \text{Alkyne} \rightarrow Co_2(CO)_6/\text{alkyne} + 2CO \quad (3.1)$$

The formation of $Co_2(CO)_6$/alkyne moieties has been widely studied for its use in Pauson–Khand reactions, and can form well distributed cobalt nanoparticles via the decomposition of $Co_2(CO)_6$/alkyne coordination complex moieties at elevated temperatures, according to the following equation.[2,10,33-39]

$$Co_2(CO)_6 \rightarrow 2Co + 6CO \quad (3.2)$$

At particularly high temperatures (>700 ºC) cobalt metal nanoparticles have been shown to catalyze the formation of CNTs, graphene, carbon fibers, nanospheres, and amorphous AC carbon supports from different alkyne containing compounds by carefully controlling temperature ramping rates, final holing temperatures, and holding times.[2,33,35,36,38,39] Although this route is an effective method of producing cobalt containing carbonaceous materials, it has been rarely explored for use in supercapacitors.[34,35]

In this chapter, we explore their use as a PS supporting material, by the carbonization and subsequent oxidation of a $Co_2(CO)_6$/poly(phenylacetylene-co-diethynylbenzene) moiety. We demonstrate the preparation of well-dispersed nanoparticles of Co_xO_y in graphitized AC, which has excellent EDCL and PS capacitor performances (as high as 310 F g^{-1}), high conductivity, power density (2017 W kg^{-1}), energy density (21 W h kg^{-1}), and a large window of stability (1.4 V in 2 M KOH solution).

3.2 Experimental

3.2.1 Materials

DEB (97%, Aldrich), PA (98%, Aldrich), palladium acetate ($Pd(OAc)_2$, min. 98%, Strem Chemicals), α,α'-bis(di-*t*-butylphosphino)-*o*-xylene (97%, Strem Chemicals), methanesulfonic acid (99.5%, Aldrich), methanol (ACS reagent, Fisher Scientific), Hydrochloric Acid (ACS reagent, Fisher Scientific), Nafion solution (5 wt.% in lower aliphatic alcohols, Aldrich), platinum wire (0.5 mm in diameter, 99.95%, Strem Chemicals), conducting carbon (acetylene black 100%, Soltex), potassium hydroxide (flakes, reagent grade, 90%, Aldrich), and dicobalt octacarbonyl (moistened with 10% hexane, Sigma-Aldrich) were all used as received without any additional purification. Deionized water was obtained from a Barnstead/Synbron Nanopure II water purification system. Nickel foam (95% purity; 95% porosity, Goodfellow Corporation) was annealed by heating to 1000 °C for 2 hr. under vacuum, and dichloromethane was purified using a solvent purification system (Innovative Technology).

3.2.2 Synthesis of CPD76% and CPD76%/$Co_2(CO)_6$ Polymer Precursors

CPD76% was synthesized through a catalytic polymerization with the use of an *in situ* generated diphosphine-ligated cationic Pd(II) catalyst system ($Pd(OAc)_2$/α,α'-bis(di-*t*-butylphosphino)-*o*-xylene/methanesulfonic acid), where 76% refers to the weight percentage DEB in the DEB/PA monomer feed (76 wt% or ~71 mol%). Synthesis of co-polymers similar to CPD76% can be found in detail from Chapter 2. Briefly, DEB (1.52 g), PA (0.49 g), and 20 mL of methanol were injected into a Schlenk flask under nitrogen protection and constant magnetic stirring. In a separate container, $Pd(OAc)_2$ (0.0177 g) and diphosphine ligand (0.0941 g) were dissolved in a total of 17 mL of methanol with the aid of sonication to form the catalyst solution. The catalyst solution was then added to the Schlenk flask, and 2 drops of methanesulfonic acid were added to initiate the polymerization. The polymerization was left to react for 18 hours, and was terminated by pouring the polymer dispersion into acidified methanol (*ca*. 2 %). The polymer was washed with anhydrous dichloromethane (DCM) five times, and dried under vacuum for 2 days at room temperature.

Once sufficiently dried, CPD76% (0.8332 g) was dispersed with 40 mL of DCM in a Schlenk flask equipped with a gas bubbler, and stirred for 30 min under nitrogen protection. In a separate container, $Co_2(CO)_8$ (0.8561 g) dissolved in 20 mL of DCM was added to the Schlenk flask and allowed to react for 3 hours. $Co_2(CO)_8$ is highly sensitive to decomposition into cobalt metal when exposed to high temperatures, or if left at room temperature for extended periods of time, so the reaction time between CPD76% and $Co_2(CO)_8$ was limited to 3 hours. This reaction time was chosen because the half-life of

$Co_2(CO)_8$ during the alkyne coordination reaction is about 300 seconds.[37,39] The resulting dark brown dispersion was filtered through a porous frit, and washed 5 times with DCM under N_2 protection. The CPD76%/$Co_2(CO)_6$ product was stored in a freezer for later use.

3.2.3 Synthesis of Co_xO_y@C-CPD76%

The cobalt containing carbon synthesized for this research was prepared in three steps. First, CPD76%/$Co_2(CO)_6$ was heated to 100 ºC in a tube furnace and held for 20 min under a flow of nitrogen. The sample was then heated to 800 ºC for 1 hour at a rate of 10 ºC min^{-1}, and then allowed to cool down naturally to 150 ºC. Once cooled, the gas was switched to dry compressed air, and the temperature was raised from 150 ºC to 200 ºC for 5 hours at a rate of 2 ºC min^{-1}. The carbon produced was labeled Co_xO_y@C-CPD76% and was allowed to cool down naturally to room temperature after oxidation. For comparison purposes, pure CPD76% subjected to identical carbonizing conditions are labeled XC-CPD76% and C-CPD76%, with the latter being obtained by excluding the oxidation step.

3.2.4 Annealed Ni Foam Current Collectors

Complete details regarding the annealing process can be found elsewhere.[25] Small pieces of nickel foam (2 cm x 1 cm) cut from a larger sheet were washed with acetone, and then with deionized water with the aid of sonication for 10 minutes. The Ni foam pieces were treated with 4 M HCl under sonication for 15 minutes, and then washed with deionized water and acetone with the aid of sonication for 10 minutes. The samples were allowed to dry in an oven at *ca*. 130 ºC for 10 minutes before the annealing process. The Ni foam pieces were then placed in a tube furnace, and subjected to a vacuum with an oil pump for 30 minutes. The temperature was ramped to 1000 ºC, held for 2 hours, and

allowed to cool back to room temperature naturally. Once cooled, the Ni foam electrodes were transferred into a N_2 atmosphere glove box for storage prior to use.

3.2.5 Characterizations

Thermogravimetric analysis (TGA) was conducted with a Q50 Series TGA from TA Instruments. Measurements were performed with N_2 and dry air with a continuous flow of 60 mL min^{-1} through the sample compartment, and 40 mL min^{-1} N_2 through the balance compartment. The samples (*ca*. 5-10 mg) were heated to 100 ºC at 10 ºC min^{-1} and held for 20 minutes, then raised to 800 ºC at 10 ºC min^{-1} and held for 1 hour. The samples were allowed to cool naturally within the sample compartment to 150 ºC before switching the gas line to compressed air. Once airflow was initiated, the temperature was raised to 200 ºC at 2 ºC min^{-1} and held for 5 hours. Braunauer-Emmett-Teller (BET) specific surface area, pore volume, and pore size distribution were determined by N_2 sorption at 77 K using a Micromeritics ASAP 2020 physiosorption analyzer. The Horvath-Kawazoe (HK) and Barrett-Joyner-Halenda (BJH) models were used to calculate pore size distributions for the micropore ($d < 20$ nm) and mesopore ($2 \leq d \leq 50$ nm) regions, respectively. Prior to the N_2 sorption measurements, samples were degassed at 200 ºC for *ca*. 20 hours. An X'Pert Pro diffractometer with Co radiation source ($\lambda_{k\alpha}$=1.79 Å) was used at room temperature to generate XRD patterns for all samples. FTIR measurements were performed using a Thermo Scientific Nicolet 6700 Analytical FTIR spectrometer, between 400-4000 cm^{-1} under constant flow of nitrogen (*ca*. 20 mL min^{-1}). To prepare the samples for testing, about 100 mg of KBr, and 1 mg of the carbon sample were mixed and ground with a mortar and pedestal. The mixture was compressed with 7 tons of pressure into a small 1 cm^2 disk, and then placed into the FTIR sample holder. All

FTIR samples were purged with N_2 for at least 30 min before background and sample measurements. ICP-MS measurements were performed on a Varian 810. ICP-MS solutions were prepared by burning a small sample on quartz in air at 1000 °C for 2 hours, then placing the quartz and residual cobalt in a solution of aqua regia and ~10% hydrofluoric acid to dissolve all the cobalt into solution. The solution was then heated to 100 °C to remove all hydrofluoric acid, and re-dissolved in dilute (*ca*. 20%) aqua regia. TEM imaging was performed using a JEOL 2010F field emission electron microscope operated at 200 keV.

3.2.6 Electrochemical Measurements

Cyclic voltammetry (CV), galvanostatic charge discharge (GCD), and electrochemical impedance spectroscopy (EIS) measurements were performed in 2 M KOH, using a Metrohm Autolab PGSTAT100 potentiostat/galvanostat,. A coiled platinum wire and saturated calomel electrode served as the counter and reference electrodes, respectively. To prepare the working electrode, the active material (80 wt%), conducting carbon (10 wt%), and Nafion (10 wt%) were dispersed in a water-acetone (1:1 in volume) solution under sonication in a small vial. The dispersion was then evenly coated onto a 2 cm x 1 cm piece of Ni foam by drop casting with a micropipette, and dried at 130 ºC for 15 minutes. The electrode was folded in half, and compressed with 2 tons of pressure to produce a 1 cm^2 sandwich structured electrode of *ca*. 0.5 mm thickness. The mass loading of the active material on Ni foam current collector was kept constant at 10 mg cm^{-2} for all electrochemical tests. CV curves were obtained in the potential ranges of 0 to 0.4 V, -1 to 0 V and -1 to 0.4 V, at different scan rates (1, 5, 10,

25, 50 and 100 mV s^{-1}). Specific capacitances (C_{sp}, in F g^{-1}) were calculated using the following equation: [40]

$$C_{sp} = \frac{\frac{1}{2}\int idV}{mv\Delta V} \tag{2.1}$$

where i and V are the current and voltage respectively, $\int idV$ is the area within the CV curve, m is the mass of the active material on the current collector, v is the voltage sweep rate, and ΔV is the voltage range of the CV test. GCD measurements were performed in identical voltage ranges, with current densities of 0.1, 0.25 0.5, 1, 2, 3, 5and 10 A g^{-1}, with specific capacitances calculated as follows:[40]

$$C_{sp} = \frac{i}{mdV/dt} \tag{2.2}$$

where i is the discharge current, m is the mass of the active material, and dV/dt is the slope of the discharge curve after the initial ohmic drop, to the end of the discharge. Energy density (E, in W h kg^{-1}) and power density (P, in W kg^{-1}) were calculated as follows:[23]

$$E = \frac{1}{2} C_{sp} V^2 \cdot \frac{1}{4} \cdot \frac{1}{3.6} \tag{2.5}$$

$$P = \frac{E}{t} \tag{2.6}$$

where C_{sp} is the specific capacitance obtained through GCD measurements, V is the voltage range used, t is the discharge time after the initial ohmic drop in hour. EIS measurements were conducted at potentials of 0 V with an AC perturbation of 10 mV at frequencies ranging from 10 kHz to 0.01 Hz.

3.3 Results and Discussion

3.3.1 Polymer Synthesis, Cobalt Functionalization, Carbonization, and Textural Properties of Functionalized Carbons

Analysis of samples of CPD76%/$Co_2(CO)_6$ carbon precursor and Co_xO_y@C-CPD76% by ICP-MS determined cobalt concentrations of 17.17% and 22.79% by weight. Figure 3.1 shows the FTIR spectrum of the pristine CPD76% before and after the complexation reaction with $Co_2(CO)_8$. The presence of pendent alkyne groups is confirmed from the large $\nu_{C\equiv C\text{-}H}$ band centered at 3290 cm^{-1} and the $\nu_{C\equiv C}$ band at 2106 cm^{-1}.[41] After reacting with $Co_2(CO)_8$, three bands appear at 2021, 2054, and 2095 cm^{-1} (overlapping the $\nu_{C\equiv C}$ band at 2106 cm^{-1}) along with a reduction in the intensity of the $\nu_{C\equiv CH}$ band at 3290 cm^{-1}. The three new bands correspond to the ν_{CO} stretching vibrations of carbonyl groups in the acetylenic dicobalt hexacarbonyl.[34,38,39,42] The carbonyl bands of complexation reaction product are very similar to those of pure $Co_2(CO)_8$, with the exception of the missing bridged carbonyl stretching vibration peaks at about 1860 cm^{-1}.[33] This indicates that the pendent alkyne bonds within CPD76% successfully replaced the two bridging carbonyl groups from $Co_2(CO)_8$, producing the CPD76%/$Co_2(CO)_6$ moiety.[42] After carbonizing CPD76%/$Co_2(CO)_6$ at 800 ºC for 1 hour, the remaining pendent alkyne peaks and the terminal carbonyl groups from the dicobalt hexacarbonyl disappear, indicating a complete reduction of the $Co_2(CO)_6$ into cobalt metal, and carbonization of

the CPD76%. The cobalt-containing carbon, prior to oxidation, was named Co@C-CPD76%, and its FTIR spectrum can be seen in Figure 3.1. Oxidation of the Co@C-CPD76% to Co_xO_y@C-CPD76% produces two peaks centered at 573 cm^{-1} and 667 cm^{-1} that can be attributed to the δ_{Co-O} band of Co^{2+} and Co^{3+} within Co_3O_4.[29,33]

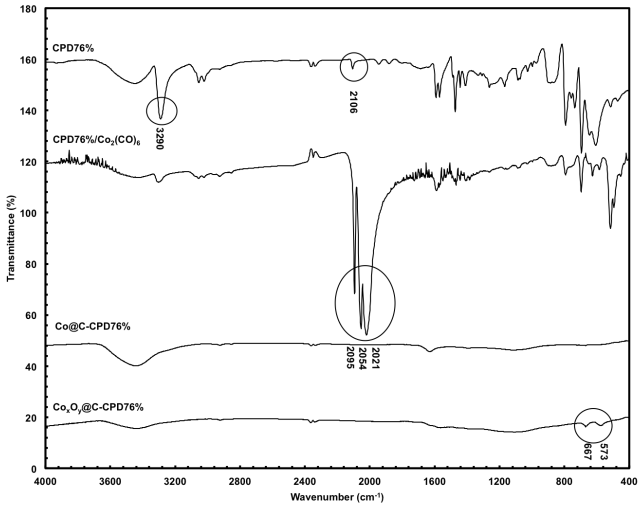

Figure 3.1 FTIR spectrum of CPD76%, CPD76%/Co2(CO)6 moiety, Co@C-CPD76%, and Co_xO_y@C-CPD76%.

TGA characterization was used to monitor the carbonization and oxidization of pristine CPD76% and CPD76%/$Co_2(CO)_6$ as shown in Figure 3.2. In the initial heating stage, a sharp weight loss from CPD76%/$Co_2(CO)_6$ can be seen in Figure 3.2(a) and (b) at 98 ºC, which is absent in CPD76%. This sudden weight loss is attributed to the release of carbon monoxide from CPD76%/$Co_2(CO)_6$ as described earlier, and confirmed through FTIR in Figure 3.1. The samples were then heated to 800 ºC and held for 1 hour to produce carbons Co@C-CPD76% and C-CPD76%, respectively. Major weight losses at 478 ºC and 568 ºC can be seen for CPD76%/$Co_2(CO)_6$ and CPD76%, respectively, in

Figure 3.2. The weight loss trend for CPD76% is similar for DEB-PA copolymers outlined in Chapter 2. Based on the data collected in Figure 3.2(b), the total carbon weight loss from CPD76% was shown to be significantly lower than CPD76%/$Co_2(CO)_6$ even when considering the weight loss caused by release of CO (*ca*. 24.5%) and constant weight of cobalt within the sample (17.17%, from ICP-MS). Considering this, the CPD76%/$Co_2(CO)_6$ contains about 58 wt% CPD76% polymer, which was converted to carbon contributing 28.5% of the total mass. Therefore, about 49% carbon was yielded from CPD76%/$Co_2(CO)_6$ compared to the 82% carbon yield from the pure CPD76%. Oxidation, when compressed air was turned on at 150°C, further increased the yield of both samples by *ca*. 1%, indicating the addition of oxygen groups and the oxidation of some of the Co metal species to Co_xO_y in the case of CPD76%/$Co_2(CO)_6$. Similar carbonization onsets and carbon yield changes pertaining to cobalt-containing acetylenic precursors have been described by others.[2,39]

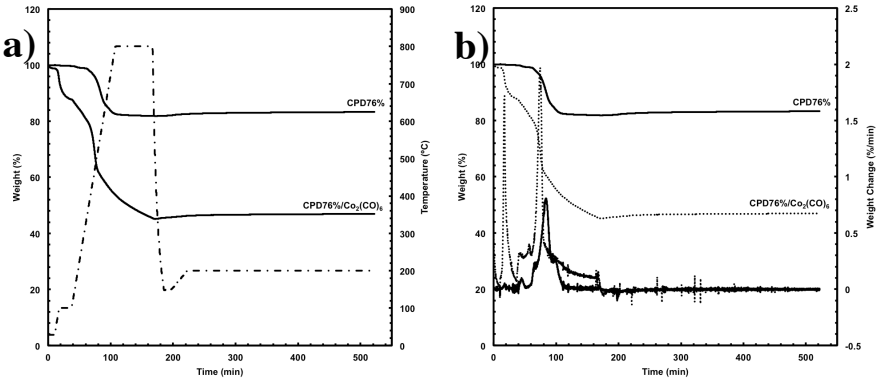

Figure 3.2 (a) TGA weight loss curves for CPD76% and CPD76%/$Co_2(CO)_6$, (b) Differential weight loss curves of CPD76% and CPD76%/$Co_2(CO)_6$.

XRD patterns shown in Figure 3.3 were used to further elucidate the effects of incorporating cobalt at various points of the synthesis procedure on the nature of the

corresponding product. All curves were normalized to the low angle carbon peak near 4.5º for a better representation of the relative intensity of the cobalt peaks within the carbons. CPD76% shows a XRD pattern similar to that of pure polyphenylacetylene, characterized by two peaks at *ca*. 4.5º and 22º, but with a notable difference in the relative intensities of the two peaks to each other.[43] The high degree of covalent cross-linking within the CPD76% co-polymer is believed to result in a lower intensity for the second peak. Incorporation of $Co_2(CO)_8$ into CPD76% results in the disappearance of the peak at 22º, and the appearance of a broad peak centered at 15º. Co@C-CPD76% has three distinct sharp peaks in common with Co_xO_y@C-CPD76%. The peak at *ca*. 30º, was assigned the (002) plane of graphite, and the peaks at 52º and 61º match well with the *fcc* lattice of metallic cobalt with a (111) and (200) crystal structure, respectively, indicating that complete oxidation to Co_3O_4 was not achieved.[26,29,44] The presence of the intense sharp graphitic peak in both Co@C-CPD76% and Co_xO_y@C-CPD76% confirm their possession of high graphitic content. Co_xO_y@C-CPD76% shows several groups of peaks of varying intensity centered at *ca*. 22º, 36º, 42º, 70º, and 77º correspond to the (111), (220), (311), (511), and (440) crystal planes of Co_3O_4 respectively.[20,21,24,29,33] Additional peaks at *ca*. 50º and 73º can be assigned to the (200) and (220) planes of CoO, respectively. To remove all traces of cobalt that may overlap with higher 2θ peaks of graphene, a sample of Co_xO_y@C-CPD76% was washed with 3 M HCl five times and rinsed with deionized water, until a pH of ~7 was reached. In the resulting XRD pattern, all peaks associated with cobalt species disappear while the large peak centered at 30º remain unchanged, indicating that the carbonization process produced a large quantities of graphitic layers with narrow interplanar spacing distributions. Pristine carbons C-

CPD76% and XC-CPD76% are nearly identical to each other, showing broad peaks at about 4.5º that are caused by a high-density group of slit micropores within the carbon materials. This peak is also apparent in the pure and cobalt containing polymers CPD76% and CPD76%/$Co_2(CO)_6$. Additionally, the broad peaks near 25º and 50º can be attributed to the (002) and (100) planes of graphitic structures respectively.[45-47] The broad nature of these peaks in C-CPD76% and XC-CPD76% indicates that the carbons are only partially graphitized, containing a low concentration of parallel layers. This is a commonly found in amorphous carbon materials carbonized at relatively low temperatures (800 ºC).

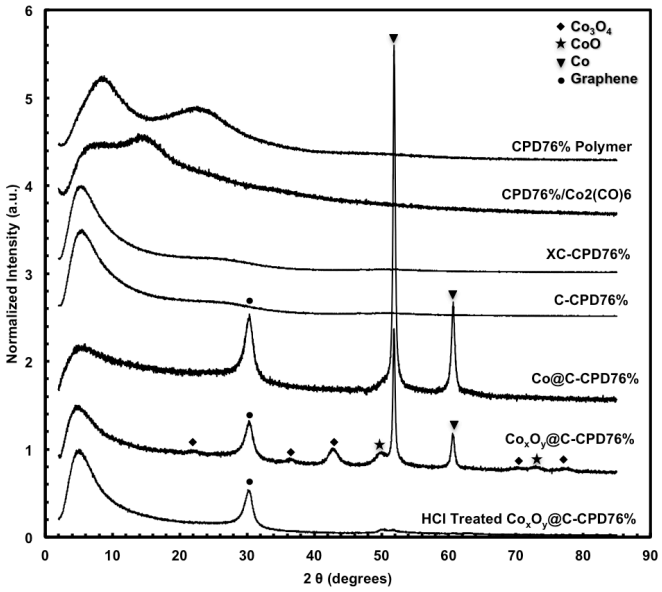

Figure 3.3 XRD patterns for CPD76% polymer, CPD76%/Co2(CO)6 moiety, Co_xO_y@C-CPD76% carbon, HCl treated Co_xO_y@CPD76% carbon, XC-CPD76% carbon, C-CPD76% carbon, and Co@C-CPD76%.

Approximate crystallite size and interplanar spacing of the different cobalt species and graphitic regions were calculated from the XRD peaks using Equation (3.3) and (3.4) respectively,[48,49]

$$\tau = \frac{K\lambda}{\beta cos\theta} \quad (3.3)$$

$$n\lambda = 2dsin\theta \quad (3.4)$$

where τ is the mean crystallite size in nanometers, K is a shape factor (assume K = 0.9), λ is the X-ray incident beam wavelength ($\lambda = 1.79$ Å), β is the width of the peak at half of the peak's maximum intensity in radians, θ is the diffraction angle in radians, d is the interplanar d-spacing, and n is a integer (assume n = 1). Calculations show typical interplanar d-spacings for graphene ($d_{(002)}$ = 3.4 Å), as well Co ($d_{(111)}$ = 2 Å; $d_{(200)}$ = 1.8 Å), Co_3O_4 ($d_{(111)}$ = 4.7 Å; $d_{(220)}$ = 2.9 Å; $d_{(311)}$ = 2.5 Å; $d_{(511)}$ = 1.6 Å; $d_{(440)}$ = 1.4 Å) and CoO ($d_{(200)}$ = 2.1 Å; $d_{(220)}$ = 1.5 Å), and the large peak centered at *ca*. 4.5° has a very large calculated interplanar d-spacing between 8 – 50 Å. The crystallite sizes of Co ($\tau_{(111)}$ = 263 Å; $\tau_{(200)}$ = 183 Å), Co_3O_4 ($\tau_{(111)}$ = 47 Å; $\tau_{(220)}$ = 60 Å; $\tau_{(311)}$ = 59 Å; $\tau_{(511)}$ = 41 Å; $\tau_{(440)}$ = 47 Å), and CoO ($\tau_{(200)}$ = 53 Å; $\tau_{(220)}$ = 55 Å) within Co_xO_y@C-CPD76%, calculated from the XRD peaks using Equation (3.3), suggest some agglomeration of the cobalt species during the synthesis of Co_xO_y@C-CPD76%. These values are consistent with TEM images of Co@C-CPD76% and Co_xO_y@C-CPD76% shown in Figure 3.4.

TEM and high resolution TEM images of CPD76%/$Co_2(CO)_6$ in Figure 3.4(b), show few signs of the cobalt carbonyl groups within its amorphous structure. Carbonization of the CPD76%/$Co_2(CO)_6$ into Co@C-CPD76% results in a drastic change in morphology. As seen in Figure 3.4(c), Co@CPD76% shows highly crystalline regions (indicated by arrows) with interplanar spacings of *ca*. 2 Å, 3.5 Å, and 4.7 – 14.7 Å,

estimated from the images, which correlates well with the XRD peaks of cobalt metal, graphitic layers and the slit micropores within the carbon, respectively. In the high resolution image of Co_xO_y@CPD76% (Figure 3.4(d)), arrows indicate crystalline regions with estimated interplanar distances of 4.5 Å (Co_3O_4), 3.3 Å (graphene) and 2.5 Å (CoO), which are in good agreement with the XRD results.

Energy dispersive x-ray spectrometry (EDS) was used consecutively with the TEM analysis to determine the distribution of cobalt, carbon and oxygen groups at various stages in the synthesis procedure. Distribution images can be seen in Figure 3.5. CPD76%/$Co_2(CO)_6$ polymer precursor shows a relatively diffuse cobalt distribution (Figure 3.5(a)) in comparison with the Co@CPD76% and Co_xO_y@CPD76%. The increased intensity of the cobalt signature in the Figures 3.5 (b) and (c), can be attributed to weight loss during the carbonization process, which increased the proportion of cobalt in Co@CPD76% and Co_xO_y@CPD76% relative to CPD76%/$Co_2(CO)_6$. The oxygen content in Co@CPD76% is also much higher compared to the carbonized materials due to the high carbonyl content. After carbonization, Co@CPD76% shows drastically reduced oxygen content as a result of the volatilized carbonyl groups, and higher cobalt to carbon ratio (Figure 3.5(b)). Oxidation of the Co@CPD76% to Co_xO_y@CPD76%, as expected, increases the oxygen content due to formation of cobalt oxides within the carbon support, as well as the oxidation of the carbon support itself. This EDS characterization confirms the uniform distribution of cobalt species within CPD76%, Co@C-CPD76%, and Co_xO_y@C-CPD76%. Such uniform dispersion benefits from the molecular level complexation of $Co_2(CO)_8$ with the pendent alkyne groups in CPD76%.

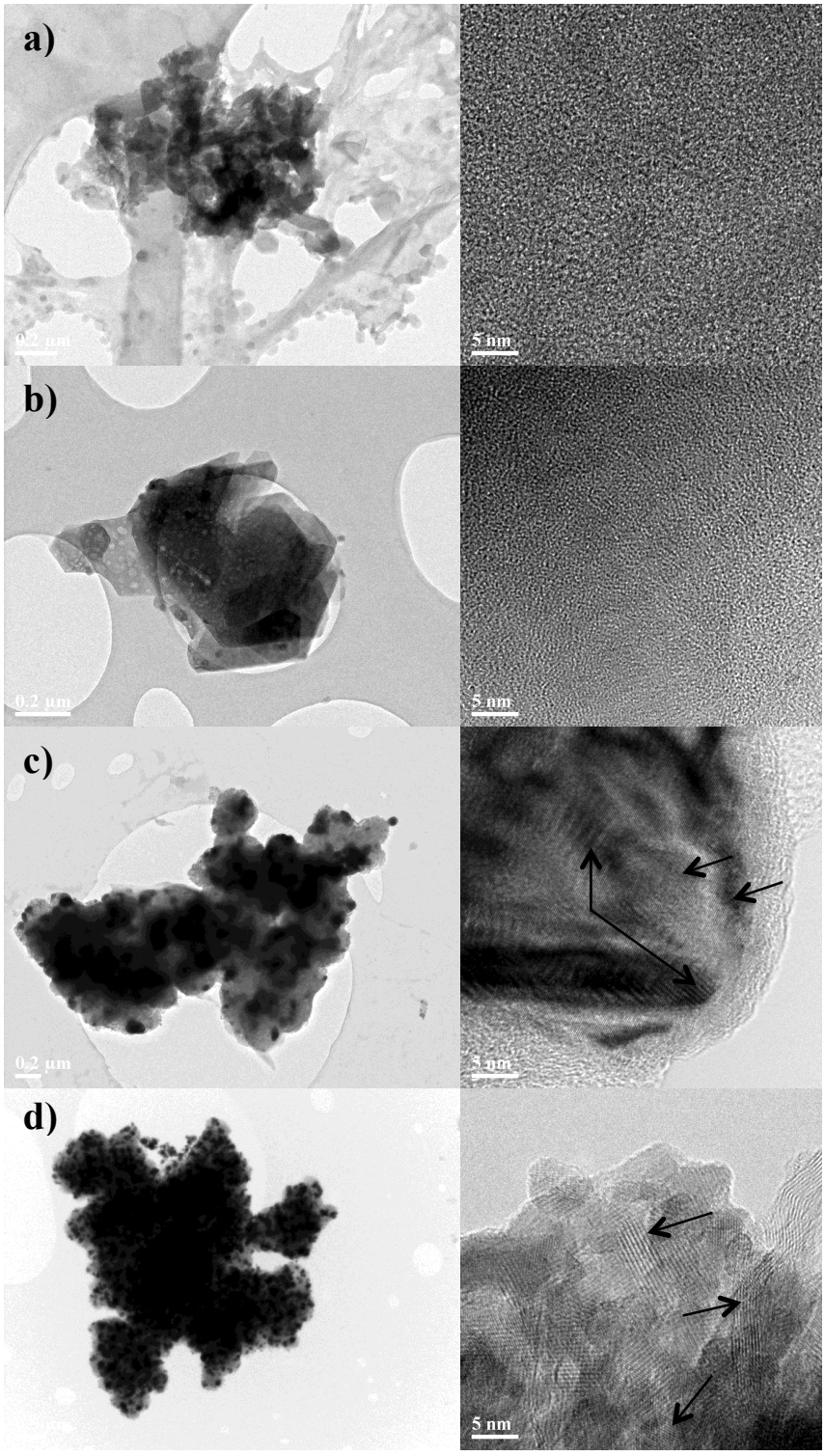

Figure 3.4 TEM (left image) and High resolution TEM (right image) of (a) CPD76%, (b) CPD76%/$Co_2(CO)_6$ polymer, (c) Co@C-CPD76%, and (d) Co_xO_y@C-CPD76.

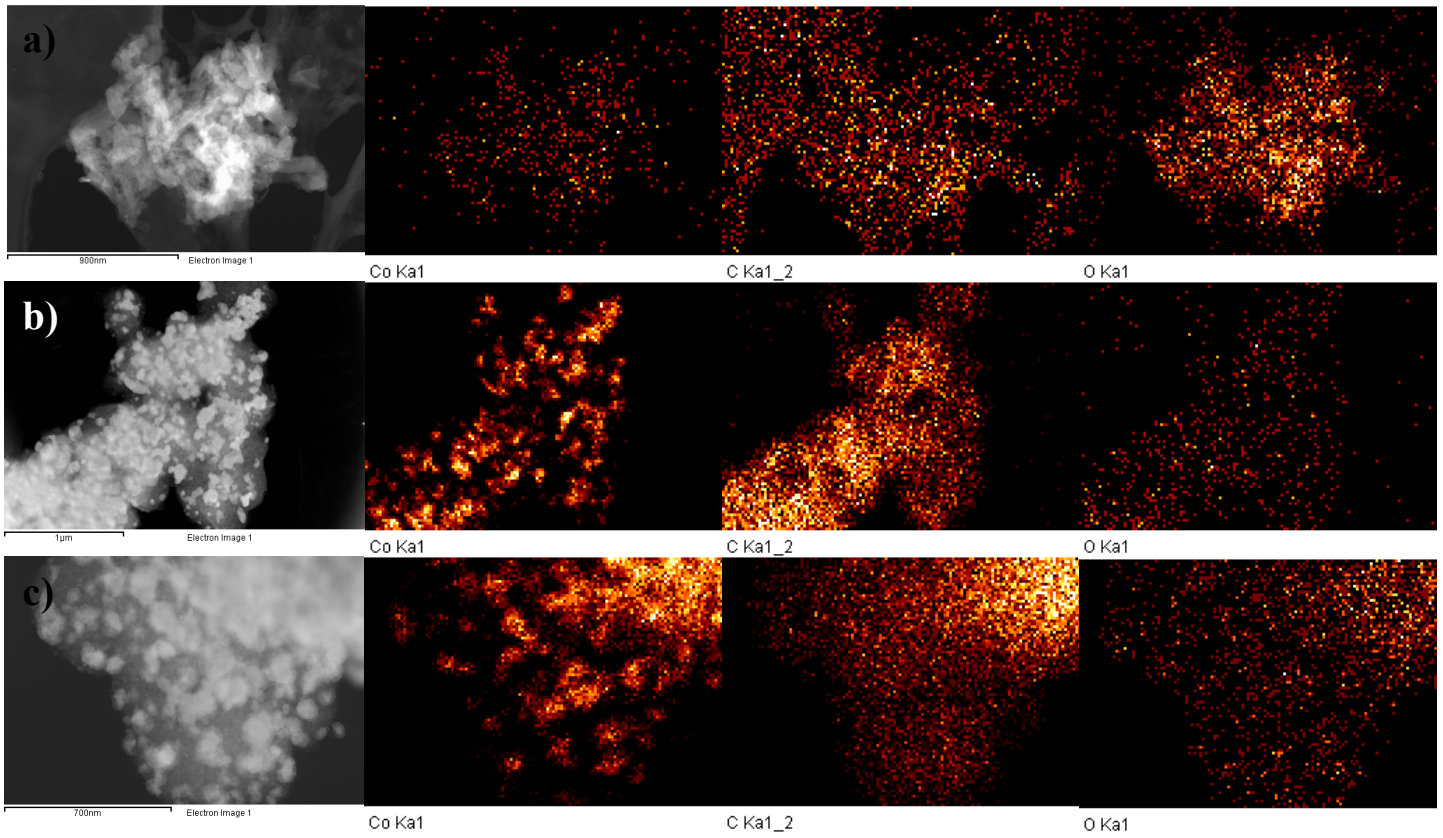

Figure 3.5 TEM-EDS images showing cobalt, carbon, and oxygen content of (a) CPD76%/$Co_2(CO)_6$, (b) Co@C-CPD76%, (c) Co_xO_y@C-CPD76%.

Table 3.1 N_2 sorption characterization results

Carbon Sample	Surface Area [a] (m^2/g)		Pore Volume [b] (cm^3/g)		Average Pore [c] Size (Å)	
	S_{BET}	$S_{d<20\ Å}$	V_{total}	$V_{d<20Å}$ (%)	d_{micro}	d_{meso}
C-CPD76%	468	415 (89%)	0.26	0.22 (82%)	4.88	38.33
XC-CPD76%	435	385 (88%)	0.25	0.20 (82%)	4.77	39.48
Co_xO_y@C-CPD76%	230	117 (51%)	0.21	0.06 (30%)	5.08	44.25

[a] Surface area of micropores ($S_{d<20\ Å}$) determined with t-plot method. [b] Total pore volume (V_{total}), micropore volume ($V_{d<20\ Å}$) determined with t-plot method. The percentage data in parentheses denote the percentage of pore volume of micropores to the total pore volume. [c] Average mesopore size (d_{meso}) determined from BJH desorption model and median micropore size (d_{micro}) determined with HK model.

Table 3.1 lists surface areas, pore volumes and pore sizes obtained from analysis of N_2 sorption results. The carbonized pristine CPD76%, and oxidized pristine carbon XC-CPD76% show relatively similar surface areas (468 $m^2\ g^{-1}$ and 435 $m^2\ g^{-1}$, respectively) and pore volumes (0.26 $cm^3\ g^{-1}$ and 0.25 $cm^3\ g^{-1}$), while Co_xO_y@C-CPD76% has a much lower surface area (230 $m^2\ g^{-1}$) and pore volume (0.21 $cm^3\ g^{-1}$). The micropore surface area and pore volume ratios for Co_xO_y@C-CPD76% were found to be significantly lower than those of C-CPD76% and XC-CPD76%, as seen in Table 3.1. BET isotherms in Figure 3.6(a) show that C-CPD76% and XC-CPD76% both exhibit type I isotherms and small type H4 hysteresis loops, as described by IUPAC.[50] Type I isotherms are the result of highly microporous materials with low external surface areas. The small H4 hysteresis loops suggest that there is a very little or no mesoporosity. These descriptions are well in agreement with TEM imaging in Figure 3.4, values in Table 3.1, BJH mesopores size distributions in Figure 3.6(b), and the HK micropore pore size distributions in Figure 3.6(c).[50] Co_xO_y@C-CPD76% can be described as a type IV isotherm with a large type H2 hysteresis loop. Type IV isotherms are characterized by there large hysteresis loop, which are typical of mesoporous materials. The large H2

hysteresis loop is difficult to interpret but is often associated with the difference in the condensation and evaporation mechanisms within highly interconnected mesopores.[50] Figure 3.6(b) shows a large fraction of pore volume can be attributed to pores with a diameter between about 35 Å to 45 Å. The HK pore size distribution, Figure 3.6(c), shows a much smaller micropore volume for Co_xO_y@C-CPD76% relative to C-CPD76% and XC-CPD76%. Since the initial heating to 100 °C released CO from the $Co_2(CO)_6$/alkyne moiety prior to any carbonization process, it is believed that the cobalt metal may have caused catalytic reactions with the micropores in the carbon at high temperatures, resulting in the collapse of these pores. The result is a broadening of pore size distribution for Co_xO_y@C-CPD76% with a slightly higher average mesopore size and lower micropore size, as seen in Table 3.1.

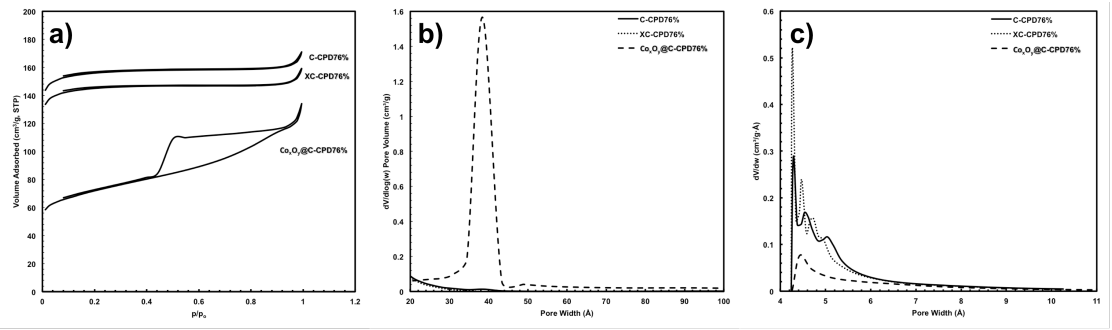

Figure 3.6 N_2 Sorption results: (a) BET isotherms, (b) BJH mesopore size distributions, and (c) HK micropore size distributions for C-CPD76%, XC-CPD76%, and Co_xO_y@C-CPD76%.

3.3.2 Electrocapacitive Performance of Pristine and Cobalt Containing Carbons

The performance of selected carbonaceous materials were tested for their electrochemical performance using a 3-electrode set up in 2 M KOH aqueous solution. Cyclic voltammetry of the electrode fabricated with Co_xO_y@C-CPD76% indicates that it

undergoes multiple phase changes with different changes in cobalt oxidation state, as represented by multiple peaks at different potentials in Figure 3.7. Several reversible redox reactions, shown below in Equations (3.4) to (3.7), have been attributed to the anodic and cathodic peaks from cobalt redox reactions in alkaline aqueous solutions.[21,23,24,28,29,51]

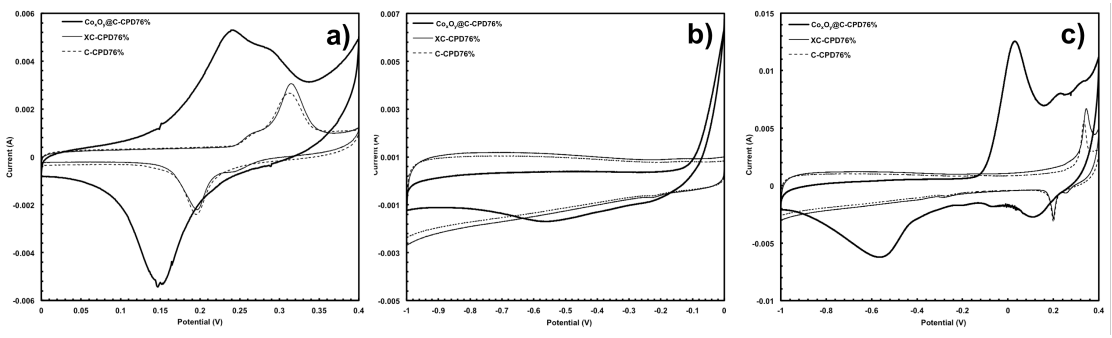

Figure 3.7 Cyclic Voltammetry curves for C-CPD76%, XC-CPD65% and Co_xO_y-C-CPD76% between (a)0 – 0.4 V (b) -1 – 0 V (c) -1 – 0.4 V vs SCE.

$$3Co(OH)_2 + 2OH^- \rightarrow Co_3O_4 + 4H_2O + 2e^- \quad (3.4)$$

$$Co(OH)_2 + OH^- \rightarrow CoOOH + H_2O + e^- \quad (3.5)$$

$$Co_3O_4 + OH^- + H_2O \rightarrow 3CoOOH + e^- \quad (3.6)$$

$$Co + 2OH^- \rightarrow Co(OH)_2 + 2e^- \quad (3.7)$$

In Figure 3.7(a) and (c), the anodic peaks for Co_xO_y@C-CPD76% centered at *ca*. 0.24 V and 0.28 V with corresponding cathodic peaks at *ca*. 0.15 V and -0.05 V, respectively, are attributed to the oxidation of $Co(OH)_2$ into Co_3O_4 and CoOOH according to Equations (3.4) to (3.6). Anodic and cathodic peaks centered at *ca*. 0.33 V and 0.21 V,

respectively, for C-CPD76% and XC-CPD76% are a result of similar faradaic reactions of nickel foam in the KOH electrolyte.[21,25] The cathodic and anodic peaks at *ca*. -0.55 V and 0 V, for Co_xO_y@C-CPD76%, as seen in Figure 3.7 (b) and (c), are attributed to reduction/oxidation of cobalt metal/$Co(OH)_2$ according to Equation 3.7.[51] The lack of similar peaks in the voltammograms for C-CPD76% and XC-CPD76 suggests that the nickel oxide, NiO, layer on the surface of the nickel foam is highly stable and does not undergo reduction to nickel metal to any appreciable extent.[25] Further to this, because the nickel oxide layer appears stable in the potential range between -1 and 0 V (see Figure 3.7(b)), it may be concluded that this potential range corresponds to ECDL behavior for the pristine carbons. In addition, it can be seen that in this potential range both C-CPD76% and XC-CPD76% exhibit higher capacitances than Co_xO_y@C-CPD76%. This is likely a result of their differences in morphology between the Co_xO_y@C-CPD76% and the other two carbons. Regardless, these results indicate that EDLC capacitance from the carbon dominates in the -1 to 0 V range, while PS behavior dominates in the 0 to 0.4 V range tested. Unfortunately, the contribution from Ni foam, although small, results in slightly overestimated specific capacitances when utilizing potentials above *ca*. 0.13 V. Therefore, the pseudocapacitive contribution of bare Ni foam redox reactions (*ca*. 0.13 to 0.4 V) was subtracted from the total area used in Equation 2.1 to better represent the electrode specific capacitances in the 0 to 0.4 V and -1 to 0.4 V ranges. The specific capacitances for the various carbons estimated from the voltammograms in Figure 3.7 using Equation 2.1 and are summarized in Table 3.2.

Table 3.2 Cyclic Voltammetry Results for C-CPD76%, XC-CPD76%, and Co_xO_y@C-CPD76%.

Sample	Cyclic Voltammetry Specific Capacitance (F/g)								
	0 – 0.4V Range			-1 – 0 V Range			-1 – 0.4 V Range		
	100 mV/s	10 mV/s	1 mV/s	100 mV/s	10 mV/s	1 mV/s	100 mV/s	10 mV/s	1 mV/s
C-CPD76%	13(14)	33(35)	55(58)	72	99	101	44(46)	86(87)	105(108)
XC-CPD76%	11(12)	27(29)	50(53)	67	105	113	33(34)	86(87)	123(126)
Co_xO_y@C-CPD76%	30(31)	131(132)	182(184)	36	50	71	52(53)	136(137)	277(280)

***Values in parentheses show specific capacitances before removing the Ni foam contribution**

GCD was used to investigate the pseudocapacitive behavior in the same potential ranges of the CV study. The discharge curves, see Figure 3.8 (a) to (c), are often considered to provide more accurate estimations of specific capacitance.[40] As such, the discharge curves were also used to determine energy densities, see Figure 3.8 (d) – (f). The calculated specific capacitances, using Equation 2.2, and energy densities, using Equation 3.3, were used to estimate power densities, using Equation 3.4. Discharge times of bare Ni foam current collectors (in the range of 0.13 to 0.4 V) were subtracted from the total discharge times of the carbon electrodes in order to compensate for Ni foam's pseudocapacitive contribution. Specific capacitances, maximum energy densities, and power densities obtained through GCD measurement, are listed in Table 3.3 and Table 3.4, respectively.

Figure 3.8(g) – (i) shows varying capacitance retentions for each potential window. Specific capacitances decrease fairly linearly with increasing current density within the potential window of 0 to 0.4 V, and decrease exponentially in the potential window of -1 to 0 V at low current densities. Widening the potential window to -1 to 0.4 V results in a combined effect of the aforementioned capacitance retention behaviors.

Co_xO_y@C-CPD76% retains about 41% of its capacitance between 10 A g^{-1} and 0.1 A g^{-1} in the 0 to 0.4 V range, 7% in the -1 to 0 V range, and 28% in the expanded 1.4 V range.

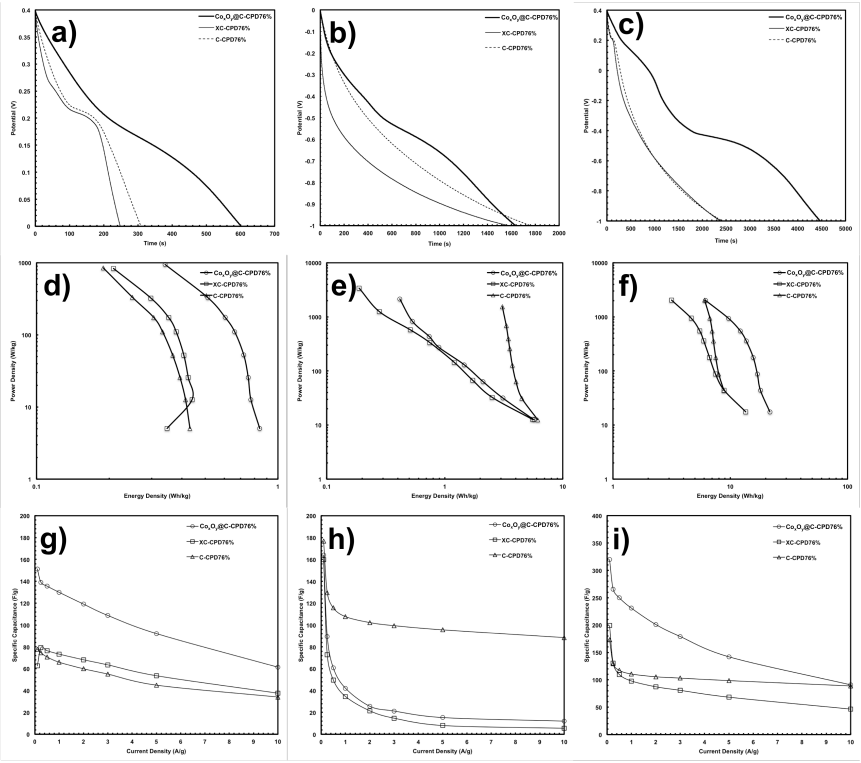

Figure 3.8 GCD curves in potential windows (a) 0 – 0.4 V; (b) -1 – 0 V; (c) -1 – 0.4 V, Ragone plots in potential windows (d) 0 – 0.4 V; (e) -1 – 0 V; (f) -1 – 0.4 V, and capacitance retention curves in potential windows (g) 0 – 0.4 V; (h) -1 – 0 V; (i) -1 – 0.4 V.

Table 3.3 Chronopotentiometry Charge Discharge Results for C-CPD76%, XC-CPD76%, and Co_xO_y@C-CPD76%.

Sample	Chronopotentiometry Charge Discharge Specific Capacitance (F/g)								
	0 – 0.4V Range *			-1 – 0 V Range			-1 – 0.4 V Range *		
	3 A/g	1 A/g	0.1 A/g	3 A/g	1 A/g	0.1 A/g	3 A/g	1 A/g	0.1 A/g
C-CPD76%	39(55)	54(66)	43(78)	99	108	177	99(103)	107(111)	164(173)
XC-CPD76%	48(64)	62(73)	28(63)	15	35	160	77(81)	95(98)	189(199)
Co_xO_y@C-CPD76%	93(109)	118(130)	117(151)	21	42	164	175(179)	228(231)	310(320)

***Values in parentheses show specific capacitances before removing the Ni foam contribution.**

Table 3.4 Maximum Energy Density and Power Density Obtained through GCD.

Sample	Potential Range					
	0 - 0.4 V		-1 – 0 V		-1 - 0.4 V	
	E* Wh/kg	P W/kg	E Wh/kg	P W/kg	E* Wh/kg	P W/kg
C-CPD76%	0.24(0.43)	851	6	1537	11(12)	2034
XC-CPD76%	0.15(0.35)	833	6	3394	13(14)	2034
Co_xO_y@C-CPD76%	0.65(0.84)	944	6	2139	21(22)	2017

***Values in parentheses show energy density before removing the Ni foam contribution.**

EIS measurements were performed on the carbons in the frequency range of 0.01 Hz to 10 kHz at 0 V (vs SCE), to evaluate some important electrochemical characteristics of the carbon. All samples show, to a degree, three characteristic features of supercapacitors; a small semicircle at high frequencies, an inclined line (*ca.* 45º slope) at intermediate frequencies, and a near vertical line at low frequencies.[24,28] The intercept of the semicircle at high frequencies with the x-axis of the Nyquist plot in Figure 3.9 is used to determine the equivalent series resistance (ESR) of the prepared electrode cell. ESR represents the combination of the ionic resistance of the electrolyte, the internal resistances of the current collector and active-material, and the current collector/active-material/electrolyte interface resistances in series. ESR values for XC-CPD76% (0.762 Ω) and Co_xO_y@C-CPD76% (0.743 Ω) are very similar, but C-CPD76% (0.607 Ω) displays the lowest of the 3 samples. These values are in good agreement with the small ohmic drops found in the GCD curve of Figure 3.8(a) – (c). It is particularly impressive that the Co_xO_y@C-CPD76% displayed such low ESR values, likely a result of the highly graphitic content in contact with the Co_3O_4 particles.[24] The diameters of the semicircles obtained from the Nyquist plots represent the faradaic charge transfer resistance (R_{CT}),

and are only just apparent for the pristine carbons as a result of an overlap with the Warburg diffusion resistance region. This has been attributed to an interfacial impedance effect that is ideal for capacitors.[28] The 45° sloped Warburg region arises due to the diffusion limiting transport of ions through micropores in the bulk of the material, while the semicircle R_{CT} region is a result the faradaic charge transfer resistances of the active materials caused by ion transport within the mesopores.[28] Typically PS materials have comparably higher R_{CT} values than EDLCs as a result of their faradaic reactions, however, all three carbons tested experience almost identical R_{CT} values 0.541 Ω, 0.591 Ω, and 0.579 Ω for C-CPD76%, XC-CPD76%, and Co_xO_y@C-CPD76%, respectively. We attribute this exceptionally lower R_{CT} value for Co_xO_y@C-CPD76% to its high graphitic content in contact with Co_xO_y, thus improving the kinetic limitations of ion and electron transport pathways.[28] C-CPD76% and XC-CPD76% both display relatively long Warburg resistance regions, indicating slow movement of ions within the micropores, while Co_xO_y@C-PCD76% has very low Warburg impedance because of it's highly mesoporous structure, in good agreement with the N_2 adsorption results in Table 3.1.

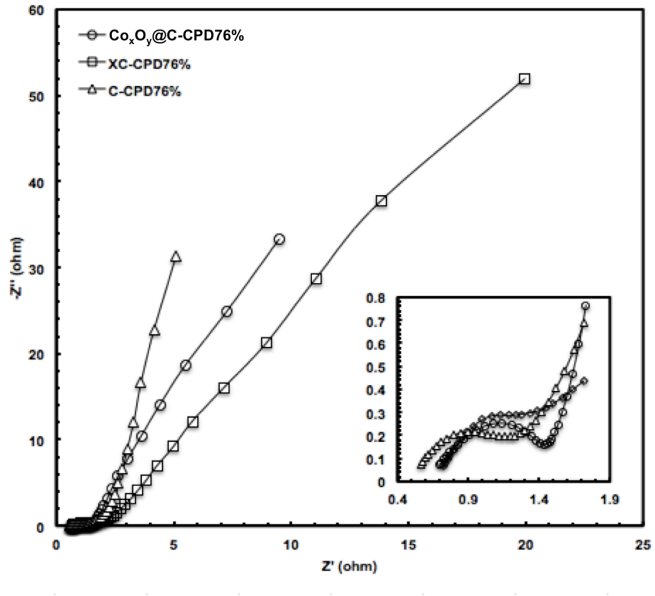

Figure 3.9 EIS Nyquist plots for C-CPD76%, XC-CPD76%, and Co_xO_y@C-CPD76%. The insert shows a closer view of the semicircles produced at high frequencies.

3.4 Conclusion

This chapter demonstrates the effective use of CPD76% as a polymer precursor for evenly distributing cobalt nanoparticles in a graphitic carbon support, and its application as an EDLC/PS hybrid supercapacitor. Co_xO_y@C-CPD76% was synthesized through carbonization and oxidation of an alkyne/$Co_2(CO)_6$ moiety, obtained by complexing $Co_2(CO)_8$ with the pendent alkyne groups in CPD76%, which has been rarely explored for supercapacitor applications. The CPD76%/$Co_2(CO)_6$ moiety was able to effectively and evenly distribute cobalt nanoparticles throughout the polymer and resulting carbon. High temperature reactions between cobalt and carbon during the initial carbonization step produced a highly conductive graphitic carbon support for the Co_xO_y, as well as a primarily mesoporous structure. CV, GCD, and EIS measurements were

performed on the Co_xO_y@C-CPD76% in three voltage windows to investigate their EDLC and PS properties. Electrochemical GCD measurements showed a maximum specific capacitance (310 F/g) at 0.1 A g^{-1}, a high energy density (21 W h kg^{-1}), and high power density (2017 W kg^{-1}) in a potential window of -1 to 0.4 V. Extremely low ESR (0.743 Ω) and R_{CT} (0.579 Ω) values were recorded, which is attributed to the conductive graphitized carbon and highly mesoporous structure in contact with the pseudocapacitive Co_xO_y nanoparticles.

3.5 References

(1) F. Béguin, V. Presser, A. Balducci, and E. Frackowiak, *Adv. Mater.*, **2014**, *26*, 2219-2251.

(2) S. Rondeau-Gagne´ and J-F Morin , *Chem. Soc. Rev.* , **2014**, *43*, 85-98.

(3) D. R. Rolison, J. W. Long, J. C. Lytle, A. E. Fischer, C. P. Rhodes, T. M. McEvoy, M. E. Bourg, Megan E. Bourg, and A. M. Lubers, *Chem. Soc. Rev.*, **2009**, *38*, 226-252.

(4) L. Borchardt , M. Oschatz , and S. Kaskel, *Mater. Horiz.*, **2014**, *1*, 157-168.

(5) M. Inagaki , H. Konno, and O. Tanaike, *J. Power Sources*, **2010**, *195*, 7880–7903.

(6) L. L. Zhang and X. S. Zhao , *Chem. Soc. Rev.*, **2009,** *38*, 2520–2531.

(7) L. L. Zhang, Y. Gu, and X. S. Zhao, *J. Mater. Chem. A*, **2013,** *1*, 9395–9408.

(8) Y. Zhai, Y. Dou, D. Zhao, P. F. Fulvio, R. T. Mayes, and S. Dai, *Adv. Mater.*, **2011,** *23*, 4828–4850.

(9) G. Wang, L. Zhang, and J. Zhang, *Chem. Soc. Rev.*, **2012**, *41*, 797-828.

(10) P. Simon and Y. Gogotsi, *Acc. Chem. Res.*, **2013,** *46*, 1094–1103.

(11) S. Yang, R. E. Bachman, X. Feng, and K. Müllen, *Acc. Chem. Res.,* **2013,** *46*, 116-

128.

(12) B. E. Conway, V. Birss, and J. Wojtowicz, *J. Power Sources*, **1997,** *66*, 1-14.

(13) M. B. Sassin, C. N. Chervin, D. R. Rolison, and J. W. Long, *Acc. Chem. Res.*, **2011,** *46*, 1062-1074.

(14) J. Jiang, Y. Li, J. Liu, X Huan, C. Yuan, and X. W. Lou, *Adv. Mater.*, **2012,** *24*, 5166-5180.

(15) V. Augustyn, P. Simon, and B. Dunn , *Energy Environ. Sci.*, **2014,** *7*, 1597-1614.

(16) C. D. Lokhande , D. P. Dubal, and O.-S. Joo, *Curr. Appl. Phys.*, **2011,** *11*, 255-270.

(17) Zhong-Shuai Wu, G. Zhou, L.-C. Yin, W. Ren, F, Li, and H.-M. Cheng, *Nano Energy*, **2012,** *1*, 107-131.

(18) C. Liu, F. Li, L.-P. Ma, and H.-M. Cheng, *Adv. Mater.*, **2010,** *22*, E28–E62.

(19) B. G. Choi, M.H. Yang, S. C. Jung, K. G. Lee, J.-G. Kim, H. S. Park, T. J. Park, S. B. Lee, Y.-K. Han, and Y.S. Huh, *ACS Nano*, **2013,** *3*, 2453-2460.

(20) C. Zhou, Y. Zhang, Y. Li, and J. Liu, *Nano Lett.*, **2013,** *13*, 2078−2085.

(21) J. H. Kwak, Y.-W. Lee, and J. H. Bang, *Mater. Lett.*, **2013,** *110*, 237-240.

(22) G. Godillot, L. Guerlou-Demourgues , L. Croguennec , K. M. Shaju , and C. Delmas , *J. Phys. Chem. C*, **2013,** *117*, p. 9065−9075.

(23) X. Ge, C. D. Gu, X. L. Wang, and J. P. Tu, *J. Phys. Chem. C*, **2014,** *118*, 911−923.

(24) R. B. Rakhi, W. Chen, D. Cha, and N. H. Alshareef, *Nano Lett.*, **2012,** *12*, 2559-2567.

(25) L. Gu, Y. Wang, R Lu, L. Guan, X. Peng, and J. Sha, *J. Mater. Chem. A*, **2014,** *2*, 7161-7164.

(26) X.-C. Dong, H. Xu, X.-W. Wang, Y.-X. Huang, M. B. Chan-Park, H. Zhang, L.-L. Wang, W. Huang, and P. Chen, *ACS Nano*, **2012,** *6*, 3206-3213.

(27) Y. He, W. Chen, X. Li, Z. Zhang, J. Fu, C. Zhao, and E. Xie, *ACS Nano*, **2013,** *7*, 174–182.

(28) S. K. Meher and G. R. Rao, *J. Phys. Chem. C*, **2011,** *115*, 15646–15654.

(29) Q. Guan, J. Cheng, B. Wang, W. Ni, G. Gu, X. Li, L. Huang, G. Yang, and F. Nie, *Appl. Mater. Interfaces*, **2014,** *6*, 7626−7632.

(30) W. Zhou, J. Liu, T. Chen, K. S. Tan, X. Jia, Z. Luo, C. Cong, H. Yang, C. M. Li, and T. Yu, *Phys. Chem. Chem. Phys.*, **2011,** *13*, 14462–14465.

(31) L. Wang, C. Lin, F. Zhang, and J. Jin, *ACS Nano*, **2014,** *8*, 3724-3734.

(32) Z.-A. Hu, Y.-L. Xie, Y.-X. Wang, L.-J. Xie, G.-R. Fu, X.-Q. Jin, Z.-Y. Zhang, Y.-Y. Yang, and H.-Y. Wu, *J. Phys. Chem. C*, **2009,** 113, 12502–12508.

(33) H. S. Lee, J. Choi, J. Jin, J. Chun, S. M. Lee, H. J. Kim, S. U. Son, *Chem. Commun.*, **2012,** *48*, 94-96.

(34) Y. Liang, M. G. Schwab, L. Zhi, E. Mungnaioli, I. Kolb, X. Feng, and K. Müllen, J. Am. Chem. Soc., **2010,** *132*, 15030–15037.

(35) L. Zhi, Y.-S. Hu, B. El Hamaoui, X. Wang, I. Lieberwirth, U. Kolb, J. Maier, and K. Müllen. *Adv. Mater.*, **2008,** *20*, 1727–1731.

(36) P. I. Dosa, C. Erben, V. S. Iyer, K. Peter C. Vollhardt, and I. M. Wasser, *J. Am. Chem. Soc.*, **1999,** *121*, 10430-10431.

(37) M. R. Tirpak, J. H. Wotiz, and C. A. Hollingsworth, *J. Am. Chem. Soc.*, **1958,** *80*, 4265–4269.

(38) B. El Hamaoui, L. Zhi, J. Wu, J. Li, N. T. Lucas, Ž. Tomović, U. Kolb, K. Müllen, *Adv. Funct. Mater.*, **2007,** *17*, 1179-1187.

(39) L. A. Mîinea, L. B. Sessions, K. D. Ericson, D. S. Glueck, and R. B. Grubbs, *Macromolecules*, **2004,** *37*, 8967-8972.

(40) M. D. Stoller and R. S. Ruoff, *Energy Environ. Sci.*, **2010,** *3*, 1294-1301.

(41) Z. Dong and Z. Ye, *Macromolecules*, **2012,** *45*, 5020−5031.

(42) H. Greenfield, H. W. Sternberg, J. H. Wotiz, R. Markby, and Irving Wender, *J. Am. Chem. Soc.*, **1956,** *78*, 120–124.

(43) B. Z. Tang and Hongyao Xu, *Macromolecules*, **1999,** *32*, 2569-2576.

(44) T. M. Keller, S. B. Qadri , and C. A. Little, *J. Mater. Chem.*, **2004,** *14*, 3063–3070.

(45) D. Puthusseri, V. Aravindan, S. Madhavi, and S. Ogale, *Energy Environ. Sci.*, **2014,** *7*, 728-735.

(46) J. Hu, H. Wang, Q. Gao, and H. Guo, *Carbon*, **2010,** *48*, 3599–3606.

(47) A. J. Amali, J.-K. Sun, and Q. Xu, *Chem. Commun.*, **2014**, 50, 1519-1522.

(48) A. L. Patterson, *Phys. Rev.*, **1939,** *56*, 987-982.

(49) G. E. M. Jauncey, *Proc. Natl. Acad. Sci.*, **1924,** *10*, 57–60.

(50) K. S. W. Sing, D. H. Everett, R. A. W. Haul, L. Moscou, R. A. Pierotti, J. Rouquérol, T. Siemieniewska, *Pure & Appl. Chem.*, **1985,** *57*, 603-619.

(51) T. R. Jayaraman, V. K. Venkatesan, and H. V. K. Udupa, *Electrochemica Acta.,* **1975**, *20*, *209-213.*

Chapter 4: Conclusions and Outlooks

This thesis presents the production and characterization of highly cross-linked copolymers of phenylacetylene and 1,3-diethynylbenzene as high-yield precursors for nanoporous carbons with applications in electrolytic double layer capacitors, pseudocapacitor carbon supports, hydrogen storage, and CO_2 capture. The polymers were first carbonized without the use of an activating agent, which produced microporous carbons with low surface areas and pore volumes (S_{BET} = ~500 $m^2\ g^{-1}$, V_{total}=0.31 $cm^3\ g^{-1}$). The copolymers also experienced different decomposition onset temperatures and carbon yields (up to 86%), which depend greatly on the cross-linker content. Upon carbonization in the presence of KOH, highly microporous activated carbons were produced with different textural properties directly related to cross-linker content (up to S_{BET}=1418 $m^2\ g^{-1}$, V_{total}=0.78 $cm^3\ g^{-1}$). Copolymers with cross-linker content from 39% to 84% displayed the best surface areas, pore volumes, and pore size distributions amongst the copolymers synthesized. Hydrogen and CO_2 sorption measurements indicated that the microporous activated carbons are well suited for hydrogen storage and CO_2 capture, displaying adsorption capacities rivaling the highest published adsorption values to date (2.66 wt% for H_2 adsorption at 77 K and 1 bar; up to 6.95 mmol g^{-1} for CO_2 along with a low relative N_2 adsorption at 0 ºC and 1 bar). In addition to gas sorption applications, the activated carbons demonstrated superior performance as electrode materials for electrochemical double layer capacitors. High specific capacitances (446 F g^{-1} at 0.5 A g^{-1} in 3 electrode cell), power densities, energy densities, and long cycle lives have been achieved using the activated carbons produced.

The copolymer CPD76% with a high pendent alkyne content, was subjected to a complexation reaction with $Co_2(CO)_8$, which dispersed cobalt species uniformly throughout the polymer matrix. ICP-MS, TEM, XRD, FTIR characterizations were employed throughout the synthesis process, from initial complexation reaction, to the carbonization and oxidation steps. Carbonization of the complexed precursor produced a highly graphitic carbon network with well-dispersed cobalt nanoparticles. The growth of graphitic layers was catalyzed by the presence of cobalt nanoparticles at high temperatures, providing a highly conductive support. Subsequent oxidation converted partially the surface of the cobalt nanoparticles into Co_3O_4. The improved electric properties resulted in extremely high power densities (2017 W kg^{-1}), energy densities (21 Wh kg^{-1}) and specific capacitances (310 at 0.1 A g^{-1} in 3 electrode cell) in a wide 1.4 V potential range. The hybridization of the EDLC and PS materials allows the electrodes to act as purely EDLC, or predominantly PS within the smaller individual potential regions (-1 to 0 V and 0 to 0.4 V).

This thesis provided an in-depth study into the use of DEB-PA copolymers in energy storage and gas sorption technologies, but has great potential for further research. Further exploration into the activation methods such as soft and hard templating could provide better ordered mesoporous carbons with microporous frameworks to improve power densities and capacitance retentions. The incorporation of cobalt nanoparticles into the carbon support also has potential for applications in catalytic oxygen reduction reactions, fuel cells, and lithium ion batteries. Graphitic networks could also be incorporated without the use of cobalt-catalyzed reactions by taking advantage of the

unique chemical and physical properties of graphene oxides, which could produce unique polymer composites.

In summary, the acetylenic copolymers of phenylacetylene and 1,3-diethynylbenze are a new and exciting material, which have use in a wide variety of applications in renewable energy research, EDLCs, pseudocapacitors, gas sorption materials, and other relevant nanotechnologies.